# UNIVERSITA' DEGLI STUDI DI PARMA

Dottorato di ricerca in Scienza e Tecnologia dei Materiali

Ciclo XXXII (2017-2020)


# Innovative Synthesis Methodology and Electronic Structure Investigation of "quasi-2D" Transition Metal Dichalcogenides: $MoS_2$ case


by

Amir GHIAMI

**Coordinatore:**

Prof. Enrico Dalcanale

**Supervisor:**

Dr. Roberto Verucchi

**Co-supervisor**:

Dr. Marco Vittorio Nardi

**Acknowledgement**

First and foremost, I would like to express my profound gratitude to my supervisor, Dr. Roberto Verucchi, for his supports, patient guidance and constant encouragement during the course of my PhD. My appreciation to him will surely continue over the years.

I am also grateful to my co-supervisor Dr. Marco Vittorio Nardi. I really appreciate him for devoting time and efforts to my research. His strict criticisms and comments on my scientific results, helped a lot to improve the quality of my research.

I would like to also thank Dr. Melanie Timpel for her assistance with functionalization of $MoS_2$ and helping me to improve my scientific writing and publishing. I would like to extend my appreciation to my other colleagues in IMEM-CNR institute, Dr. Lucrezia Aversa and Dr. Roberta Tatti for their valuable helps in performing XPS and UPS measurements and interpreting the data. I also would like to sincerely thank Dr. Petr Nozar for his assistance in using IJD tool and deposition process.

I also would like to thank Dr. Cedric Huyghebaert and Dr. Steven Brems to host me at 2D-Team at IMEC as a visiting researcher. That period helped me a lot to deepen my knowledge and experiences in the field of 2D materials and devices.

I would like to extend my heartfelt gratitude to all of my colleagues and friends at IMEM, IFN, FBK, University of Parma and University of Trento in Italy, and also my colleagues and friends at KU Leuven and IMEC in Belgium for their supports and encouragements, which helped me to overtake challenges and grow during the last three years.

I would like to take this opportunity to extend my warmest appreciation to two of my best friends and co-travelers, Dr. Shahab Aslani and Dr. Amir Ghorbani, who have accompanied me to this point, since I started my studies abroad in 2013. They made me experience a deep, cordial and unconditional friendship.

Finally, and most importantly, my deep and sincere gratitude to my parents, Fatemeh and Ali, for their continues support, patience and love. I am also grateful to my brother and sister-in-law, Ehsan and Ghazal for always being there for me as a friend. This journey would not have been possible without their supports, and I dedicate this milestone to them.

**Abstract**

Two-dimensional (2D) materials importance was born with graphene, about 16 years ago. The driving idea is that in case of a layered material such as graphite, when thinned down to isolated few or a single monolayer, it exhibits novel properties different from its bulk counterpart. In this sense, graphene was a breakthrough and its outstanding properties pushed research community towards the study of other layered materials, to find new 2D materials and possibly overcome some intrinsic issues of graphene for electronics, such as the semi-metallic behavior.

Transition metal dichalcogenides (TMDCs) are a class of recently emerged semiconductor materials, which has attracted enormous interests due to their intriguing physical, chemical and electrical properties. They show a typical layered structure, thus being promising 2D materials with semiconducting properties for electronics. The laboratory scale TMDC-based electronic devices like transistor, sensors, memristor etc. have been demonstrated, especially using few or single layer material and the outcome sparked hopes to obtain highly efficient electronic devices beyond Si-CMOS technology. However, the path through realization of electronic devices based on two dimensional TMDCs is suffering from many challenges which should be overcome. Controlling the surface electronic properties, role of defects and scalable synthesis of few/single layer TMDCs with large dimensions are some of the important issues still needed to be more investigated. In this thesis, we will explore these issues focusing our attention on Molybdenum Disulfide ($MoS_2$), probably the most studied TMDCs.

Initially, we studied the role of Sulfur defects on surface electronic properties of $MoS_2$. For this purpose, a 2H-$MoS_2$ single crystal was annealed at two different temperatures in ultra-high vacuum (UHV), in order to introduce Sulfur vacancies in a controlled manner. The detailed characterization of surface electronic properties of the sample by X-ray and ultraviolet photoelectron spectroscopy clearly evidences the formation of different key role players whose balance determines the final material's features. Followingly, passivating the Sulfur vacancies and recovery of the surface electronic properties have been investigated by thiol functionalization of pristine and thermally treated $MoS_2$ single crystal. Further assessment on the interaction between the molecule and underlying $MoS_2$ has been carried out by μ-Raman and FT-IR analysis. Although $MoS_2$ surface defects creation by thermal annealing and its surface functionalization has been already studied, we report here a

comprehensive analysis of surface electronic properties to deeply understand the complex mechanisms related to sulfur defects and their role in promoting reactivity towards an efficient functionalization by organic molecules.

Second part of this work was focused on synthesis of highly crystalline $MoS_2$ thin film by an up-scalable novel physical vacuum deposition (PVD) technique, so called Ionized Jet Deposition (IJD) that has been considered and demonstrated for the first time for this material. Initially, to understand the best working condition, IJD growth on Silicon substrate has been performed. Among the operating acceleration voltages, 15 kV was found to be the best compromise in terms of efficient ablation process and absence of target overheating. Deposited film shows chemical properties typical of $MoS_2$, with amorphous matrix and an excess of free, unbounded sulfur that can be removed by annealing in the 300-400°C temperature range. This led to a certain degree of structural order with misoriented lattices and unusual electronic properties. However, the formation of an interface comprised of several silicon oxide species was also observed between $MoS_2$ and silicon substrate, which probably originates from the oxidizing process from water molecules in the vacuum chamber during growth.

To overtake the complex interface formation, growth on platinum substrate was investigated, which is less susceptible to oxidation. It was found that annealing at 250 $^oC$ for 3 h, is the optimal annealing condition, which is also compatible with polymeric substrate. The study of electronic and structural properties of the IJD $MoS_2$ films was fulfilled by a multi-technical approach. Final results lead to a complex material that, in spite of its bulk nature (thickness of about 200 nm), shows features typical of few/mono layered nanocrystalline material. In the end, to demonstrate the applicability of the IJD-$MoS_2$ for electronic devices, a resistive random memory (ReRAM) device based on IJD-$MoS_2$ has been realized, with good memristive properties and excellent stability and reproducibility.

**Thesis structure**

In Chapter 1 will be introduced TMDCs, describing main characteristics, applications and growth techniques, especially when in form of few or single monolayer.

Chapter 2 is devoted to description of all experimental issues, also considering the many characterization tools used in this study, also thanks to the collaboration with other Italian and international groups.

Chapter 3 will describe the study of defects in bulk crystalline 2H-$MoS_2$ by thermal annealing, the effects of sulfur vacancies on electronic properties and functionalization efficiency for an organic molecule.

Chapter 4 will describe all studies related to the synthesis of $MoS_2$ films by IJD. A brief introduction on this new deposition technique will be presented. First results of $MoS_2$ thin film growth on Silicon substrate will define basis of most important studies using Platinum film as a substrate. The complex scenario of electronic, structural, chemical properties will be deeply discussed.

In the end, the conclusion and highlights will be provided in Chapter 5.

# Table of content

## List of figures

## List of Tables

## List of Abbreviations

| | |
|---|---|
| AES | Auger Electron Spectroscopy |
| AFM | Atomic Force Microscopy |
| ALD | Atomic Layer Deposition |
| ARPES | Angle-Resolved Photoemission Spectroscopy |
| BE | Binding Energy |
| CBM | Conduction Band Maximum |
| CPD | Contact Potential Difference |
| CVD | Chemical Vapor Deposition |
| $E_A$ | Electron Affinity |
| EELS | Electron-Energy Loss Spectroscopy |
| $E_F$ | Fermi Energy |
| $E_G$ | Band-Gap Energy |
| $E_{VAC}$ | Vacuum Energy |
| FET | Field Effect Transistor |
| FTIR | Fourier-Transform Infrared Spectroscopy |
| FWHM | Full-Width at Half Maximum |
| HOMO | Highest Occupied Molecular Orbital |
| IE | Ionization Energy |
| IJD | Ionized Jet Deposition |
| KPFM | Kelvin-Probe Force Microscopy |
| LUMO | Lowest Unoccupied Molecular orbital |
| MOCVD | Metal-Organic Chemical Vapor Deposition |
| MUPA | Mercaptoundecylphosphonic Acid |
| PEALD | Plasma-Enhanced Atomic Layer Deposition |
| PL | Photoluminescence |
| PLD | Pulsed-Laser Deposition |
| PVD | Physical Vapor Deposition |
| SAM | Self-Assembly Monolayer |
| SBH | Schottky Barrier Height |
| SECO | Secondary Electron Cut-Off |
| STM | Scanning Tunneling Microscopy |
| STS | Scanning Tunneling Spectroscopy |
| TEM | Transmission Electron Microscopy |
| TMDCs | Transition Metal Dichalcogenides |
| UHV | Ultra-High Vacuum |

| | |
|---|---|
| UPS | Ultra-violet Photoemission Spectroscopy |
| VBM | Valence Band Maximum |
| VOC | Volatile Organic Compound |
| VPD | Vapor Phase Deposition |
| WF | Work Function |
| XPS | X-ray Photoemission Spectroscopy |

# Chapter 1

# Introduction

## 1.1 Two-dimensional materials: overview

Graphene, the first studied two-dimensional (2D) material started its glorious ages as it was mechanically exfoliated and isolated from three-dimensional (3D) graphite in 2004.[1] Graphene is an allotrope of carbon in the form of a single layer of atom in a two-dimensional hexagonal lattice,[1] the thinnest material ever made. Graphene has shown many intriguing properties such as high transparency ($3\times10^3$W/mK), high electrical conductivity (~ $10^4\Omega^{-1}$cm$^{-1}$) and high electron mobility at room temperature (10000 cm$^2$V$^{-1}$s$^{-1}$).[1,2] To discover all those properties, which were not know until isolation of graphene, has become a new challenge and opened up a new prospect in the field of physics. All those distinguishing properties have made graphene an interesting candidate for a variety of applications, including energy storage,[3] solar cell,[4] sensors [5] etc. The intrinsic semi-metallic nature along with the characteristic zero-bandgap has partially limited the application of graphene in logic devices, pushing towards gap opening by defects creation and surface functionalization.

The idea of isolating a monolayer in layered structures, which was born by graphene, drew the attention to other class of materials. The driving idea is that each layered material, when thinned down to its physical limit, exhibits novel properties different from its bulk counterpart due to reduced symmetry, different electron correlations etc. Therefore, at the physical limit these materials are referred to 2D materials.[6]

Beyond graphene, there has been found a variety of 2D materials spanning insulators, semiconductors, metals and even superconductors. In the search for alternative 2D materials with semiconducting properties, the attentions toward transition metal dichalcogenides (TMDCs) has increased in recent years. The high performance of field-effect transistor based on single layer Molybdenum disulfide ($MoS_2$),[7] as one of the most studied members of TMDCs materials, proved the extensive potential that these materials have in the area of 2D nanoelectronics. Moreover, identifying the direct band gap of some TMDCs materials in monolayer form like in $MoS_2$, when accompanied with their other electronic properties such as high career mobility, has introduced them as a promising candidate for opto-electronic

applications.[8]It has been shown also that by tailoring the defects in TMDCs materials, they can be used as catalytic agent in hydrogen evolution reaction.[9] To further broaden the capabilities and application prospect of TMDCs, many studies focused on surface functionalization of these materials. For example, carrier doping of $MoS_2$ nanoflakes by functional self-assembled monolayer (SAMs),[10] tuning photoluminescence of TMDCs through doping via a p-type or n-type adsorbents,[11] demonstrating volatile organic compound (VOC) sensor by using thiol functionalization of $MoS_2$ etc. [12]

Mechanically exfoliated 2D crystals of TMDCs obtained from bulk crystal has been mostly used as the common template for lab-scale demonstration of the most studied devices based on TMDCs materials like field-effect transistors,[7] memory cells,[13] photodetectors,[8,14] piezoelectric sensors[15] and nanopores[16]. Although flakes quality is very high and excellent proof of concept can be obtained in this way, however, the method is suffering critical drawbacks on industrial scale production. To move from laboratory to industrial scale, methods for scalable synthesis of TMDCs should be developed. For this purpose, many studies (see **section** 1.5) have been focused on obtaining large domain of single crystal TMDCs materials via atomic layer deposition (ALD),[17,18] chemical vapor deposition (CVD),[19,20] metal-organic chemical vapor deposition (MOCVD)[21,22] and pulsed laser deposition (PLD)[23–25]. Despite of the many achievements have been made in growth of single crystal TMDCs with controlled thickness, there has been remained a long way to synthesize large area of TMDCs with desirable quality.

Ultimately, to bring TMDCs materials in technologically relevant applications, beside developing methodologies for scalable synthesis of these materials, a tireless work on studying the fundamental physical, chemical and electrical properties of them is still needed.

In this chapter we will describe main physical, chemical structural properties of TMDC, with emphasis on surface electron spectroscopies. A general introduction on applications in electronics, optoelectronics and sensing will be presented, together with the main synthesis and deposition techniques used for these materials. Focus will be pointed to $MoS_2$, with the aim to give a panorama on features and perspectives of this TMDC that will be the necessary background for next chapters.

### 1.2 Properties and applications of TMDCs: the $MoS_2$ case

TMDCs are a class of materials with the formula $MX_2$, in which M is a transition metal from group IV-VI, and X is a chalcogen element. These materials pertaining crystal structure

consist of weakly bonded sandwich layers X-M-X, where a M-atom layer is sandwiched within two X layers and the atoms in layers are hexagonally packed (**Figure** 1-1a).[26]

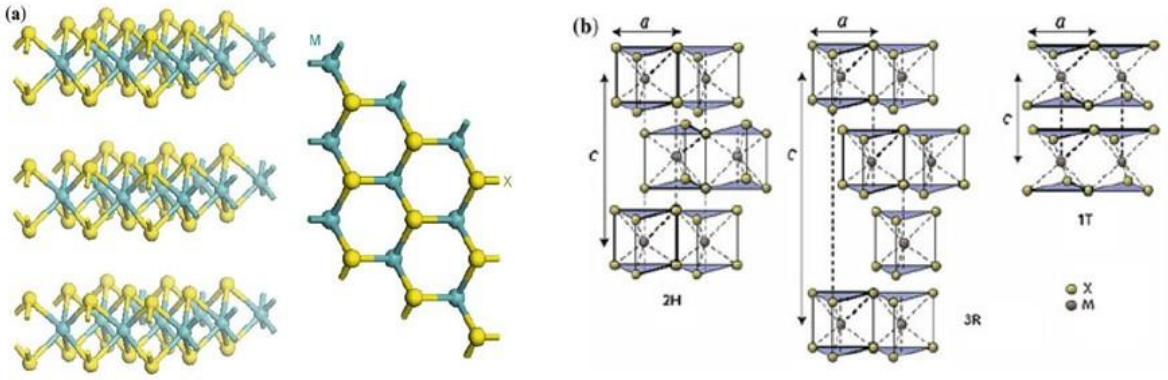


**Figure** 1-1 (a) Three-dimensional schematic representation and top view of a typical $MX_2$ structure, with the chalcogen atoms (X) in yellow and the metal atoms (M) in gray. (b) Schematics of the structural polytypes. Adapted from [26].

Layers are weakly bonded together by a van der Walls interaction to form a bulk structure in a variety of polytypes, which varies in stacking orders and metal atom coordination (**Figure** 1-1b).[26] Concerning $MoS_2$, it is found in 3 different polytypes: (*i*) Semiconducting 2H, the hexagonal symmetry, which constitutes two layers per unit cell with trigonal prismatic coordination. (*ii*) 3R, the rhombohedral symmetry with three layers per unit cell and the trigonal prismatic coordination, and the last, (*iii*) the metallic 1T polytype, with tetragonal symmetry, which constitutes one layer per unit cell with the octahedral coordination. Thermodynamically, the 2H-$MoS_2$ is the most stable among all polytypes,[27] and hence the 2H phase naturally occurs in bulk $MoS_2$.[26]

Referring to TMDCs materials, 2H polytype of Molybdenum Disulfide is the most abundant one in the nature and the most stable one. Bulk $MoS_2$ is a semiconductor material with an indirect band gap of about 1.2eV. An indirect-to-direct transition has been observed in $MoS_2$ band gap when thinned down to monolayer form; the direct band gap of $MoS_2$ found to be 1.8eV.[28] Mobility of monolayer $MoS_2$ found to be at least 200 $cm^2V^{-1}S^{-1}$ at room temperature using hafnium oxide as a gate dielectric, and the current on/off ratio of $1\times10^8$.[7]

The application of $MoS_2$ monolayer in electronic and optoelectronic devices are relying on its electronic properties, such as band structure and density of states. The band structure of bulk 2H-$MoS_2$ calculated from first-principles shows indirect-semiconducting behavior with a band gap of approximately 1.2 eV, which originates from transition from the top of valence band situated at Γ to the bottom of conduction band, half way between Γ and K high

symmetry points (**Figure** 1-2). The optical direct band gap is situated at K point. As the number of layers decreases, the indirect band gap increases (**Figure** 1-2). In the monolayer form, the material changes into a 2D direct bandgap with a 1.9 eV. At the same time, the optical direct gap (at the K point) stays almost unchanged and close to the value of the optical direct band gap (at the K point) of a bulk system.

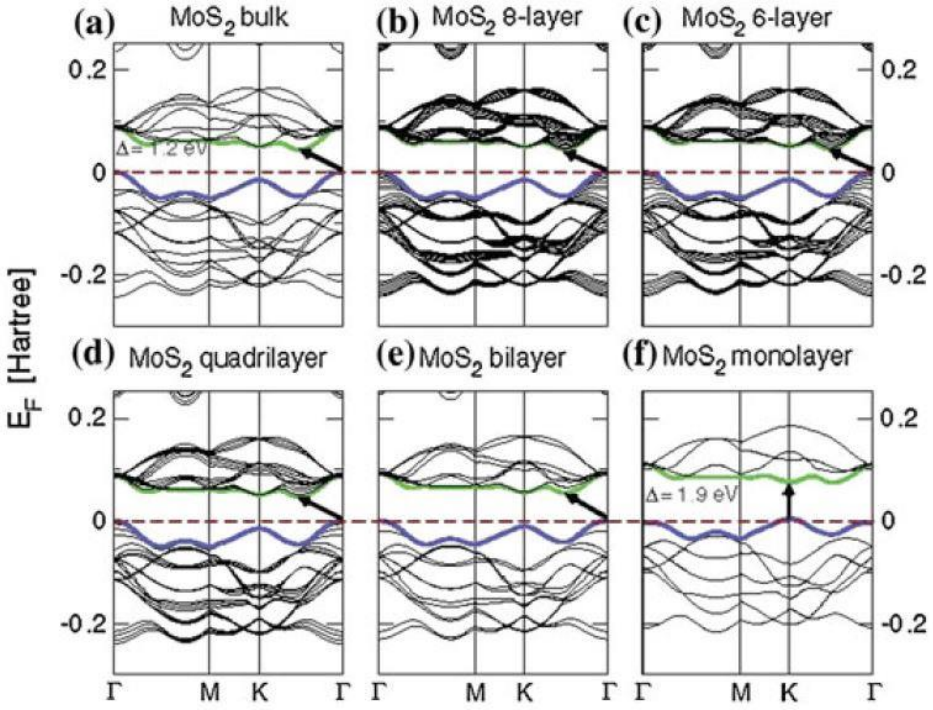


**Figure** 1-2 Band structures of bulk $MoS_2$, its monolayer, as well as, multi-layers calculated at the DFT/PBE level. The horizontal dashed lines indicate the Fermi level. The arrows indicate the fundamental bandgap (direct or indirect) for a given system. The top of valence band (blue/dark gray) and bottom of conduction band (green/light gray) are highlighted. Adapted from [29].

The band structure and bandgaps of $MoS_2$ monolayer are very sensitive to the external strain.[30] Compared to Graphene, a much smaller amount of strain is required to vary the bandgap of $MoS_2$ monolayer. The mechanical strains reduces the bandgap of semiconducting $MoS_2$ monolayer causing a direct-to-indirect bandgap or semiconductor-to metal transition.[30] These transitions, however, significantly depends on the type of applied strain. In addition, the results demonstrate that the homogenous biaxial strain of around 10% leads to semiconductor-to-metal transition in all semiconducting $MoS_2$ monolayer.[31] By considering the accurate bandgap of $MoS_2$ monolayer, the required strain for the transition should be increased.

The optical properties of bulk $MoS_2$ had been thoroughly studied experimentally.[32–36] The calculated absorption spectrum of bulk $MoS_2$ showed that there are two distinct low-energy

peaks at 1.88 and 2.06 eV,[37,38] which were assigned to the direct transition between a split valence band (VB) and the conduction band (CB) at the K high symmetry point of the Brillouin zone. Excitonic effects are important to understand the optical absorption spectrum of nanostructures and two-dimensional materials due to a reduced electron screening.[39]

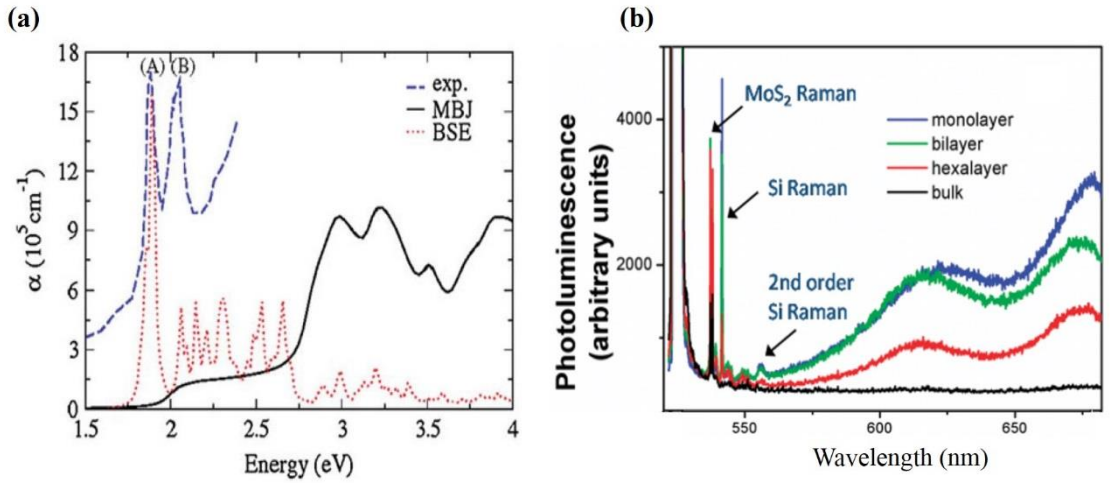


**Figure** 1-3 Experimental as well as calculated absorption spectrum of monolayer $MoS_2$. Adapted from [40]; (b) layer dependence efficiency pf PL in $MoS_2$, adapted from [32].

The detailed calculation on the absorption spectrum at low energy based on the modified Becke-Johnson (mBJ) approximation showed that the $MoS_2$ monolayer has two excitonic peaks at 1.88 eV (A exciton) and 2.06 eV (B exciton), respectively (**Figure** 1-3 a), which are similar to the bulky values and consistent with the experimental data on monolayer.[32,41]

The high luminescence yield in monolayer $MoS_2$ can be attributed to the high binding energy of the A exciton, which strongly reduces the probability that excited electrons decay to the bottom of the CB before recombining.[40] The peaks labeled *A* and *B* agree with the energies of the *A* and *B* excitons, suggesting that they arise from the direct bandgap photoluminescence at the K point. Moreover, the observed optical behavior of in few-layer $MoS_2$ has several unique characteristics. Bulk $MoS_2$ does not exhibit luminescence and has strong direct excitonic absorption at energies much larger than the indirect band gap. These excitonic sates become strongly luminescent in $MoS_2$ monolayer, by they remain at the same transition energies as in the bulk. Photoluminescence of $MoS_2$ monolayer, bilayer, hexalayer and the bulk sample is presented in **Figure** 1-3 b. The PL intensity was found to be the strongest in monolayer $MoS_2$ in spite of the reduced dimensionality.

Many studies have also been carried out to elucidate the lattice dynamic of $MoS_2$. Raman infrared spectroscopy, as a valuable non-destructive and versatile method for structural

characterization, has been widely used to investigate the electronic and vibrational properties of materials. The Raman spectrum is directly related to the lattice dynamics of materials, including phonon dispersion curves, phonon density of states and infrared and Raman active modes. These properties can also be predicted by first-principle calculations using the optimized atomic structure. The Mo atoms in bulk structure of $MoS_2$ occupy sites of $D_{3h}$ symmetry and S atoms obey $C_{3v}$ symmetry. The symmetry of bulk $MoS_2$ is $D_{6h}$, having 24 symmetry elements and 12 irreducible representations. Four second order representations involve the lateral (in-plane) displacements of Mo and S atoms (**Figure** 1-4 c).[42] First order representations recoupled with the displacements perpendicular to the layers of atoms or parallel to the *Z* axis. The $MoS_2$ monolayer has $D_{3h}$ symmetry, 12 symmetry elements, and 6 irreducible representation. In order for an irreducible representation to be infrared active mode, it must create a dipole moment in the system.

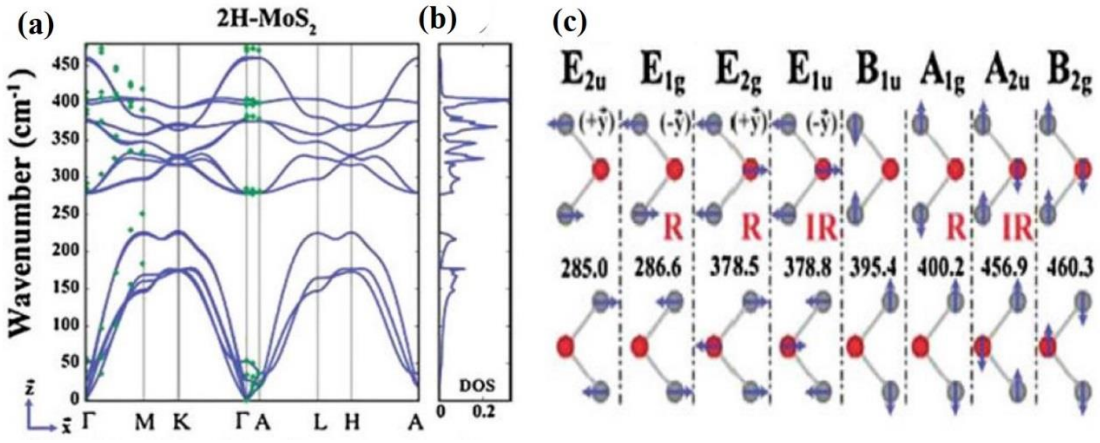


**Figure** 1-4 (a) Calculated phonon dispersion curves of 2H-$MoS_2$, Ω(k) versus k along symmetry directions of BZ, and (b) corresponding density of states, (c) Raman and Infrared active vibrational modes. Adapted from [42].

For bulk $MoS_2$, $E_{1u}$ and $A_{2u}$ and for the monolayer counterpart, E′ and $A_2'$ are the infrared-active modes, respectively. Raman active modes induce polarization or quadruple moment in the lattice. On the other hand, $A_{1g}$, $E_{1g}$ and $E_{2g}$ are the Raman active modes for bulk $MoS_2$, where, $A_1'$, E′ and E″ are the Raman active modes for $MoS_2$ monolayer.[42]

### 1.3 Surface electronic properties of materials: overview

Surface electronic properties of semiconductor materials play a crucial role in electronic and optoelectronic devices; hence to have a comprehensive understanding on the surface energy levels and the approaches to tune their values is of vital importance.

Surface electronic energy levels has been intensively investigated in this thesis applying a variety of characterization technique, including highly surface sensitive photoemission spectroscopy technique, which is the best-known technique to directly measure these parameters. In this section, a brief introduction to the core concepts of the surface electronic properties is given.

The electronic levels and energies of semiconductor material, such as Fermi level, vacuum level, work function, ionization energy or electron affinity are of great importance to leverage the performance of electronic devices, charge carrier injection and transport, carrier density etc. The aforementioned surface energy levels are sensitively dependent on the structure, surface morphology, chemical composition, surface defects, adsorbates etc. It will be discussed that, how a small amount of contamination on a semiconductor, or a shift in molecular orientation at the surface of an organic semiconductor, can vary the work function and vacuum level position by a large fraction of an electron-volt, and considerably impact the electronic properties of the interface. Initially we will introduce the most important surface energy levels and mechanisms that affect these fundamental quantities.

Fermi level ($E_F$) and vacuum level ($E_{VAC}$) position, work function (WF), energy gap ($E_G$), ionization energy (IE) and electron affinity (EA) are parameters of great importance for any electronic material. To a large extent, these parameters are key roles that define the electronic structure of entire interfaces between a material and the outside world and control process of charge exchange and transport across interfaces in all electronic devices.[43] However, there have been a variety of factors causing changes in these values. Among those are purity of material (doped or undoped), crystallographic structure, surface roughness, preparation condition, surface contamination and cleanliness etc.

Schematic illustration of the surface energy levels is given in **Figure** 1-5. For ease of comprehension, the semiconductor is represented with a flat band near the surface, which assumes that there has been occurred no net charge accumulation at or near the surface.

The hole and electron single particle transport levels in inorganic semiconductors are called valence band maximum (***VBM***) and conduction band minimum (***CBM***), respectively.[43] The equivalent terms used for the same parameters in the organic semiconductors are called highest unoccupied molecular orbitals (HOMO) and lowest unoccupied molecular orbital (LUMO). In the following sections in this thesis we will use the first pairs, since we are dealing with $MoS_2$, which is an inorganic semiconductor.

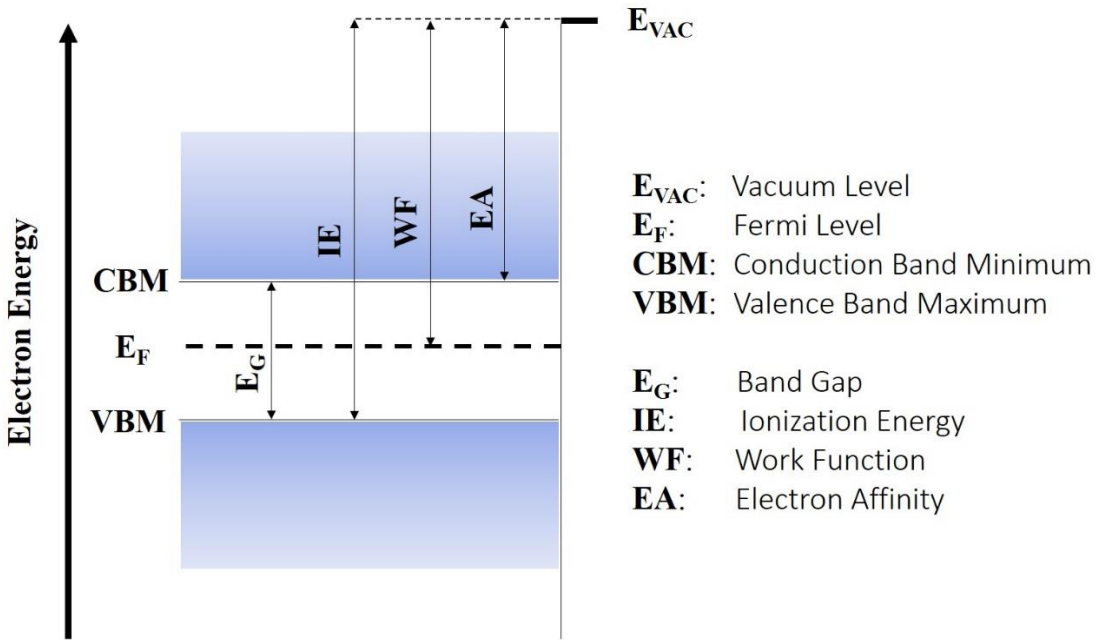


**Figure** 1-5 Energy diagram of a semiconductor with flat bands to the surface.

Band gap (***E_G***) which is also called transport gap, is the energy difference between VBM and CBM energy levels.

Electrons are normally bound to the solid. At the surface of the material, due to presence of an energy barrier, the electrons are prevented to escape (to the vacuum); this energy barrier reaches its maximum values at vacuum level (***E_VAC***). Work function (***WF***). WF is the energy necessary to remove an electron originally at the Fermi level (***E_F***) deep inside the material and place it at rest at a point in free space just outside the surface, i.e at $E_{VAC}$. Photoemission spectroscopy can provide absolute measurements of both $E_F$ and $E_{VAC}$.

The energy difference between VBM and $E_{VAC}$ is the minimum energy required to remove an electron from the system and is known as the ionization energy (***IE***). In the same way, the energy gained by dropping an electron from vacuum level to the CBM, is called electron affinity (***EA***).

$E_{VAC}$ is a key parameter in definition of all parameters described in **Figure** 1-5.

Tuning work function and other surface-related parameters can be obtained through a variety of approaches such as elemental doping and molecular functionalization. The underlying mechanism in entire approaches is attributed to engineering specific dipole.[43,44] As an instance, the deposition on a surface of an acceptor species of an strong electronegative

character results in an charge transfer that creates a surface dipole and raises $E_{VAC}$ and increases WF, IE and EA. Conversely, the deposition of electropositive species has the opposite influence. The magnitude of the effect depends on the charge displacement.

In many studies, it has also been shown that due to the surface charge redistribution also the surface band bending, hence, Fermi level shift also occur, which has also contributions in the total changes of WF, IE and EA.[44,45]

### 1.4 Surface electronic properties of TMDCs: $MoS_2$ case

The surface electronic energy levels and the importance of gaining abilities to tune their quantities has been discussed in previous paragraph. In this section we exclusively, aim to discuss the surface electronic properties of $MoS_2$ also focusing on the influence of adsorbates, defects, ambient exposure etc. A comprehensive understanding on the surface electronic properties, the effective parameters and defining approaches to tune these properties would path the way to exploit the maximum potential of these materials and design high performance electronic devices, i.e. FET, diodes, sensors, based on TMDCs materials.

Surface area of the materials is one of the factors dominating their tendency to interact with external agents, i.e. adsorbates in ambient; in case of layered material, the surface area and hence, the reactivity, reaches its maximum when they are thinned down to monolayer, i.e. when all atoms are exposed to the surface.[46] As a result, the intrinsic physical and chemical properties are no longer expected since the interaction with environmental agents would change them. Work function is a good example, which can be easily modulated by ambient gases and is a key parameter to be considered in designing a variety of electronic and optoelectronic devices based on TMDCs. In recent years, Graphene has been studied from this point of view. It has been shown that, when oxygen molecules adsorbed on a graphene surface, leads to a change in the electrical properties to p-type by trapping the electrons of the host material.[47] However, such sensitivity to the environment can be considered as an advantage from an engineering perspective as means to control the work function of the material.[48]

Lee *et al*.[48] by using Kelvin-probe force microscopy (KPFM), measured the work function of CVD-grown monolayer $MoS_2$ under various ambient conditions (air, oxygen and nitrogen), which was further confirmed by ultraviolet photoemission spectroscopy (UPS).

They could spot a large work function variation of around 0.43 eV by varying the environment from vacuum to $O_2$ exposure. Their KPFM apparatus was operating in ultra-high vacuum (UHV). The measured work function of the monolayer was 4.36 eV in air, which reduced to 4.04 eV under UHV conditions ($10^{-9}$ Torr). The sample was then exposed to $O_2$ gas (3 Torr, gas flow), and it has been observed that, the WF further increased to a higher value of 4.47 eV. They have also introduced $N_2$ to the KPFM chamber and repeated the WF measurement. $N_2$ exposure introduced a negligible change of around 0.02 eV, which indicates that the $N_2$ does not react with pristine $MoS_2$ and hence does not change its surface electronic properties. The energy level diagram of the CVD-grown monolayer $MoS_2$ is given in **Figure** 1-6a, with values calculated from KPFM measurements ($E_G$ value assumed to be 1.9 eV). The values obtained by UPS (He II, monochromatic excitation of 40.813 eV) found to be comparable with the values obtained by KPFM, i.e. $WF_{1L\text{-}MoS2,\ UPS}$= 4.023 eV, $WF_{1L\text{-}MoS2,\ KPFM}$=4.05 eV, as shown in **Figure** 1-6b-c.

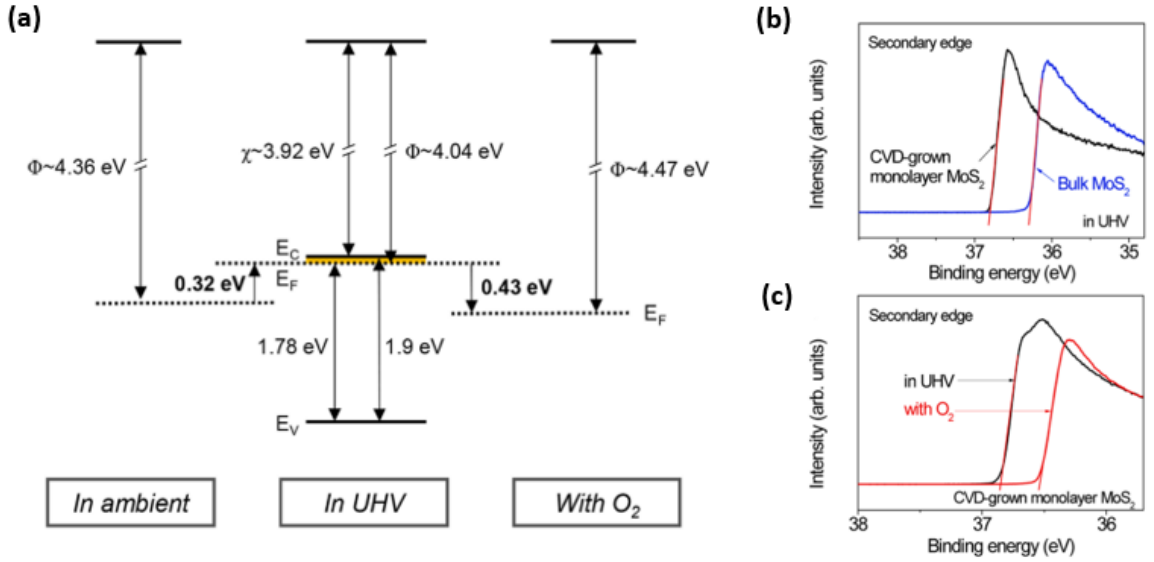


**Figure** 1-6 (a) Estimated band diagrams of the CVD-grown monolayer $MoS_2$ in ambient, UHV, and $O_2$ gas environment. Secondary-edge spectrum from (b) bulk and CVD-grown monolayer $MoS_2$ measured in UHV and (c) CVD-grown monolayer $MoS_2$ measured in UHV and $O_2$ gas environment. Adapted from [48].

The work function of the bulk $MoS_2$ found to be 4.54 eV, which is around 0.5 eV higher than its monolayer counterpart; the influence of $MoS_2$ thickness on WF value will be discussed later in this section. Furthermore, the WF of the sample after $O_2$ exposure measured by UPS found to be slightly smaller than value measured by the KPFM, which is attributed to the desorption of the $O_2/H_2O$ that partially occurred by transferring the sample to the UHV chamber for UPS measurement.

On the other hand, the $O_2$ exposure does not introduce any shift in the VBM level (**Figure** 1-7b), although it causes a significant increase in the WF value (**Figure** 1-6c). This indicates that the $O_2$ exposure does not modulate Fermi level and entire changes in the work function is attributed to the shift of $E_{VAC}$ level. However, according to the valence band spectra given in **Figure** 1-7a , CVD-grown sample appears to have higher VBM, which indicates that this sample is relatively more n-type relative to the single crystal $MoS_2$. This can be attributed to the more defective nature of the CVD-grown sample, which will be discussed later in this section.

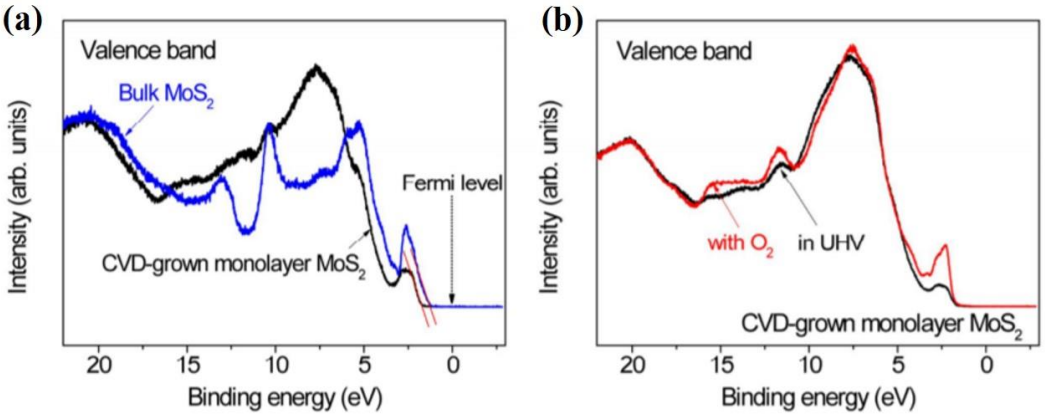


**Figure** 1-7 Valence-band spectrum from the UPS measurement. (a) Bulk and CVD-grown monolayer $MoS_2$ measured in UHV. (b) CVD-grown monolayer $MoS_2$ measured in UHV and $O_2$ gas environment. Adapted from [48].

The influence of layer number and the atmospheric adsorbates on WF of $MoS_2$ has been also been studied by Choi *et al.*[49] They have also used KPFM to measure the surface potential. They have reported that the WF of as-prepared 1 to 6 layers $MoS_2$ nanoflakes were 5.15 to 5.39 eV, increased with increasing the number of layers (**Figure** 1-8).

The gradual increase of the WF by increasing the number of layers has been discussed in terms of the changes in the number of charge carriers due to a variation in charge trapping induced by the surface absorption of foreign molecule. They have also reported that the annealing of flakes at 300$^o$C for 1 h, under continuous argon gas flow, results in reduction of WF, which they have attributed it to the desorption of atmospheric adsorbates from the surface. Adsorbates like $H_2O$ and $O_2$ act as electron withdrawing agents and hence, making the underlying $MoS_2$ substrate more p-type.[47]

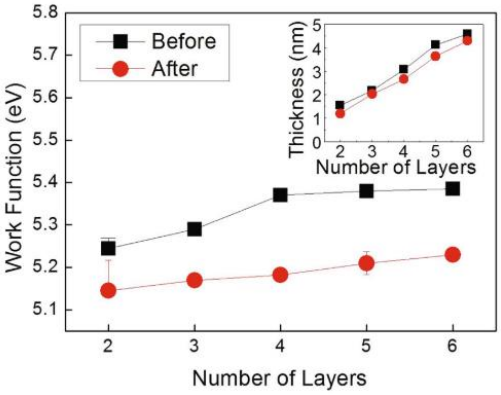


**Figure** 1-8 Layer-number-dependent work function of $MoS_2$ nanoflakes before and after heat treatment. The values were extracted by using a line profile analysis of the acquired KPFM data. The inset is the thickness as a function of the number of layers in the $MoS_2$ nanoflakes. After heat treatment, the thickness was decreased by ~0.3 nm for all layer numbers. Adapted from [49].

In another work, Kim *et al.*,[50] has also studied the WF of CVD-grown $MoS_2$ of different thickness. According to the results obtained by KPFM and XPS measurements, they have reported that the $MoS_2$ surface potential increases by 0.15eV when the number of layers is increased from 2 to 12, as evidenced by contact protentional difference (CDP) distribution obtained by KPFM in mapping mode (**Figure** 1-9a). They have claimed that the WF shift is due screening effect of oxygen and water molecules adsorbed on the surface.

To further evaluate the influence of foreign molecule on WF of $MoS_2$, they have carried out photoemission spectroscopy with in-situ annealing under ultra-high vacuum condition. The annealing was for 10 min at 250$^o$C. After annealing, XPS measurements has shown no changes on the S/Mo ratio but the C1s and O1s core levels significantly decreased, which is a clear indication of foreign molecule desorption from the $MoS_2$ surface. In accordance with the work of Choi *et al.*[49], thermal treatment reduces the work function of $MoS_2$ with different thickness (**Figure** 1-8), with Mo3d and S2p core levels experiencing downward rigid shifts.

Regarding the electronic devices based on TMDC materials, the $MoS_2$ channel material formed an interface with the gate dielectric which can tune the electronic properties of the channel material.[51–53] Leonhardt *et al.*,[51] investigated the doping effect of aluminum oxide capping layer and silicon oxide back gate layer on field effect transistor based on $MoS_2$, $ReS_2$ and $WS_2$. They have highlighted that, deposition of $Al_xO_y$ capping layer and interface between silicon oxide layer and TMDC channel material, results in doping of both synthetic and single crystal natural $MoS_2$. They hypothesized that the doping originates from donor states in the band gap of $Al_xO_y$ and interface contaminations, which can donate electrons depending on the position of CBM of the TMDCs.

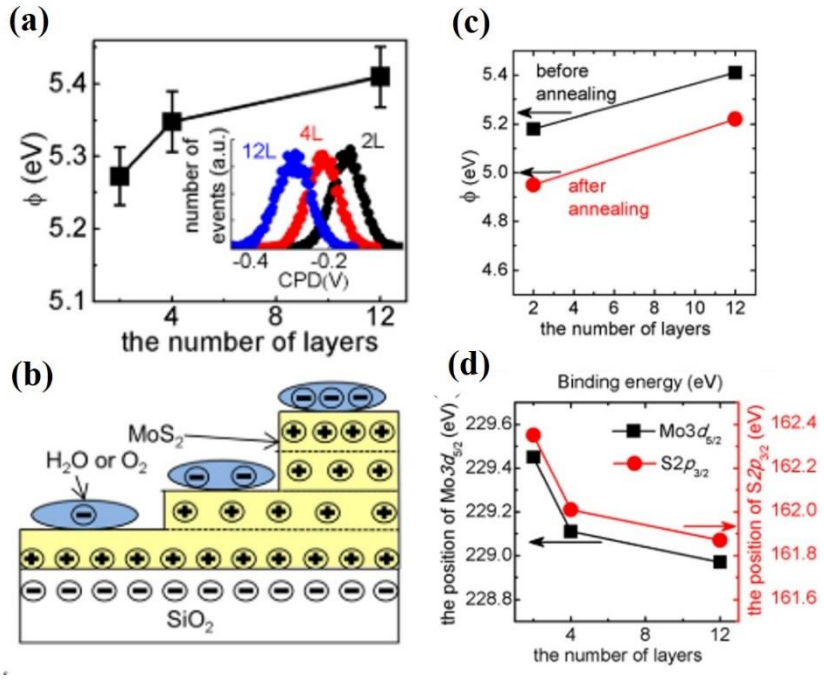


**Figure** 1-9 (a) Work functions of the $MoS_2$ films as a function of layer thickness. Inset: work function distribution of each CPD image. (b) Schematic diagram of the $MoS_2$ charge distribution when $O_2$ or $H_2O$ is adsorbed, (c) Work function of $MoS_2$ films vs. thicknesses before and after annealing. (d) The peak positions of $Mo3d_{5/2}$ and $S2p_{3/2}$ vs. thickness. Adapted from [50].

One of the major challenges in designing high performance electronic component like $MoS_2$-based FETs, is the high contact resistance, which arises due to high Schottky barrier height (SBH). In this concept, the WF of the metal and electron affinity (EA) of the semiconductor, i.e. $MoS_2$ and the interface condition are involved. Contact resistance dominates the charge transfer between metal and semiconductor and hence, significantly influences the performance of FET (**Figure** 1-10).[54]

However, this notable SBH leads to a considerable $R_C$ and a performance degradation (i.e. low field mobility) in two-terminal $MoS_2$ FET, since a large portion of the applied potential between source and drain, dropped across this $R_C$. The presence of SBH in $MoS_2$ FETs has been experimentally verified in several works.[55–61] The origin of the charge injection/extraction barrier are thought to be due to a strong Fermi level pinning (FLP) effect at the contact metal/$MoS_2$ interface.[54,62] Many microscopic and spectroscopic studies on $MoS_2$ flakes revealed the high concentration of defects and impurities, such as sulfur vacancies (SV), which are thought to be responsible for FLP.[57,63] It is due to the pinning effect that most of the metal-contacted $MoS_2$ FETs typically show unipolar n-type behavior as the metal Fermi level gets pinned near the CBM of the $MoS_2$ irrespective of the metal WF.

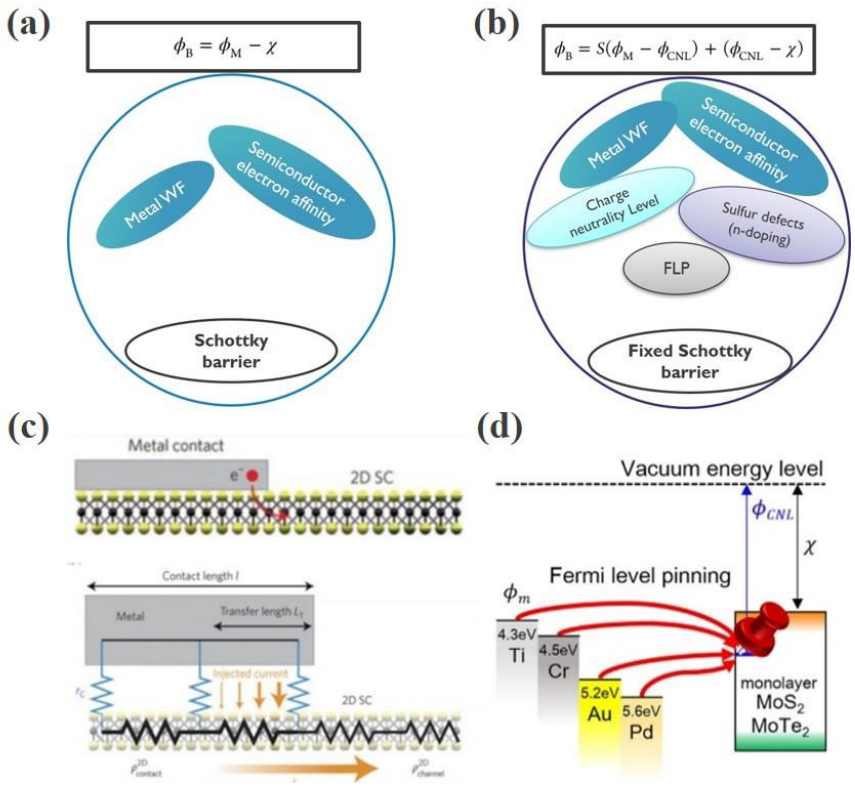


**Figure** 1-10. (a) Parameters involved in Schottky barrier height; formula is valid in conventional metal-semiconductor junction, (b) FLP introduced to Schottky Mott rule, developed for $MoS_2$-metal junction, (c) Schematic illustration of the contact length (LC), transfer length (LT) and current injection near the metal contact/2D TMDC interface edge, also shown in the resistor network model. Adapted from [54]. (d) Band diagram at the interface, indicating that regardless of the metal contact of various WF, a fixed SBH obtained. Adapted from [61].

Many approaches have been implemented to tackle the drawbacks arises due to fixed SBH. Among those are transference of the metallic electrodes (**Figure** 1-11a), since it is believed that deposition would partly damage the semiconductor channel and yield a more defective surface (**Figure** 1-11b), which makes it more susceptible to Fermi level pinning.[64]

Through this approach, one of the highest electron mobility ever reported in the literature for $MoS_2$ FET, 260 $cm^2V^{-1}s^{-1}$ with Ag electrode was obtained.

In another work, Kappera *et al.*[59] could significantly reduce the contact resistance from 1.1 to 0.2 kΩ.µm and hence increase the electron mobility from 19 to 46 $cm^2V^{-1}s^{-1}$ of $MoS_2$ FET by applying a phase engineering approach, in which they transformed the $MoS_2$ phase from semiconducting 2H to metallic 1T phase at the contact region and then deposited the metal electrode on the 1T phase region.

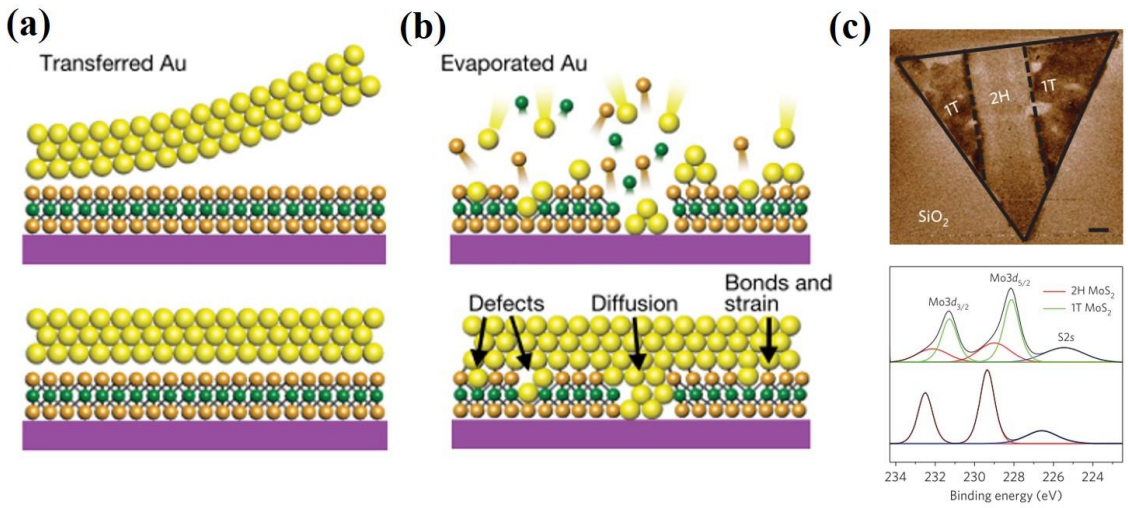


**Figure** 1-11 Schematic illustrations of vdW integration of metal–semiconductor junctions: a comparison between transference (a) and deposition (b) of Au metal contact, with defective and alloying interface. Adapted from [64]. (c) Photoluminescence map of the $MoS_2$, evidences the partial phase transformation (up); XPS Mo3d core level, confirming a metallic 1T phase of $MoS_2$ (down). Adapted from [59].

Many other approaches like interface engineering i.e. insertion of graphene[65] and metal oxide[66] in metal-semiconductor interface, elemental doping, molecular functionalization etc.[67–72] have been widely investigated in several studies to tackle the high contact resistance in metal-$MoS_2$ junction.

In spite of all the efforts to control the metal-$MoS_2$ interface to compensate the high contact resistance, the contact resistance and electron mobility of $MoS_2$ FET still drops far below its theoretical value and needed to be improved.[73]

However, in the above discussed challenge, it has been pointed out that, surface defects and the consequent surface electronic levels are taking a key role and we believe that, in order to take the right action, to fully compensate the drawbacks arises from surface electronic properties, a more detailed investigation should be carried out to understand the relationship between surface defects and surface electronic levels. In the following section, the role of defects on surface electronic states will be briefly discussed.

### 1.4.1 Defect-dominated surface electronic levels tuning

Due to the extremely high surface-to-volume ratio of 2D materials, understanding their surface characteristics is crucial for practically controlling their intrinsic properties and fabricating devices based on them. TMDCs materials, i.e. $MoS_2$, are expected to have an inert surface because of the absence of dangling bond. Nevertheless, many microscopic and spectroscopic studies on $MoS_2$ revealed the presence of considerable number of defects of

several types on their surface; among those, sulfur vacancies found to be the most abundant one. It has been claimed that the sulfur defects are negatively charged and hence, is considered as one of the key roles, dominating the surface electronic levels and is thought to be the origination of many (undesired) phenomenon observed in devices based on 2D-$MoS_2$, i.e. intrinsic unipolar n-type behavior of $MoS_2$ FET, high metal-$MoS_2$ contact resistance due to FLP, which have been discussed in previous section.

In different works, a wide range of characterization techniques such as scanning tunneling spectroscopy/microscopy (STM/STS),[57,63,74] angle resolved photoemission spectroscopy (ARPES),[75] X-ray photoemission spectroscopy (XPS)[63,76] have been used to experimentally investigate the electronic nature of the defects.

In previous section, the role of defects on metal-$MoS_2$ contact-related phenomenon has been highlighted. The majority of recent studies reported n-type behavior with fixed SBH for both high WF (i.e. Pt) and low WF (i.e. Al) metals.[77–79] This behavior is not typical of metal/semiconductor contacts without chemical reactions changing the interface. This has been attributed to the Fermi level pinning close to the conduction band of $MoS_2$,[80] but the underlying mechanism is still not well understood. Here on we would like to put further emphasis on the role of $MoS_2$ defects on contact-related undesired phenomenon of FLP and elucidate the underlying mechanism.

In one of the most cited work, Mcdonnell *et al.*,[63] found that intrinsic defects in $MoS_2$ dominates the metal/$MoS_2$ contact resistance and provide a low Schottky barrier independent of metal contact WF. Moreover, they have shown that $MoS_2$ can exhibit both n-type and p-type conduction at different points on a same sample. They have claimed that these variations in doping are defect-chemistry-related and are independent of contact metal. To adjust a meaningful correlation between the varying chemistry, defects and conductivity of each point, they obtained the core level spectra and hence the stoichiometry by XPS measurement. The upper row graphs in **Figure** 1-12 are attributed to the region showing n-type behavior (**Figure** 1-12 a-d) with Fermi level close to the CBM (**Figure** 1-12 c), low concentration of bright (metallic-like) defects (**Figure** 1-12 b) and stoichiometry found to be 1.8:1 (S/Mo), which means that the measured spot is highly sulfur deficient. Regarding the properties of other spot given in the lower graphs of **Figure** 1-12, it can be seen that, the region is dominated by high concentration of dark defects (**Figure** 1-12 f), with sulfur rich

stoichiometry of around 2.3:1 (S/Mo)and p-type behavior with Fermi level close the VBM (**Figure** 1-12 g).

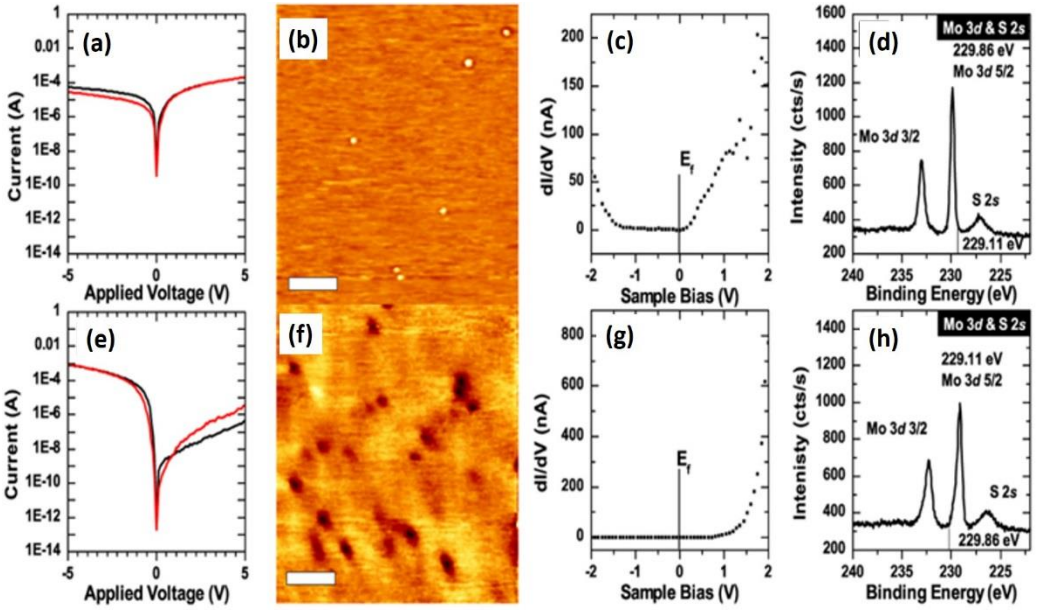


**Figure** 1-12 Correlation of I-V characteristics with STM, STS, and XPS acquired in two spots (a-d and e-h). I-V characteristic showing n-type (a) and and p-type (e) behavior. STM acquired with bright/dark defects (b) and high concentration of dark defects (f) observed. STS acquired showing the Fermi level close to (c) and >1eV far (g) from the conduction band. XPS (d,h) Mo 3d and S 2s core-levels. Adapted from [63].

The variability of electronic properties across the surface of $MoS_2$ found to be quite high, that a movement in the range of few hundreds of nanometers leaded to a shift in the Fermi level and XPS core levels position in the range of 1 eV and 0.8 eV, respectively.

The bright and dark defects and the consequent Fermi level position and electronic behavior type has also been discussed by other researchers.[70,74,81] Park *et al.*[70] utilized STM/STS measurement to investigate the doping effect of sulfur vacancies. They have revealed that the sulfur vacancies can be observed on the planes of CVD-grown $MoS_2$ ML grown on highly oriented pyrolytic graphite (HOPG). Their STM measurements were performed in an ultra-high vacuum (UHV) at 100K. As depicted in **Figure** 1-13, the STM images displays pinholes in the terrace of a ML $MoS_2$ flake. Investigating the size of these pinholes, they can be attributed to the few missing S toms or both missing S and Mo atoms. I-V spectra obtained at various distance from the defect points shows gradual shifting of Fermi level toward CBM, means the material shows more n-type behavior adjacent to the defect sites.

In another work, Siao *et al.*,[75] combined STS and ARPES measurement to reveal the doping effect of sulfur vacancies. They have shown that the surface of high-quality synthesized $MoS_2$ is a major n-doping source. The surface electron concentration of $MoS_2$ is nearly four

orders of magnitude higher than that of its inner bulk. Substantial thickness-dependent conductivity in $MoS_2$ nanoflakes was observed.

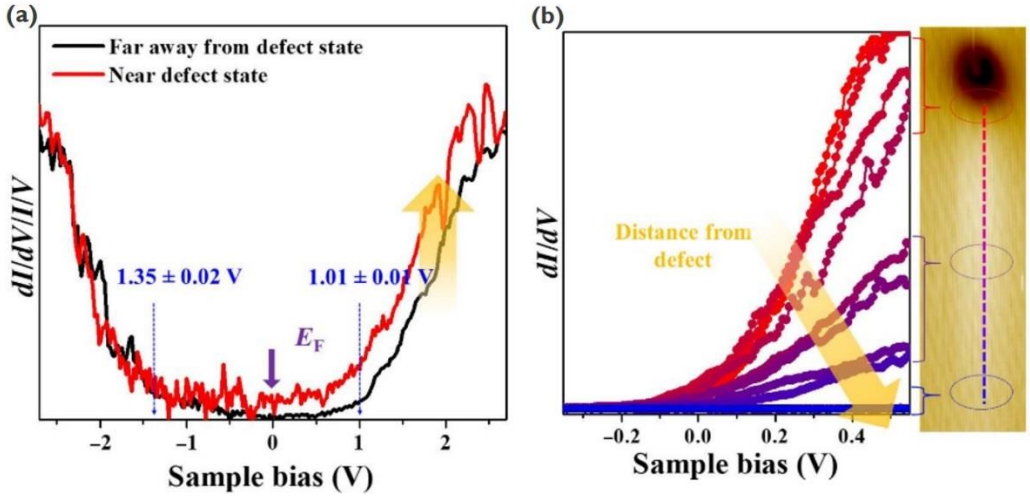


**Figure** 1-13 STMS/STS analysis of a bare ML $MoS_2$ surface deposited on HOPG. (a) STS measured on the terrace of a ML $MoS_2$; the black spectra are measured far away from the defects, whereas the red spectra are measured near a defect. (b) Spatial STS near the CB edge as a function of the distance from the defect. Adapted from [70].

The STM/STS results confirms that the $MoS_2$ surface is highly n-doped. Furthermore, the band alignment diagram (**Figure** 1-14 d) shows that the energy difference between the Fermi level and CBM is relatively uniform over the whole probing range, which is around 100nm, indicating that the metal-like surface is not confined to a few local defect areas. Formerly, in this section we have highlighted the presence of two opposing types of defects on the surface,[63] but according to Siao *et al.*,[75] as they have carried out the measurement in a long range (~100 nm), n-doping source found to be the dominating source on the surface of $MoS_2$, as given in **Figure** 1-14 d and f.

Considerably, the fresh surface did not exhibit metal-like characteristics, as the $E_F$ position is located far from the CBM (**Figure** 1-14 e and h). This result indicates that the fresh surface has a lower electron concentration and is likely intrinsic, different from the metallic non-fresh surface that has been exposed to air.

Notably, by a surface long term exposure to air, the $E_F$ position shifted to near the conduction band (**Figure** 1-14 i) indicating a metallic character. The band alignment diagram in **Figure** 1-14 f exhibits uniform doping in the 100nm probing range.

They have also investigated the probable origin of surface electron accumulation and surface electronic properties of bulk single crystal $MoS_2$ by ARPES. The band mapping results

shows a clear shift in the VBM relative to the Fermi level when the surface condition changes from pristine via the ex-situ fresh to the in-situ fresh state (**Figure** 1-15 a-c). The normal emission spectra at the Γ point is depicted in **Figure** 1-15 d. The spectrum shows a very sharp valence band at -0.75 eV binding energy in the in-situ fresh surface.

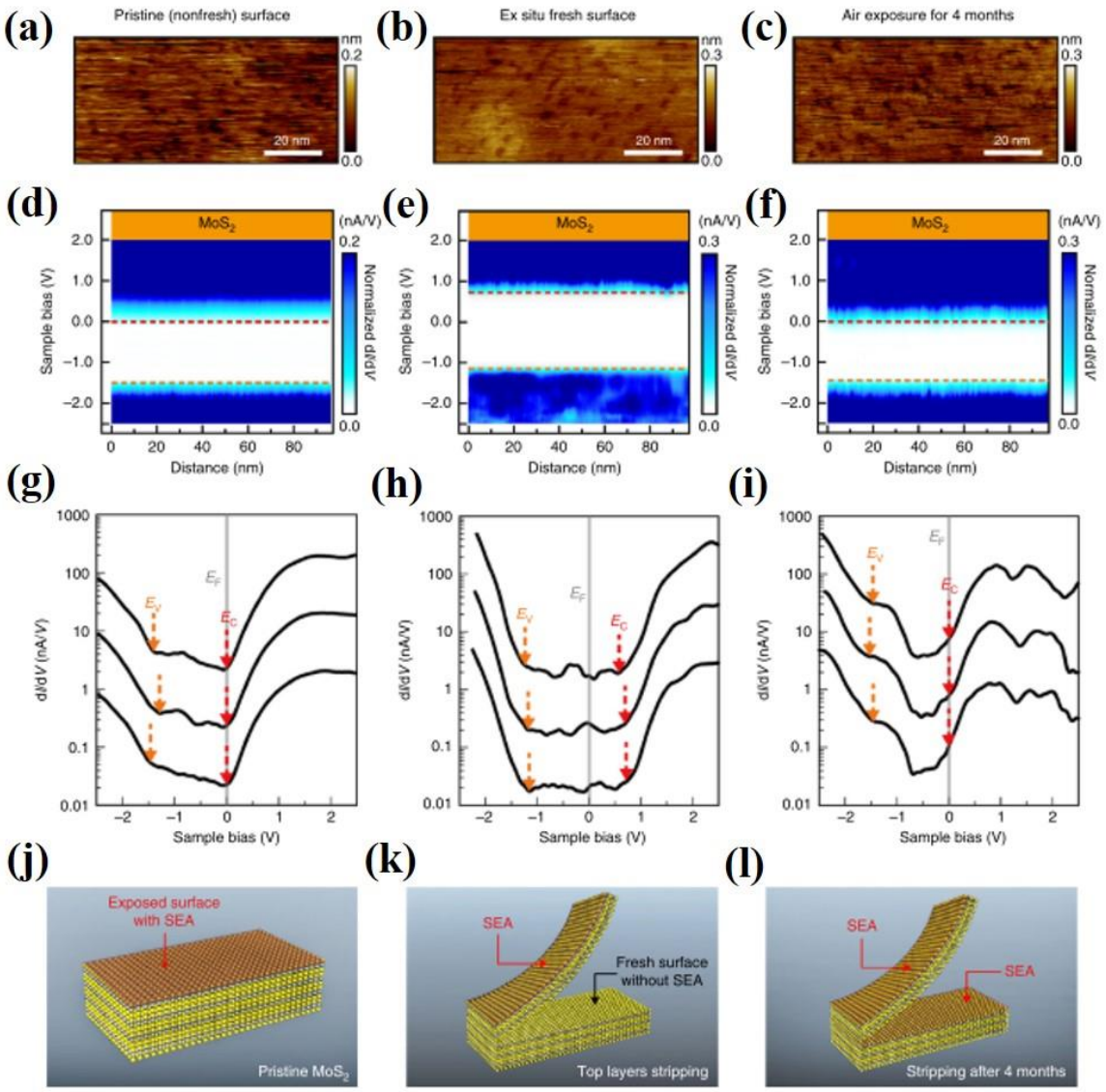


**Figure** 1-14 STM/STS characterization and surface electron accumulation (SEA) of a $MoS_2$ single crystal. (a-c) STM image, (d-f) band alignment, and (g-i) dI/dV curve measurements for the non-fresh surface of a pristine $MoS_2$ crystal (a,d,g), the fresh surface of an $MoS_2$ crystal (b,e,h), the fresh surface of an $MoS_2$ crystal exposed to air for four months (c,f,i). (l) Schematic showing the SEA formation at the fresh surface of $MoS_2$ after four months exposure to air. Adapted from [75].

Assuming the $E_G$~1.3 eV, the corresponding Fermi level position would be close to the middle of the band gap, so called, intrinsic Fermi level. Observations indicate that the new surface cleaved in the UHV has a nearly perfect structural quality and highly insulating nature.

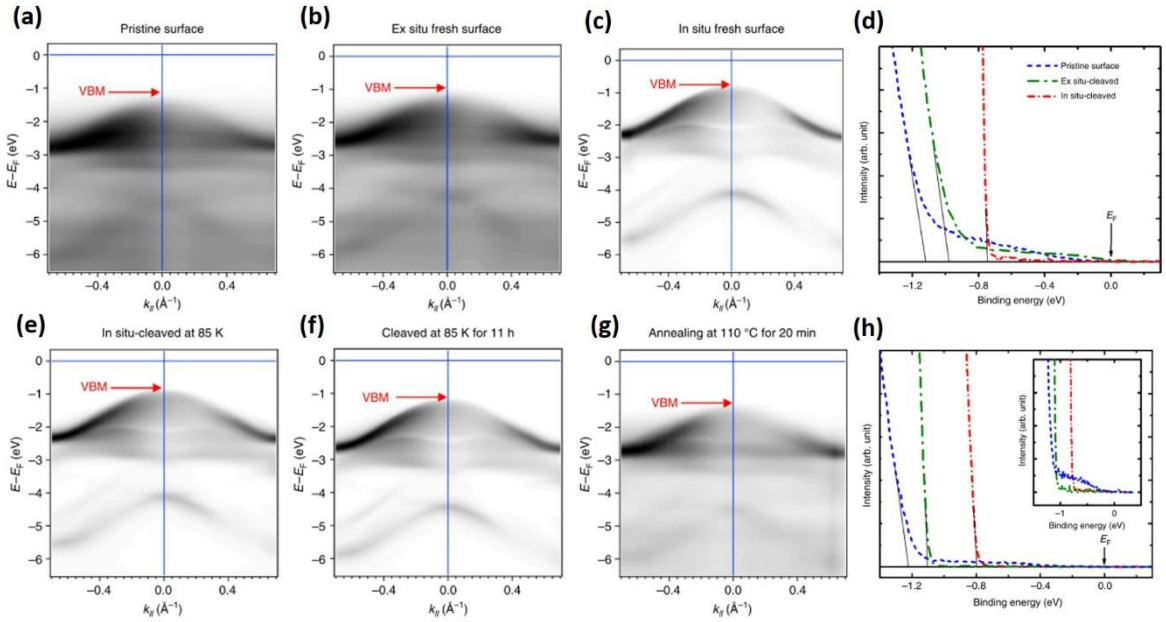


**Figure** 1-15 ARPES characterization of single crystal $MoS_2$ at different conditions. The E versus $k_{\parallel}$ valance band measurements for pristine (a), ex situ (b) and in situ-cleaved fresh surfaces (c), (e) in situ-cleaved surface at 85 K, (f) the in situ-cleaved surface at 85 K for 11 h, and (g) the in situ-cleaved surface at 85K after annealing at 110 °C for 20. (d,h) The normal emission spectra at the Γ point for different cases. Adapted from [75].

Once the surface is exposed to the atmosphere, the bandgap shows a considerable shift to -0.98 eV for the ex-situ fresh surface (exposure time around 10 min). They have shown that, even further exposure of the surface to ambient would significantly decrease the band gap to -1.2 eV. The higher Fermi level position indicates a much higher surface electron accumulation and means that the SEA decreases from pristine to ex-situ and in-situ cleaved surface, respectively (**Figure** 1-15d). The have claimed that, the surface ambient exposure may be accompanied with two reactions, sulfur loss and adsorption of foreign molecules, which are thought to be the origin of surface electron accumulation (SEA). To the best of our knowledge, this was the sole time ever reported in the literature that desulfurization widely occurs by ambient exposure of $MoS_2$. To further prove this argument, they have annealed the sample up to 100$^{o}$C for 20 min and repeated the ARPES measurement. The VB (**Figure** 1-15 g) and its corresponding normal emission spectrum (**Figure** 1-15 h) indicate that the VBM further shifts to the energy position at -1.22 eV,so that the Fermi level can easily be pushed to the near CBM by accelerating the sulfur loss process at higher annealing temperature.

On the other hand, the role of sulfur defects on surface electronic properties of $MoS_2$ has been investigated in several other works, in which, the defects have been intentionally introduced by ion irradiation[71,82–84] or annealing.[83,85,86]

Considering the electronic properties of intentionally introduced defects, at variance with the results formerly discussed in this section, it has been clearly evidenced that the introduction of sulfur vacancies by i.e. $Ar^+$ irradiation, would result in a downward rigid shift of the core levels (obtained by XPS analysis) and hence yielding a more p-type $MoS_2$. As an instance, Ma *et al.*[82] sputtered $MoS_2$ film of a single layer thickness by low-energy argon ion, which makes the selective removal of sulfur atoms possible. **Figure** 1-16 a and b show the simultaneous downward shift of the Mo3d and S2p core levels, which is an indication of Fermi level tuning. In other word, the ion irradiation and the consequent formation of sulfur vacancies shifted the Fermi level closer to the VBM, an indication of p-doping of $MoS_2$. To account for the surface charging, the spectra at different sputter times were aligned so that the Si 2p peak remains at constant energy (**Figure** 1-16 c).

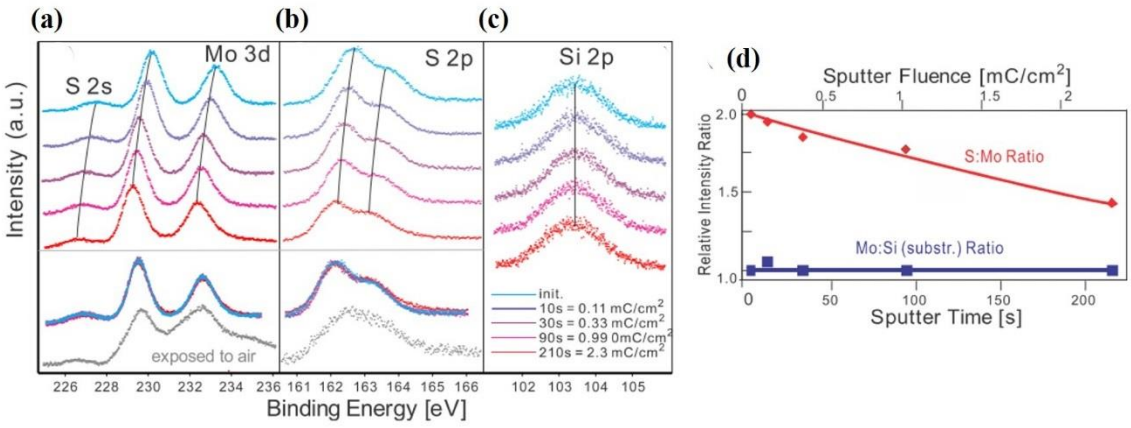


**Figure** 1-16 XPS spectra of (a) the Mo 3d-S2s, (b) the S 2p state, and (c) the Si 2p state. The spectra (from the top to the bottom) were acquired after increasing sputtering. (a) and (b) show spectra scaled and shifted for the best overlay of the peak shape, as well as the corresponding spectra after exposure to air. (d) Intensity of the Mo XPS signal referenced to the substrate Si peak (normalized to 1), and the S/Mo XPS ratio (normalized to 2) as a function of sputtering time. Adapted from [82].

Last but not least, in another work, Choi *et al.*,[84] sputtered the $MoS_2$ surface by e-beam to introduce sulfur vacancies and then, they attempted to recover the surface electronic properties by thiol functionalization. They have used XPS analysis to trace the core level changes. They have also investigated the influence of defect introduction and functionalization on the performance of $MoS_2$ FET. They have also shown that due to sulfur removal, both S2p and Mo3d core levels experienced downward shift, which is a clear evidence of Fermi level shift toward VBM. However, as illustrated in **Figure** 1-17 thiol

functionalization could have partly recovered the modified surface electronic properties through passivating the sulfur defects. They have used thiol-terminated molecule with carbon chain comprising 12 atoms, the molecule is labeled as C12 in **Figure** 1-17.

Considering the works have been carried out on the effect of sulfur defects on surface electronic properties of $MoS_2$, it has been found that in the many investigations based on highly surface sensitive photoemission spectroscopy, introduction of defects by either sputtering or annealing, results in a shift of Fermi level closer to the VBM, which is in contrary of the results obtained by scanning tunneling spectroscopy analysis, in which the shift of Fermi level closer to the CBM is observed.

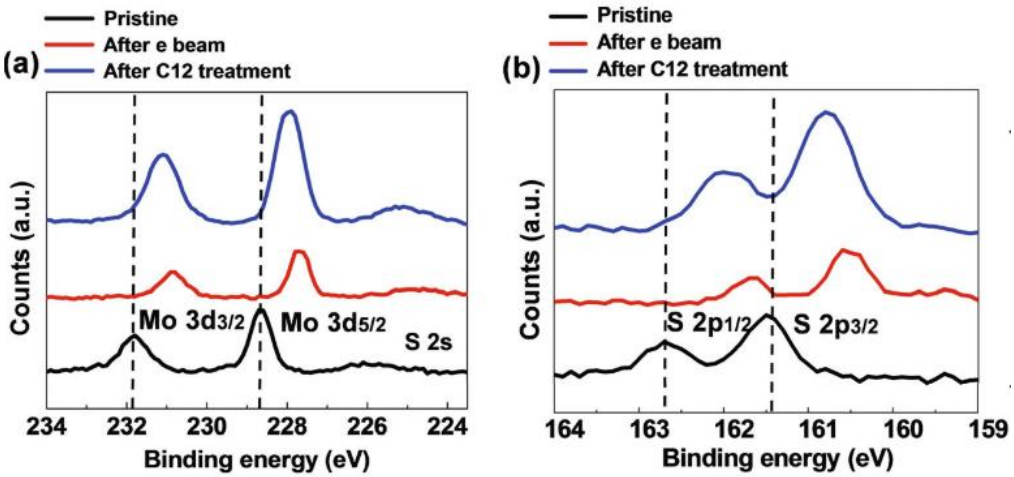


**Figure** 1-17 (a) XPS spectra of Mo 3d and (b) S2p for pristine, e-beam irradiated, and C12-treated $MoS_2$. Adapted from [84].

Regardless of the conflict in the literature, on the role of defects on defining surface electronic properties of $MoS_2$, which was discussed previously, it's well understood that, defects would deteriorate the surface electronic properties and hence the performance of devices based on these materials. Molecular functionalization has been widely used to overcome the challenges arose due to defects. Due to the considerable potentials, molecular functionalization provides for both studying and tuning the electronic properties of TMDCs materials, we will briefly review the most relevant molecular functionalization approaches and the obtained results on defect passivation and controlling the surface electronic properties of $MoS_2$.

### 1.4.2 Molecular functionalization

Functionalization of the TMDCs materials through binding of atoms, molecules or molecular groups has also been under intensive investigation in recent years.[35,87–92] Functionalization offers an efficient way to modify the electronic, chemical, optical and mechanical properties of nanostructure, and to provide new functionalities.

As formerly discussed, defects found to be responsible for fixed SBH in metal-$MoS_2$ contact, increasing the contact resistance and prevent tuning Fermi level to obtain a bipolar $MoS_2$ based FET. Moreover, sulfur defects act as scattering sites in FET channel, reducing the electron mobility of the device.[67] To passivate the surface and control the electronic properties of TMDCs material, many approaches, i.e. molecular functionalization[67,70,91,93–97] and plasma treatment[85,98–100], have been widely studied.

Among the diverse routes, thiol functionalization found to be quite facile and effective. In this approach, molecule with S-H (thiol) tail-group tends to react with the sulfur defects on the surface of $MoS_2$ and fill the vacancy and hence passivate the surface, as also revealed by theoretical studies.[93] The molecule is usually accompanied with a functional group as well, which can bring a variety of capabilities, i.e. sensing and doping towards $MoS_2$ multifunctionality. This is also a way to passivate the negatively charged sulfur defects and recover a perfect surface, as in many studies that exploited thiol functionalization.[67,101–103] Some other used structures of molecules with electron withdrawing capability.[70] However, due to the scope of this thesis, we will just focus on the interaction of molecules with the $MoS_2$ and the consequent surface electronic level changes.

Kim *et al*., investigated the formation of an organic-inorganic van der Waals interface between a monolayer of titanyl phthalocyanine (TiOPc) and a ML of $MoS_2$ as a defect passivation method. They have found that a strong negative charge transfer occurred from $MoS_2$ to TiOPc molecule. They have investigated the influence of charge transference in organic-inorganic interface by STM measurement (**Figure** 1-18). They have revealed that such defect passivation would results in an increase in the $I_{ON}/I_{OFF}$ (which is the ratio of maximum available drain current and the OFF current) in a back-gated $MoS_2$ transistor for two orders of magnitudes, whereas the degradation in the photoluminescence signal is suppressed (**Figure** 1-19). According to **Figure** 1-18c and d, as the STM tip approaches a TiOPc molecule, the Fermi level moves away from the CBM to the middle of the band gap. The Fermi level movement continues to next to the VBM when the tip reaches the molecule.

Based on this observation, they have concluded that, the excess negative charge on the surface of $MoS_2$ is transferred to TiOPc molecule. The electrical characteristics of a four-point back gated single layer $MoS_2$ FET with and without a TiOPc passivation layer is illustrated in **Figure** 1-19 a. Transfer curve of bare $MoS_2$ is showing a threshold voltage ($V_{th}$: is the minimum necessary voltage needed to be applied in FETs to create a conducting path between source and drain) of about -14V with $I_{ON}/I_{OFF}$ ratio of $10^4$. $V_{th}$ is undesirably shifted to the negative voltage, which is an indication of sulfur vacancies presence in the channel.[104]

Annealing at UHV further decrease the $I_{ON}/I_{OFF}$ ratio. Conversely, after the deposition of TiOPc ML on $MoS_2$, the $I_{ON}/I_{OFF}$ ratio improves to greater than $10^7$, because of 100x reduction of the OFF-state leakage, with the $V_{th}$ positively shifted to 10 V because the TiOPc compensates for the excess charge.

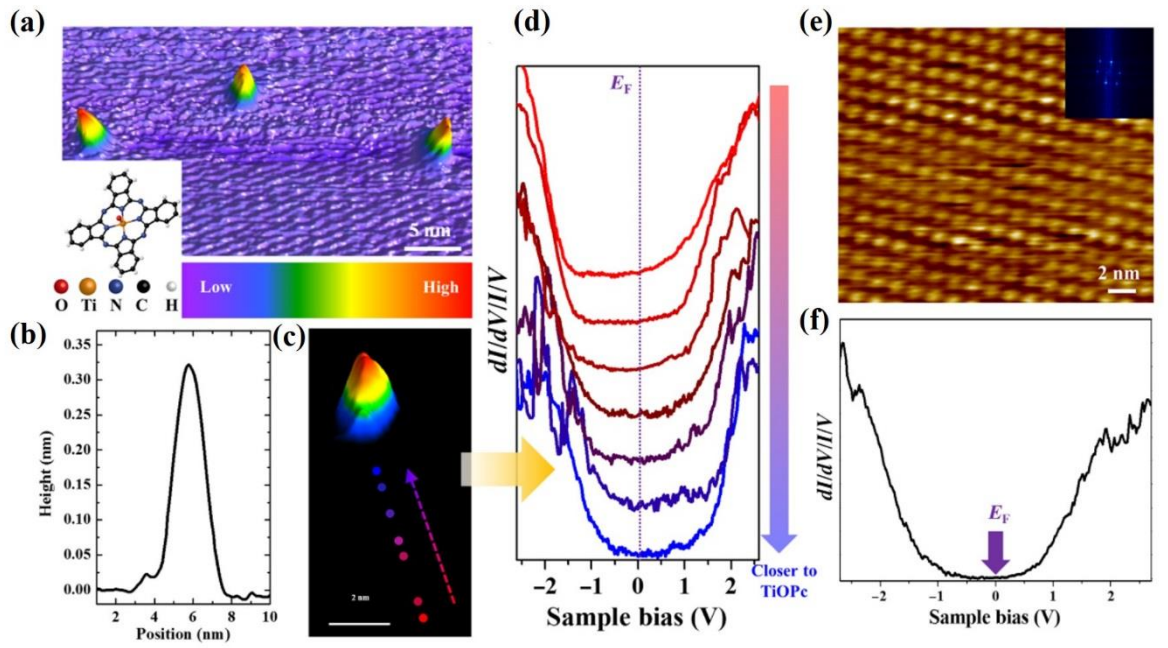


**Figure** 1-18 TiOPc/$MoS_2$ Interface studied by STM/STS. (a) Few TiOPc molecules deposited on a $MoS_2$ ML at 300 K (Vs =2 V, It = 30 pA). Inset: molecular structure of TiOPc. (b) Cross-sectional line trace of an adsorbed TiOPc molecule. (c) Single TiOPc adsorption with a black background. (d) Subset of dI/dV/I/Vspectra taken along the dashed arrow in (c). (e) Full-coverage ML TiOPc on a ML $MoS_2$ and corresponding Fourier transform (Vs =2V, It =50pA). (f) STS of ML TiOPc on aML$MoS_2$. Adapted from [70].

Deposition of TiOPc molecule does not degrade the PL emission (**Figure** 1-19 b). The deposited molecule on annealed $MoS_2$, made no changes in the FWHM, but an increase in the intensity, relative to the annealed counterpart. In addition, a red shift is also observed, which is consistent with the blue shift from bare $MoS_2$.

In another work, Yu *et al.*,[67] applied a low temperature thiol chemistry route to repair the sulfur vacancies and hence, improving the interface in ML $MoS_2$ FET, which results in a significant reduction of the charged impurities and traps and increasing the mobility up to around 80 $cm^2V^{-1}s^{-1}$.

In this work, they have used (3-mercaptopropyl) trimethoxy silane (MPS) molecule, in which a thiol tail is bonded to a head grope via a carbon chain. The idea was to fill and hence, passivate the sulfur vacancies, and then heating the functionalized $MoS_2$ at 350°C to dissociate the rest of the molecule and just leave the $MoS_2$ with filled sulfur vacancies behind. The process is schematically illustrated in **Figure** 1-20 a. The FET based on bare and treated $MoS_2$ shows a considerable improvement in the channel conductivity (**Figure** 1-20 c) and electron mobility (**Figure** 1-20 d) of the device.

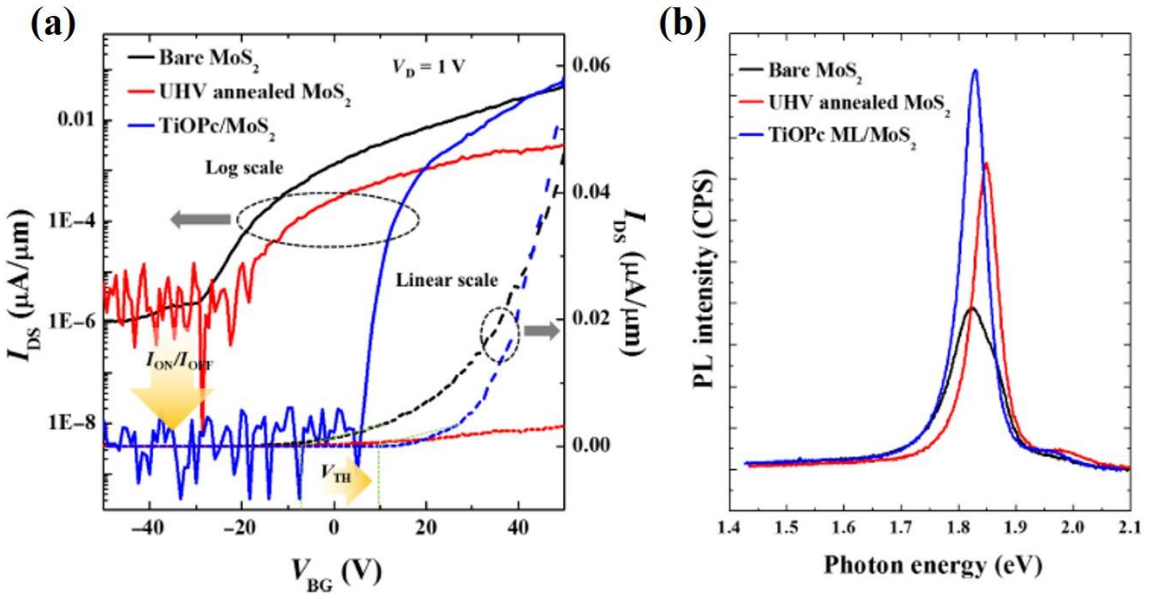


**Figure** 1-19 Electrical and PL characteristics of $MoS_2$ ML, with and without ML TiOPc. (a) Back-gated transfer characteristics of a ML $MoS_2$ FET in log (solid curves) and linear (dashed curves) scales, before and after deposition of ML TiOPc. (b) Room temperature PL of exfoliated ML $MoS_2$ before and after deposition of ML TiOPc. Adapted from [70].

The improvement of performance of FET devices by thiol molecule functionalization has been claimed by other researchers.[60,69,71,84] Moreover, the reaction between organic thiol and $MoS_2$ has been investigated at several works.[84,91,105] As an instance Choi *et al.*[84] deposited dodecanethiol ($CH3(CH_2)_{11}SH$) molecule on defective $MoS_2$ obtained by e-beam irradiation. The molecule consists of thiol tail (as the anchoring group) and hydrocarbon chain with negligible dipole moment (which roles out the doping effect of the organic layer).

They have shown that the thiol molecule fills the sulfur defects and partly recover the surface electronic properties of pristine $MoS_2$, evidenced by shift of Mo3d and S2p core levels to the higher binding energy (see **Figure** 1-17 at **section** 1.3.1).

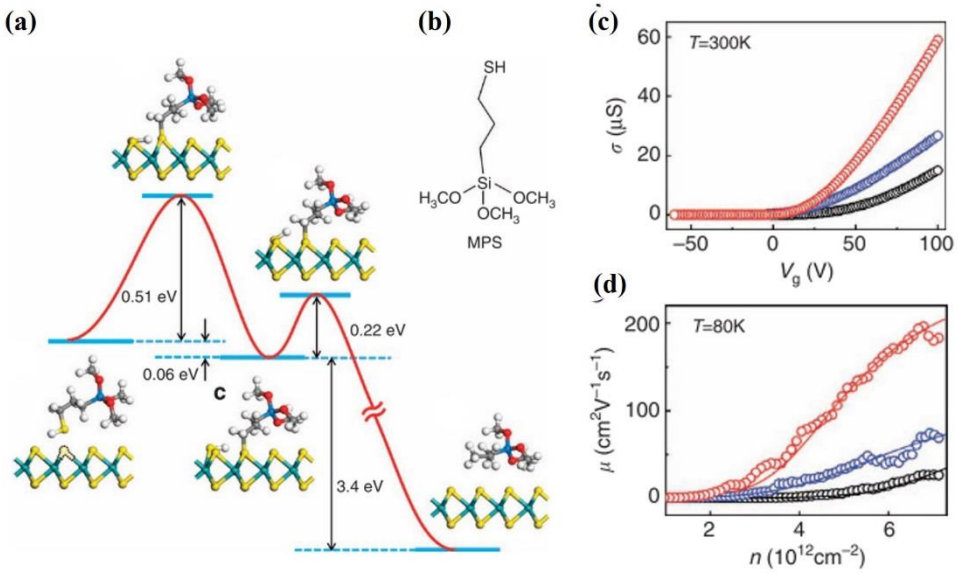


**Figure** 1-20 (a) Kinetics and transient states of the reaction between a single SV and MPS. There are two energy barriers, at 0.51 eV due to the S-H bond breaking, at 0.22 eVs due to S-C bond breaking. (b) chemical structure of MPS. (c) s-Vg characteristics for as-exfoliated (black), TS-treated (blue) and DS-treated (red) monolayer $MoS_2$ at T=300 K. (d) µ-n characteristics for the three devices at T=80 K. Solid lines are the best theoretical fittings. Double side and top side treated samples denoted as TS-treated and DS-Treated, respectively. Adapted from [67].

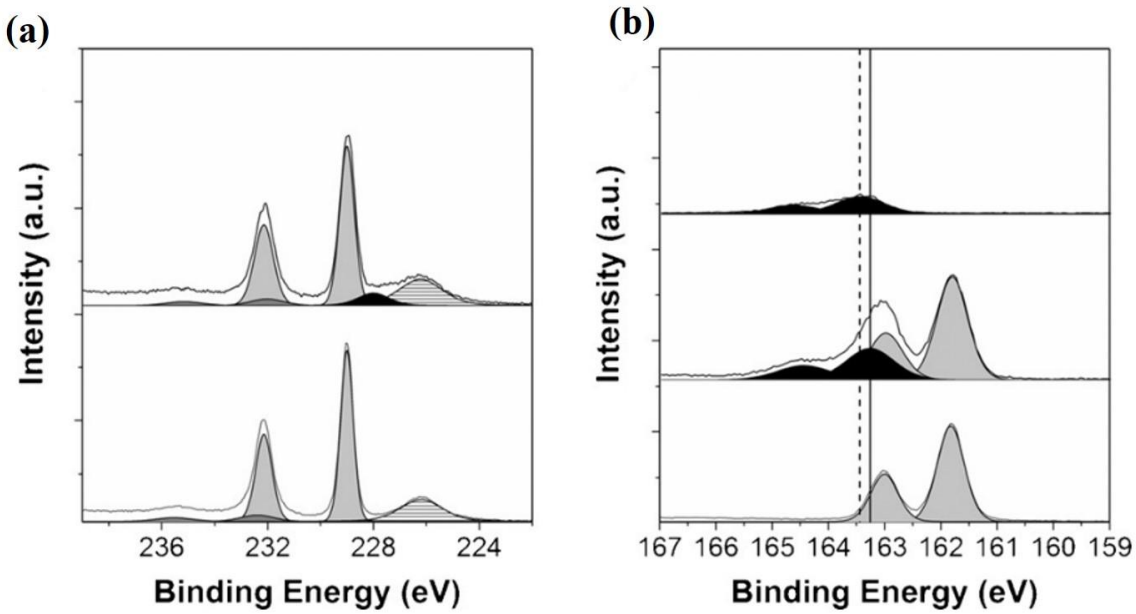


**Figure** 1-21 Fitted XPS spectra. (a) Mo 3d core level spectra of Cys-2H- $MoS_2$ (top), and pristine 2H-$MoS_2$ (bottom). Fit components are attributed to 2H-$MoS_2$, $MoO_3$, $S_{2s}$, and cysteine-like entities in both cases. (b) S2pcore level spectra of cysteine salt (top), Cys-2H-$MoS_2$ (middle), and pristine 2H-$MoS_2$ (bottom). Fit components are attributed to 2H-$MoS_2$ (light gray), and cysteine-like entities (black). Adapted from [91].

However, this is in contrary to the findings of Chen *et al*.[91], since they have claimed that the thiol (cysteine) physiosorbed on $MoS_2$ rather than coordinated as a thiol filling sulfur vacancies in the 2H-$MoS_2$ surface. Unlike the study carried out by Choi *et al*.,[84] they did not observed any shift in the Mo3d and S2p core levels by thiol functionalization (**Figure** 1-21), although they have already confirmed the presence of sulfur vacancies on the $MoS_2$ nanoflakes.

However, in contrary to the latter work, there are more recent studies that confirm the filling of sulfur vacancies via thiol molecule occurring during the functionalization.[60,88,102]

### 1.5 Toward scalable synthesis of TMDCs materials

In the vast area of 2D materials, to carry out the fundamental study on the physical, chemical and electrical properties of 2D-TMDCs, mechanically[106,107] and chemically exfoliated[87,108–111] materials obtained from natural bulk single crystal have been mainly used in a top-down approach. Although this top-down approach led to exfoliated flakes showing very good properties, however, to liberate the significant potential of TMDCs materials in technologically relevant applications, methods for scalable synthesis should be realized. In recent years, considerable efforts have been dedicated to the synthesis of high quality 2D-TMDCs materials using various bottom-up approaches, including vapor phase deposition (VPD), i.e. chemical vapor deposition (CVD)[19,20,76,112,113] and metal-organic vapor deposition (MOCVD),[21,22,114,115] atomic layer deposition (ALD),[116–120] physical vapor deposition (PVD), i.e. pulsed laser deposition (PLD)[121–125] and magnetron sputtering.[126–135] However, despite the many works in developing new approaches and improving the quality of the synthetic TMDC materials, further works are still needed to be carried out. Here we will briefly describe the fundamentals and main achievements of the above-mentioned techniques and optical and electronic properties of the deposited material as well.

#### 1.5.1 Vapor phase deposition (VPD) techniques

Currently, one of the most promising wafer-scale synthesis techniques for atomically thin TMDCs is vapor phase deposition (VPD). In general, the underlying mechanisms in VPD process is principally the chemical reaction or physical transport (often with inert gas as the carrier) of vaporized precursor to deposit TMDCs onto the substrate surface. In terms of the initial precursor state, VPD can be classified into solid-precursor VPD and gas-precursor VPD.[136] The quality of the 2D-TMDCs obtained from VPD process is a function of several

parameters such as growth substrate template, temperature, reacting gasses concentration etc., for which, to obtain a high-quality material, optimization of the all variables is of great importance. Recently, many studies have been undertaken to control the process parameters and the different growth stages in VPD process to obtain high quality TMDCs.,[137,138] Growth stages comprises of three steps, which namely are nucleation, growth and coalescence. (**Figure** 1-22).

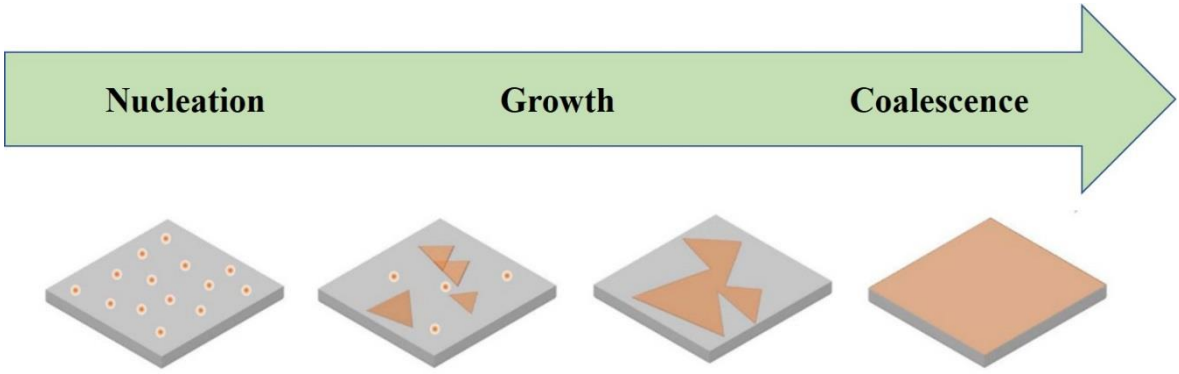


**Figure** 1-22 Three different stages of the CVD process: nucleation, growth and coalescence (formation of continuous film).

As mentioned before, the precursor can be delivered to the main reaction chamber in different ways, through which the VPD techniques can be classified, accordingly:

- Chemical Vapor Deposition (CVD): it is based on the reaction between metal precursors and chalcogen precursors in vapor phase, starting from evaporation of precursor in solid form. In the process set-up, usually three different temperature zones are available to separately evaporate the metal source, i.e. $MoO_3$ and $WO_3$, and chalcogen source, i.e. S and Se, while the substrates maintained at a different temperature (see **Figure** 1-23a).[139,140] As an instance, $MoO_3$ vapor is decomposed to Mo to react with sulfur vapor, leading to formation of $MoS_2$ nuclei, which progressively expand to atomically thin crystal.

- Chalcogenization of metal/metal oxide thin film: this approach is based on the reaction between pre-deposited Transition metal or Transition metal oxide film, i.e. Mo or $MoO_3$, and the chalcogen precursor gas, i.e. sulfur. (see **Figure** 1-23) For example, the Mo or $MoO_3$ thin film with a thickness of a few tens of nanometers is deposited on the substrate by e-beam or thermal evaporation. After pre-annealing, prompt annealing at 1000$^{o}$C in a sulfur gas atmosphere leads to the formation of a crystalline $MoS_2$ thin film.[141,142]

- Metal-organic chemical vapor deposition (MOCVD): metal-organic gas precursors, such as $Mo(CO)_6$, $W(CO)_6$ and $(C_2H_5)_2S$, are pyrolyzed on the target substrate at elevated temperature for the growth of single crystalline or polycrystalline 2D TMDCs. However, the large-scale growth in this process is possible at low temperature, but the required growth time might be over 12 h, which is significantly longer than the other approaches. In **Figure** 1-23 c the schematic illustration of MOCVD process and optical images of 2D $MoS_2$ grown on a $Si/SiO_2$ substrate is given. Since the gas precursor are generally diluted in a mixture of Ar and $H_2$ carrier gases and the partial precursor of each reactant has to be precisely controlled throughout the process for large-scale growth, optimization of the process condition is MOCVD is trickier.[138]

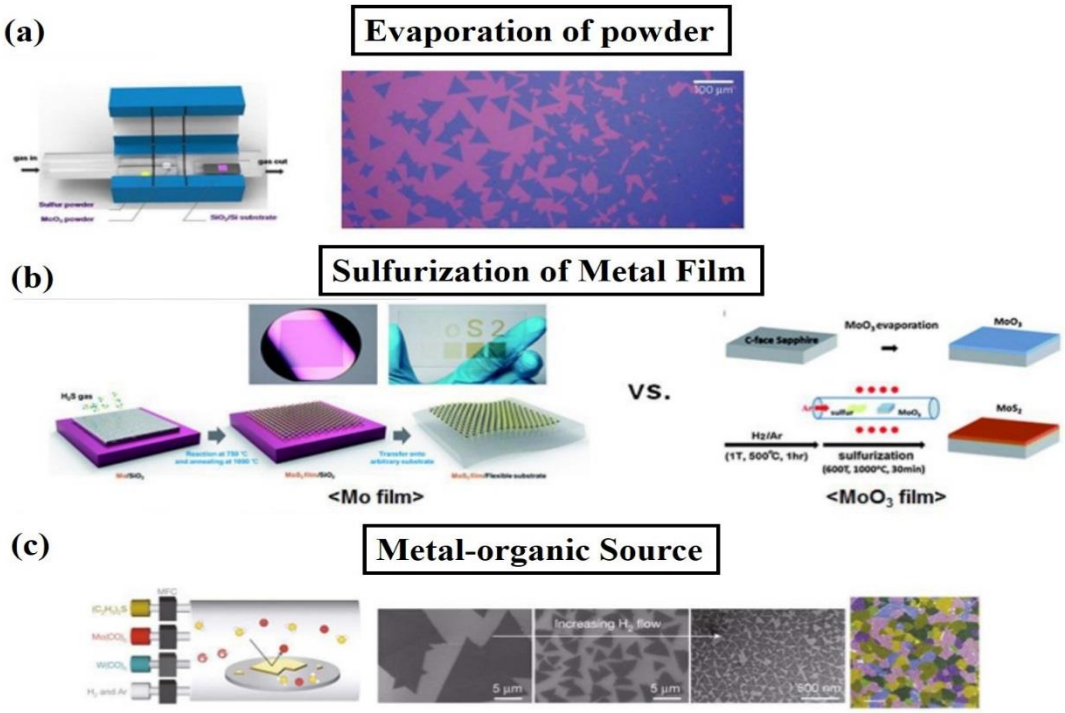


**Figure** 1-23 Three representative VPD methods for growth of TMDCs. (a) Deposition of the evaporated powder precursors, (b) Chalcogenization (sulfurization/selenization) of pre-deposited Mo or $MoO_3$thin film, and (c) MOCVD with pyrolyzed metalorganic gas precursors. Adapted from [138].

As one of the very first work on VPD preparation of $MoS_2$, Zhang *et al.*[143] applied a sulfurization of Mo film approach. The Mo film was pre-deposited on $SiO_2$ substrate. Initially they have taken a 285 nm thick $SiO_2$ on Si substrate and deposited 1-5 nm Mo by e-beam evaporation. In a typical procedure, the Mo samples placed in a ceramic boat were placed in the center of a tube furnace. Another ceramic boat holding pure sulfur was placed in the upstream low-temperature zone (~113 $^oC$) in the quartz tube (**Figure** 1-24 a). The

sulfurization of the Mo film at the center of the furnace was carried out at 750ºC. A Raman spectrum obtained by 532nm excitation shows the two main characteristic vibrational modes typical for $MoS_2$ (**Figure** 1-24 b). Regarding the homogeneity of the deposited film, as can be seen in **Figure** 1-24 c-e, the film contains $MoS_2$ film of different thickness, indicating lack of control on the number of layers of $MoS_2$ deposited on $SiO_2$. On the other hand, the transistor based on the deposited film shows a room temperature mobility in the range of 0.004-0.04 $cm^2V^{-1}s^{-1}$, which is one to two orders of magnitude less than room temperature mobility of the mechanically exfoliated $MoS_2$. This is a clear indication of low crystallinity.

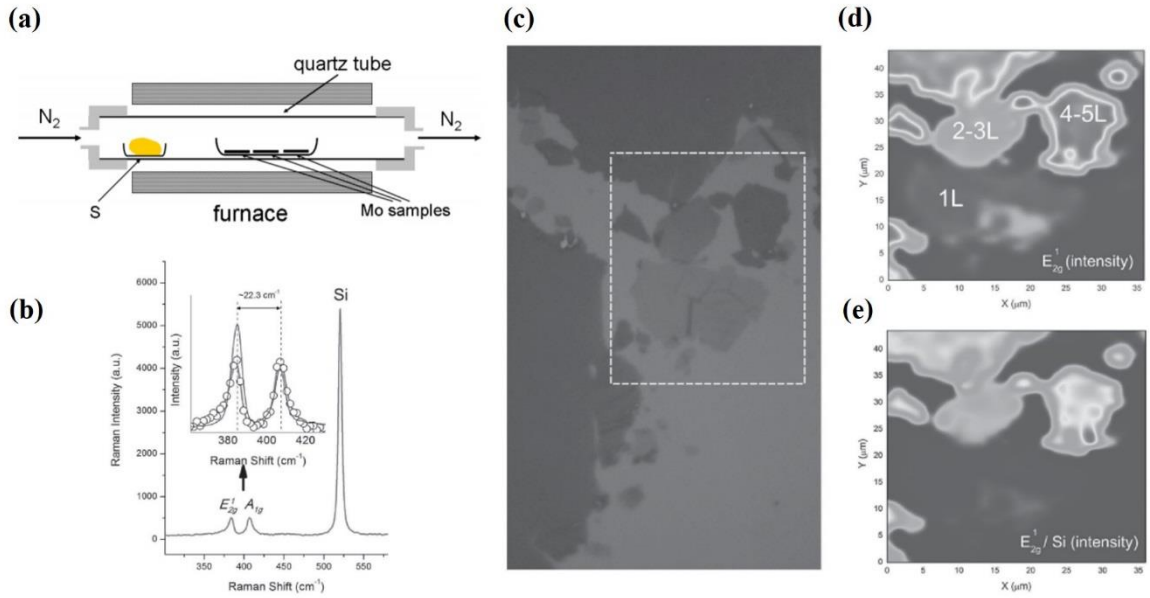


**Figure** 1-24 (a) The CVD system to prepare $MoS_2$ samples, (b) a sample Raman signature of CVD-grown $MoS_2$, (c) A typical landscape of $MoS_2$ atomic layers on $SiO_2$ substrate. The dotted area is mapped in (d) as the intensity of the $E^1_{2g}$ peak, and in (e), as the intensity ratio $E^1_{2g}$/Si, indicating the number of layers. Adapted from [143].

In another work from the same group, Najmaei *et al.*[144] reported the controlled vapor phase synthesis of molybdenum disulfide atomic layers and elucidated a fundamental mechanism for the nucleation, growth and grain boundary formation in its crystalline monolayers. The developed CVD process was based on vapor phase sulfurization of $MoO_3$ nanoribbons dispersed on $SiO_2$/Si substrate (**Figure** 1-25 a) and pure Sulphur. The process was carried out at 850ºC, which is a higher temperature relative to the CVD process in their previous work. The process is schematically illustrated in **Figure** 1-25b. The devices had a channel length and width of 100 µm and 10 µm, respectively. All the devices demonstrated FET characteristic of n-type semiconductor, similar to mechanically exfoliated sample. The mobility showed an average value of 4.3 $cm^2V^{-1}s^{-1}$ with film thickness ranging from single

to multiple layers, so two order of magnitude higher than in previous work. The increase could be attributed to the improved crystallinity of the material with formation of typical triangle $MoS_2$ flakes. Despite the improved crystallinity of the deposited material, the nucleation occurred on the grown flakes before fully coverage of the bare $SiO_2$ surface with monolayer, which hinders the process to reach a controlled thickness growth over a large area. As given in **Figure** 1-25 d, the Raman signatures of random spots across the continuous film show different distances between the two characteristic peaks of $MoS_2$, which is a clear indication of different thickness.

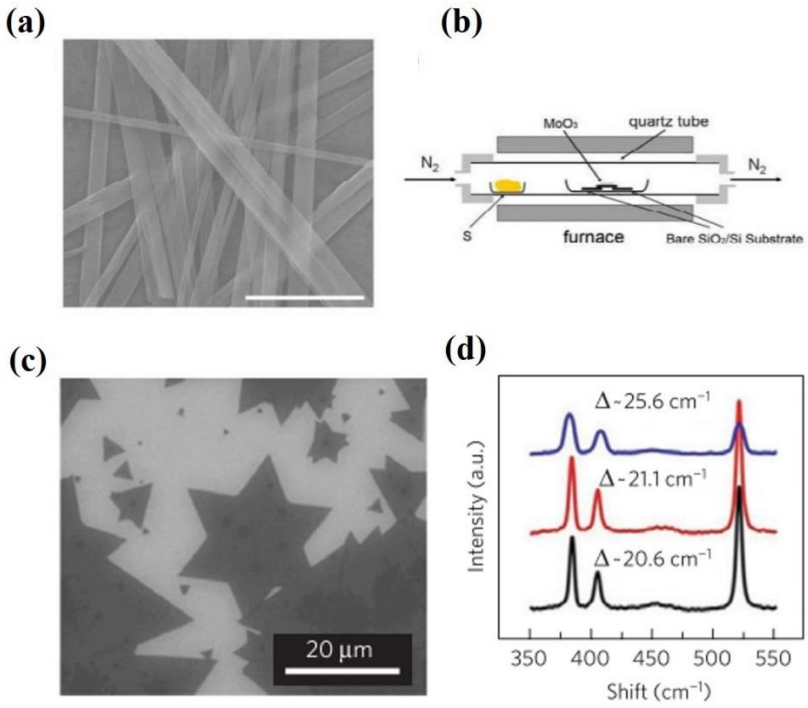


**Figure** 1-25 (a) $MoO_3$ nanoribbons prepared by hydrothermal method, (b) The CVD system to prepare $MoS_2$ samples, (c) $MoS_2$ triangles grown randomly on $SiO_2$ substrate, (d) Raman spectra of 3 random spots on $MoS_2$ continuous film. Adapted from [144].

Van der Zande *et al.*,[140] had a deeper insight into the grain boundaries formed due to the flakes of $MoS_2$ growth and overlapping. Similar to previous works, growth substrates were Si with 285 nm of $SiO_2$. Using a 2-inch CVD furnace and placed face-down above a crucible containing $MoO_3$ with another crucible containing Sulphur located upstream, the growth was performed at atmospheric pressure and 700$^o$C hot zone temperature. The process could yield a highly crystalline islands of monolayer $MoS_2$ up to 120 µm (**Figure** 1-26 b) in size with optical properties comparable or superior to exfoliated samples. They have differentiated two different grain boundaries, so called faceted tilt and mirror twin boundaries, causing strong enhancements and quenching of photoluminescence, respectively. On the other hand,

mirror twin boundaries slightly increase the measured in-plane electrical conductivity, whereas tilt boundaries slightly decrease the conductivity.

In devices from different growth, room-temperature field-effect mobilities ranged from 1-8 $cm^2V^{-1}s^{-1}$, and typical on/off ratios ranged between $10^5$-$10^7$. The values are attributed to the multiple devices fabricated within single crystal domains.

To obtain an epitaxial growth and hence taking a step forward to grow a uniform $MoS_2$ film, in a more recent study, Dumcenco *et al.*,[19] utilized a treated sapphire substrate, which facilitated the epitaxial growth of $MoS_2$, and therefore putting a further emphasis on the influence of growth substrate in obtaining a high quality 2D-$MoS_2$. The growth of $MoS_2$ on sapphire substrate has already been reported,[145] but for the first time they could achieve control over lattice orientation with centimeter-scale uniformity during the growth of monolayer $MoS_2$. Key point is the preparation of atomically smooth sapphire terraces by annealing it in air for 1 hour at a temperature of 1000 $^oC$ just prior to the growth process. The CVD growth process was based on gas-phase reaction between $MoO_3$ and sulfur evaporated from solid sources, using ultra-high-purity argon as the carrier gas at 700 $^oC$ tube furnace hot zone temperature.

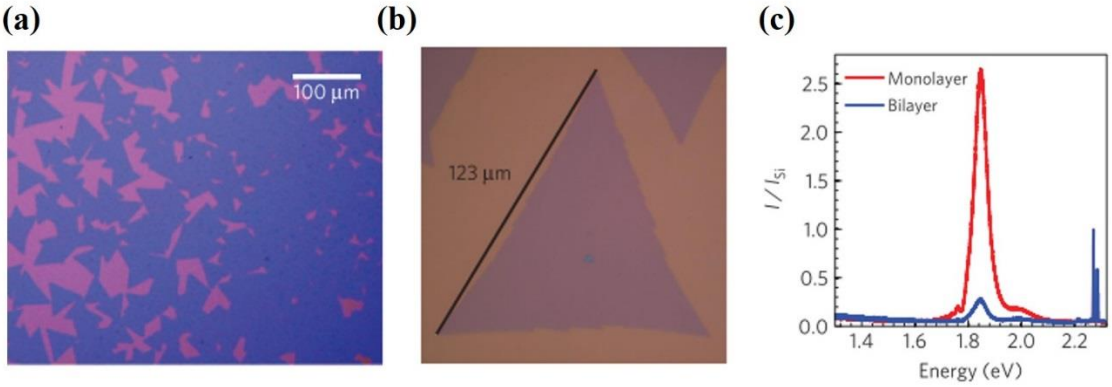


**Figure** 1-26 Optical image of (a) large grain $MoS_2$ on $SiO_2$, (b) monolayer $MoS_2$ triangle. The triangle is 123 µm from tip to tip. (c) Photoluminescence spectra from monolayer (red) and bilayer (blue) $MoS_2$. Peak height is normalized to the silicon Raman peak. Adapted from [140].

The influence of sapphire annealing can be seen in **Figure** 1-27 a and b, as the $MoS_2$ grains on unannealed sapphire are randomly oriented. The Raman spectra of the CVD-grown material compared to monolayer $MoS_2$ exfoliated onto sapphire is represented in **Figure** 1-27 c. The frequency difference confirms that the material is monolayer $MoS_2$. Moreover, since the ratio between the intensity of $A_{1g}$ and $E_{2g}{}^1$ vibrational modes is an indication of doping level, it can be seen that the CVD material is less doped than the exfoliated

counterpart and also pertains less disorders, since the FWHM of the $A_1$ peak of CVD material is less than that of exfoliated one. **Figure** 1-27 d shows a PL spectrum.

An intense exitonic peak at 659 nm (1.88 eV) can clearly be resolved. Typical widths are ~26 nm (~72 meV) and are smaller than in exfoliated $MoS_2$ samples with ~ 40 nm (~111 eV), indicating that the CVD-$MoS_2$ shows higher optical qualities than exfoliated material. UV-visible absorption spectrum shows the well-known A and B exitonic absorption bands at 695 nm (1.78 eV) and 611 nm (2.02 eV), which demonstrates the high optical quality of the deposited $MoS_2$. Although using sapphire necessitate the transfer of the grown material to realize electronic devices, which itself may result in difficulties and problems, the quality of the grown material in this work is among the best material reported in the literature so far.

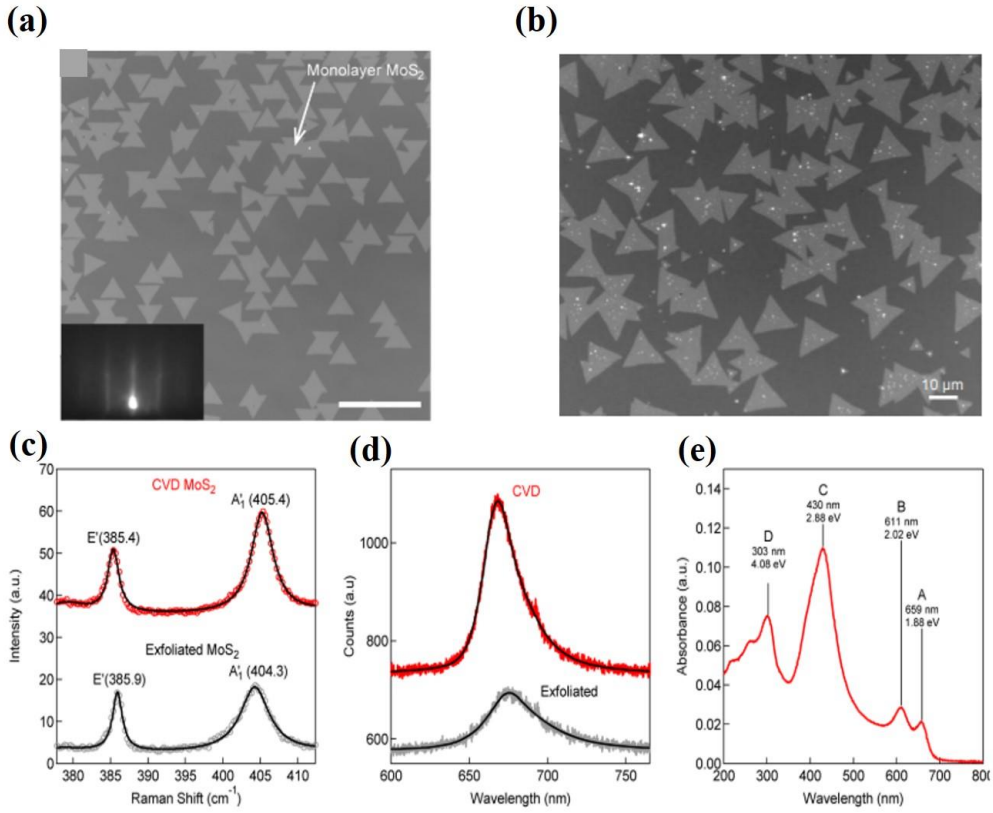


**Figure** 1-27 (a) Optical microscopy image of monolayer $MoS_2$ grains. Scale bar length is 50μm. Inset: RHEED pattern, showing a film with long-range structural order. (b) Optical image of a triangular $MoS_2$ single crystals grown on sapphire without annealing, (c) Raman spectra of monolayer $MoS_2$ (d) Photoluminescence spectra of monolayer $MoS_2$ (c) UV-vis optical absorbance spectra acquired from large-area monolayer $MoS_2$ showing the A and B absorption peaks due to band-edge excitons as well as C and D peaks associated with van Hove singularities of $MoS_2$. Adapted from [19].

The realm of vapor phase deposition of 2D-TMDC materials is quite vast. Other approaches in terms of precursors types or metal film preparation techniques (in metal film sulfurization approach) have been under investigation. For example, using metal-organic chemical

compounds as the precursors instead of vaporizing the solid precursors,[21,114] or using different techniques like magnetron sputtering[146] or ALD[147] to prepare Transition metal film before sulfurization. More detailed review on the influence of process parameters, precursors, substrate etc. on CVD growth of 2D materials has been provided by Zhang *et al*.[148], Bosi[149] and Kim *et al*.[150].

However, VPD techniques have some disadvantages, such as harsh growth environment, high reaction temperature, long growth time and use of toxic precursor (in some cases) which makes the process more complicated. As a result, the pursue for alternative approaches has always been an option.

### 1.5.2 Atomic layer deposition (ALD)

Atomic layer deposition (ALD) process, basically comprise of a sequential use of a gas phase chemical process. It is principally a subclass of chemical vapor deposition. In this process, the precursors react with the surface of a material one at a time in a sequential and self-limiting manner. Whilst ALD process, the surface is being exposed to alternate precursors which leads to gradual synthesis of the film. Unlike to the CVD process, precursors are never present in the reactor at the same time, but they are introduced as a series of sequential and non-overlapping pulses. In each of these pulses the precursor molecules react with the surface in self-limiting way, so that the reaction terminates once all the reactive sites on the surface is consumed.[151,152] Due to self-limiting nature of the reactions in ALD reactor, not only the thickness of the films can be controlled at an atomic scale, but also the uniformity can be kept on a large-area substrate even with complex structures.[153]

Moreover, since the ALD process is insensitive to excessive precursors, this approach holds promises for high reproducibility. ALD does not require a high growth temperature, which is an advantageous over CVD process where high growth temperatures are typical, showing high potential for 2D material growth.

Successful synthesis of $MoS_2$ and $WS_2$ has recently been demonstrated. Kheng *et al*.,[154] in 2014, could grow a mono-to multilayer $MoS_2$ film by ALD process at 300$^{o}$C on a sapphire wafer. They used $MoCl_5$ and $H_2S$ as the precursors to provide Mo and S atoms, respectively. The synthesis was followed by a post-annealing step at 800$^{o}$C in a tube furnace with sulfur saturated atmosphere.

The annealed $MoS_2$ at 800°C shows relatively good PL emission and as evidenced by Raman spectra, annealing increases the crystallinity of the deposited film. (see **Figure** 1-28 a and b) The deposited film shows the characteristic layered nature of $MoS_2$ film as shown in **Figure** 1-28 d in TEM image. However to obtain a high quality TMDCs materials, the process parameters should be finely optimized and more appropriate precursors investigated.[155]

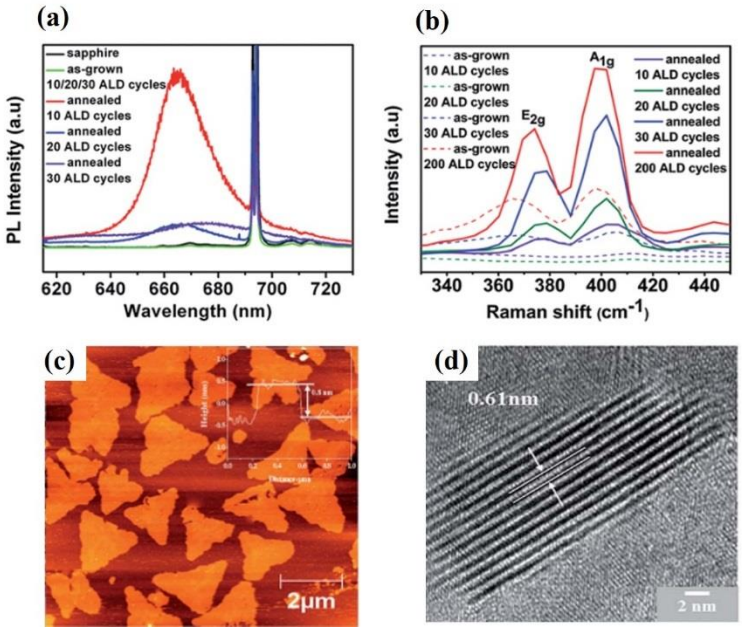


**Figure** 1-28 (a) photoluminescence spectra and (b) Raman spectra ALD-deposited, as-grown or annealed $MoS_2$ films, (c) AFM images of monolayer 800°C-annealed ALD $MoS_2$ film. The inset shows the height profile of the triangular flakes. (d) Lattice spacing from a cross-sectional TEM view. Adapted from [154].

Mattinen *et al.*[120] introduced a new Mo precursor $Mo(thd)_3$ (thd= 2,2,6,6-tetramethylheptane-3,5-dionato), which facilitates the low temperature growth of $MoS_2$ by ALD using $H_2S$ as the sulfur precursor. They have shown that the deposited film pertains a high roughness, RMS~3nm for the film with 1nm average thickness but poor crystallinity for low cycle deposited films, as shown in **Figure** 1-29 a, although Raman spectra shows two typical main characteristic peaks of $MoS_2$ (**Figure** 1-29 b). They have also revealed the influence of growth temperature on the crystallinity of the deposited material. As given in **Figure** 1-29c and d, the higher crystallinity was obtained for the 400 °C growth temperature. The functionality of the material has not been evaluated in any practical application.

To facilitate the chemical reactions in the ALD reactor and hence further improve the quality of the deposited film, plasma enhanced ALD (PEALD) was used in some other works. For example, Delabie *et al.*,[116] applied a low temperature PEALD process to investigate the $WS_2$

deposition by $WF_6$ (precursor as W provider), $H_2$ plasma and $H_2S$ (precursor as S provider) reactions at 300 $^oC$ growth temperature and $Al_2O_3$ as the substrate.

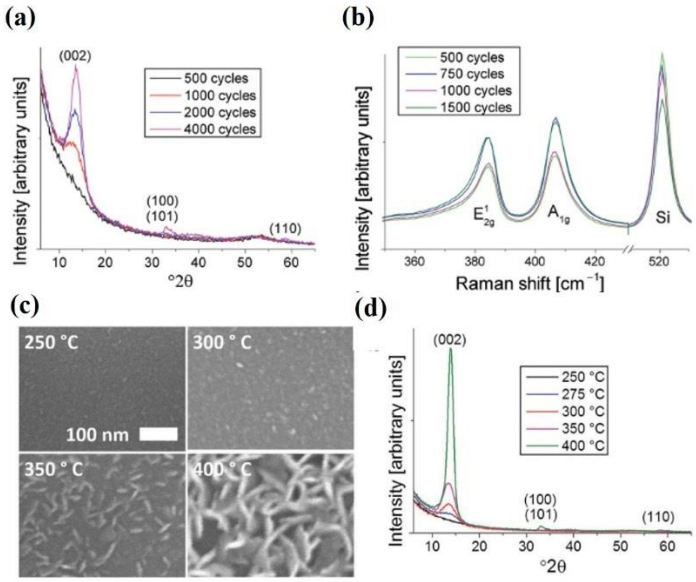


**Figure** 1-29 Crystallinity of $MoS_2$ films deposited at 300$^o$C. (a) X-ray diffractograms of films grown with 500–4000 cycles, (b) Raman spectra of films grown with 500–1500 cycles. Effect of deposition temperature on film crystallinity, (a) SEM images and (b) X-ray diffractograms of $MoS_2$ films grown at different temperatures on silicon using 2000 cycles. Adapted from [120].

As given in **Figure** 1-30a and b, the $WF_6$ and $H_2S$ reactions show the conventional ALD saturation behavior, indicating that the two precursors reaction is self-limiting. However, the high plasma power (*e.g.* 300 W), would lead to less control on sulfur content as can be concluded from the divers stoichiometries given in **Figure** 1-30d. Both $H_2$ plasma power and exposure time found to be strongly effective on the composition of deposited film. For the samples deposited at higher plasma power, the samples shown both $WS_2$ and $WO_3$ peaks in XPS core levels. Oxidation occurs due to presence of the metallic W in the film, which become oxidized during exposure to air. The Raman spectra also confirms the low crystallinity of the deposited film as the longitudinal acoustic phonon at M point LA(M) appeared quite dominant at around 224 $cm^{-1}$. The LA(M) peak is a clear indication of the presence of defects and disorders in $MoS_2$.[156] Despite the low crystallinity, the deposited $MoS_2$ holds its layered nature as shown **Figure** 1-30 g and h.

A more recent work by the same group, shows further improvement of the quality of the deposited 2D-$WS_2$. Groven *et al.*,[157] demonstrated that crystal grain size increases from 20

to 200 nm by lowering the nucleation density. They have attributed this to lower precursor adsorption rate on starting surface using an inherently less reactive starting surface, by decreasing the $H_2$ plasma reactivity and by enhancing the mobility of the adsorbed species at higher deposition temperature.

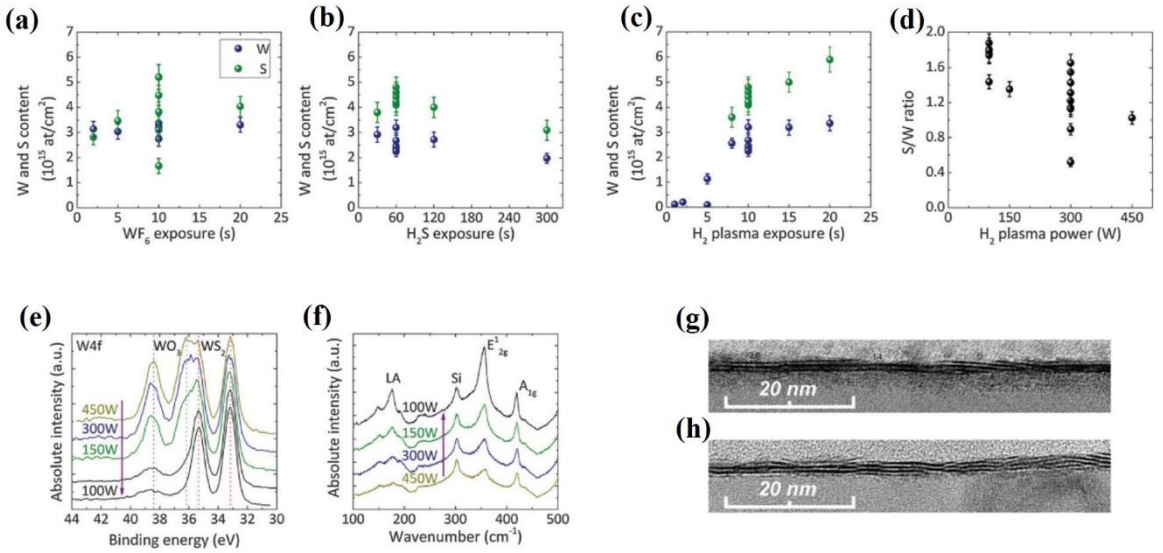


**Figure** 1-30 RBS of W and S-content as a function of precursor exposure time (a) and (b), and H2 plasma exposure time (c) and $H_2$ plasma power (d). (e) XPS W4f and (f) Raman spectrum as a function of the plasma power. (g) 2–3 monolayers of $WS_2$ deposited at 300ºC on amorphous $Al_2O_3$, (h) 3 monolayers of $WS_2$ deposited at 300 ºC on crystalline $Al_2O_3$. Adapted from [116].

They have also used Silicon Oxide ($SiO_2$) as the growth template, which shows less reactivity than Aluminum Oxide ($Al_2O_3$).

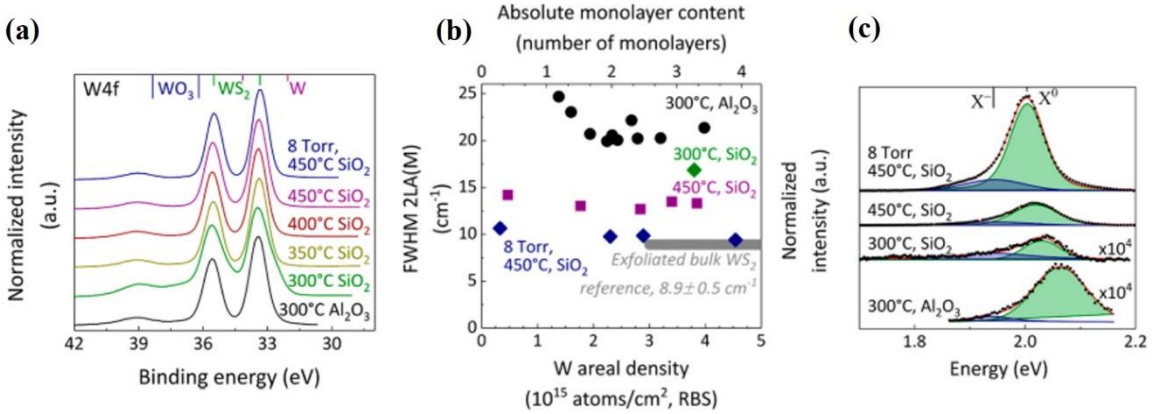


**Figure** 1-31 (a) Normalized W 4f XPS spectra (angle-integrated) for 3−4 ML of $WS_2$ as a function of growth temperature. (b) 2LA(M) FWHM as a function of the W areal density (obtained from RBS (c) PL response of $WS_2$ PEALD. The PL spectrum is deconvoluted into two contributions, including the charge-neutral exciton ($X^0$) and trion (X−) PL peak. Adapted from [157].

As given in **Figure** 1-31a, the XPS W4f core level shows less oxidation in comparison to the $WS_2$ film reported in their former work (see **Figure** 1-30 e), indicating the presence of less metallic W to be oxidized after exposure to air for XPS measurement. Furthermore, the FWHM of the 2LA(M) peak in Raman spectra decreases as the growth temperature increases. Likewise, the material grown at higher temperature shows higher PL intensity, an indication of higher quality of the deposited material. The transistor based on the deposited sample with the optimal growth condition shows a response with ratio of maximal to minimal drain current ($I_{D,max}/I_{D,min}$) of $10^5$ for 224 nm long and 1µm wide channels.

ALD despite its intriguing capabilities, is still in its premature stage for yielding high quality TMDCs materials applicable in (opto)electronic devices and the work in this field is continuing.

### 1.5.3 Pulsed laser deposition (PLD)

Pulsed laser deposition (PLD) technique has first become popular after successful deposition of superconducting Yttrium Barium Copper Oxide ($YBa_2Cu_3O_7$) film in an efficient and epitaxial way.[158] Afterward, PLD has been mostly used for deposition of complex oxide thin films, heterostructures and well controlled interfaces. A shown in **Figure** 1-32, the PLD set-up is mainly consists of an ultrahigh vacuum chamber (UHV) and high energy pulsed laser.

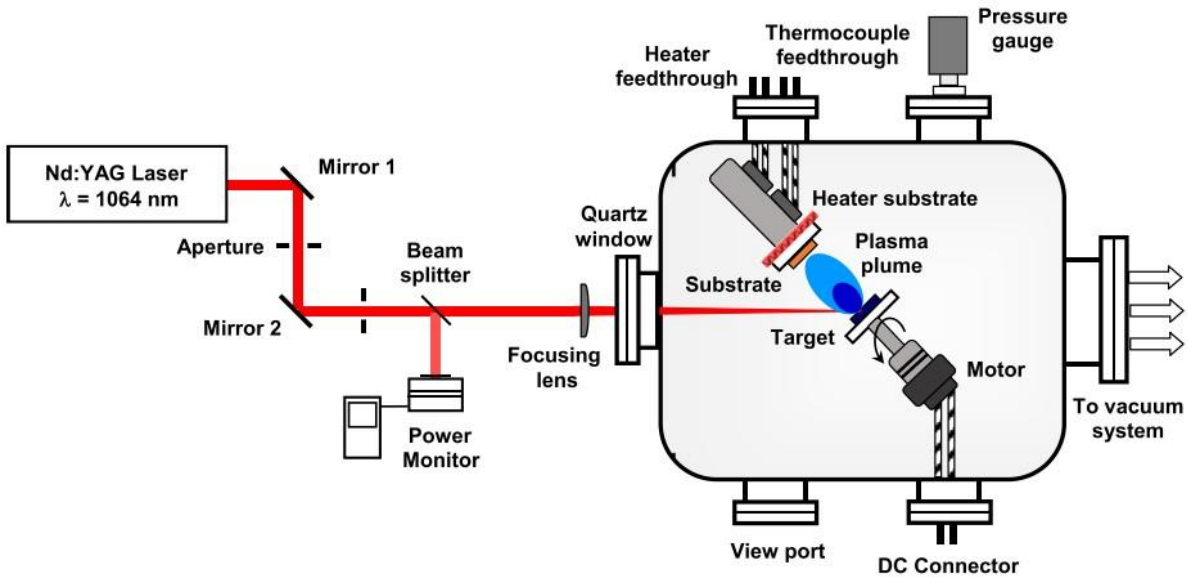


**Figure** 1-32 Schematic of a PLD system. Adapted from [160].

In contrary to VPD techniques, PLD utilizes pure physical method to prepare large scale thin films mainly under higher vacuum and lower growth temperature. Compared to VPD, the advantageous of PLD include high rate of deposition, good control of thickness and morphology, and low growth temperature.[159]

The underlying mechanism in PLD deposition process is principally a series of complex physical reactions in an ablation event. When the focused laser beam strikes the surface for a short time, as a result of the laser light and target material interaction ablation occurs, an energetic plasma plume carrying the ions and atoms of target material is formed, and then deposited on a pre-heated substrate placed in front of the target. The quality of the deposited film in PLD process is also highly dependent on the process parameters, such as substrate temperature and pulsed laser source (wavelength, fluence, frequency and pulse duration). Moreover, it is necessary a good optical absorption of the target material in order to achieve an efficient ablation process. Beside using PLD for the deposition of complex oxide thin film, this technique has recently been considered for growing 2D materials including graphene,[160–162] Molybdenum Disulfide ($MoS_2$),[23–25,159,163–165] Molybdenum Sulfoselenide ($MoS_2Se_2$)[166] have been successfully grown by use of PLD techniques.

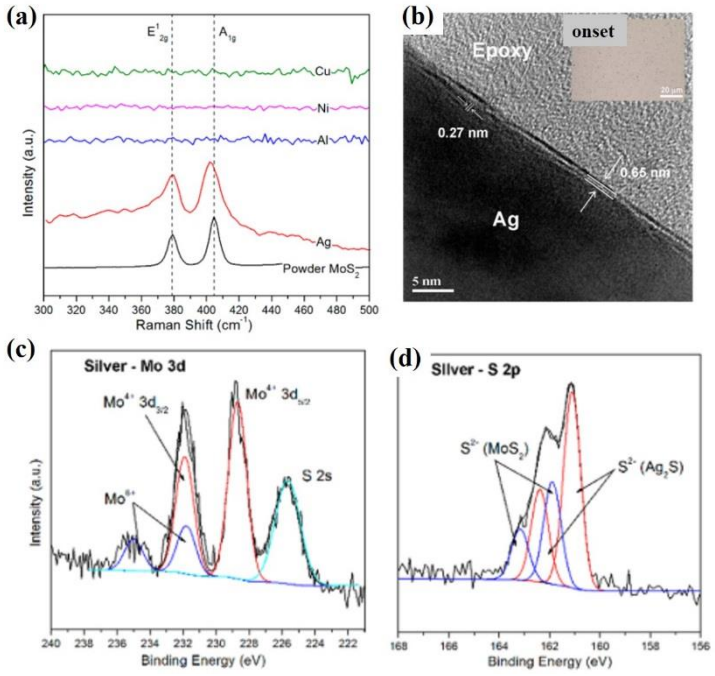


**Figure** 1-33 (a) Raman spectra of as-grown samples fabricated on different metal substrates. (b) Cross-sectional TEM image of Ag sample fabricated at 50 mJ laser energy and 10 s deposition time Onset is the optical image showing the uniform coverage of the film. (c) and (d) XPS spectra showing Mo 3d, S 2s, and S 2p core level peak regions of the sample deposited on Ag substrate. Adapted from [164].

Among TMDCs, PLD has been first used to deposit $MoS_2$ film for lubrication of aerospace components. In 1994, McDevitt *et al.*,[165] studied the influence of thermal annealing on disorders of PLD deposited $MoS_2$ film by Raman. They could capture the sign of disorder reductions induced by thermal annealing on the Raman characteristic. Loh *et al.*[164] studied the growth mechanisms of $MoS_2$ few-layers on Ag, Al, Ni and Cu metal substrate. They have shown that the solubility of the transition metal (Molybdenum) and chalcogenide (sulfur) atoms in the substrate is a dominating factor on the crystallinity of the deposited film. They have claimed that, since the ablated materials are highly energetic, they could dissolve into the metal substrate rather than just being deposited on it. Among the four metal substrate, only the Ag could yield a good crystallinity (see **Figure** 1-33 a and b). In the case of Ag substrate, Mo is insoluble in solid Ag at any temperature, while S reacts with Ag to form Silver Sulfide, $Ag_2S$, during early growth stages at the surface regions of the substrate, acting as a growth template. Mo atoms that segregate out of Silver bind to the sulfur species in $Ag_2S$, in addition to unreacted S atoms. The energy supplied by the pulsed laser and by heating imparts mobility to the Mo and S atoms that allow them to rearrange into an orderly configuration during the subsequent cooling process. However, as evidenced by XPS measurement (**Figure** 1-33 c and d), the as deposited $MoS_2$ contains byproducts of Mo and S species, appeared as Molybdenum Oxide ($Mo^{6+}$) and Silver Sulfide ($AgS_2$), respectively, which reduces the quality of the deposited material.

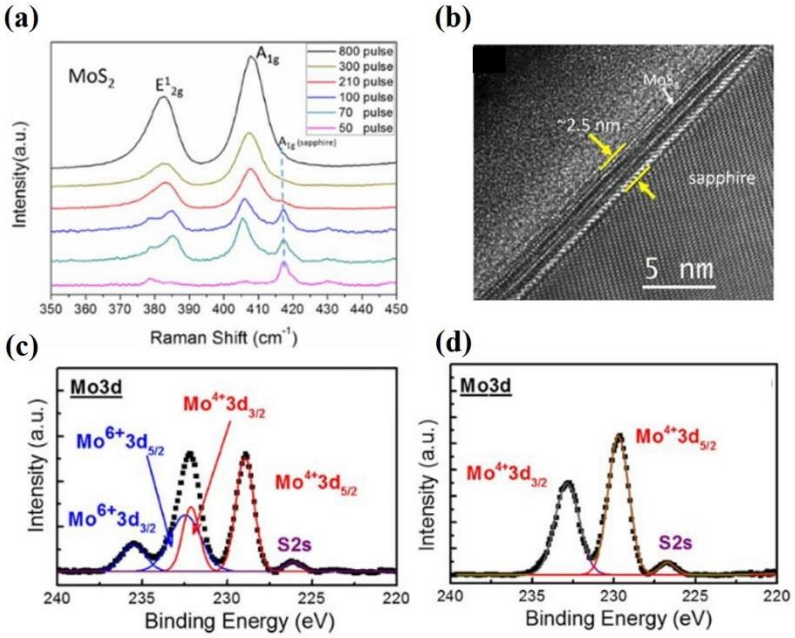


**Figure** 1-34 (a) Raman spectra of $MoS_2$ deposited on sapphire with various pulse numbers in PLD. (b) Cross-sectional view of high resolution TEM images 210 pulses. XPS Mo3d core level of (c) as deposited and (d) post-treated $MoS_2$. Adapted from [25].

The formation of byproducts during PLD deposition of $MoS_2$ few-layers on Ag substrate has reported in other work.[167] Ho *et al.*[25] studied the influence of pulse number on the crystallinity of the PLD-grown $MoS_2$ on sapphire template at 800°C growth temperature. They have shown that the film higher laser pulse number yield a better quality as evidenced by Raman spectra and the cross-section TEM image (**Figure** 1-34a and b). Moreover, they have shown that, a post sulfurization process at 650°C effectively reduces the molybdenum oxide content in the as-grown film (**Figure** 1-34 c and d).

In a more recent work, Xie *et al.*,[123] systematically studied the influence of post-sulfurization at different temperature. They have shown that the content of Mo oxide specie reduces by increasing the post sulfurization temperature from 400 to 600 °C, evidenced by XPS Mo3d core level (**Figure** 1-35a). Moreover, they have captured an increase in the intensity of $E_{2g}^1$ mode after sulfurization at 500°C, which is an indication of increased crystallinity.

As illustrated in the TEM cross section images of the 2D-$MoS_2$ grown by PLD, it can be seen that the technique preserves the layered nature of the material in a large scale with an excellent control on the thickness, which is a clear advantage over vapor phase deposition techniques, i.e. CVD and MOCVD. But the crystallinity of the as-grown layers is still not high enough and also the post process cannot recover the crystallinity desirably. However, further improvements are foreseen by tuning the process parameters and engineering the growth templates.

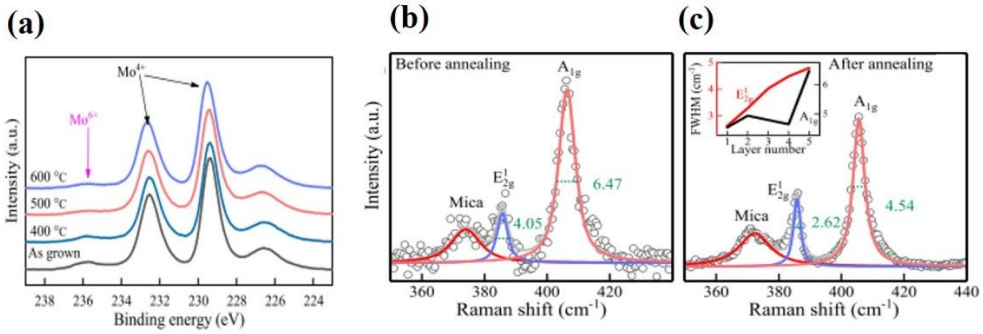


**Figure** 1-35 (a) XPS spectra of Mo 3d core level peaks for $MoS_2$ films as-grown and annealed at different temperature. (b) and (c) Raman spectra of the as-grown sample and the annealed sample at 500 °C. Adapted from [123].

### 1.5.4 Magnetron Sputtering

Magnetron sputtering has developed rapidly over the last decade, being the process of choice for the deposition of a wide range of industrially important coatings. In the basic sputtering process as shown in **Figure** 1-36, a target (or cathode) plate is bombarded by energetic ions

generated in a glow discharge plasma, situated in front of the target. The bombardment process causes the removal of the target atoms (sputtering) which may then condense on a substrate as a thin film.[168] Secondary electrons are also emitted from the target surface as a result of the ion bombardment, and these electrons play an important role in maintaining the plasma.

In this technique a magnetic field configured parallel to the target surface can constrain secondary electron motion to the vicinity of the target. The magnets are positioned in such a way that one pole is located at the central axis of the target and the second pole is formed by a ring of magnets around the outer edge of the target (see **Figure** 1-36). Trapping the electrons in this way substantially increases the ionization efficiency, resulting in a dense plasma in the target region.[169]

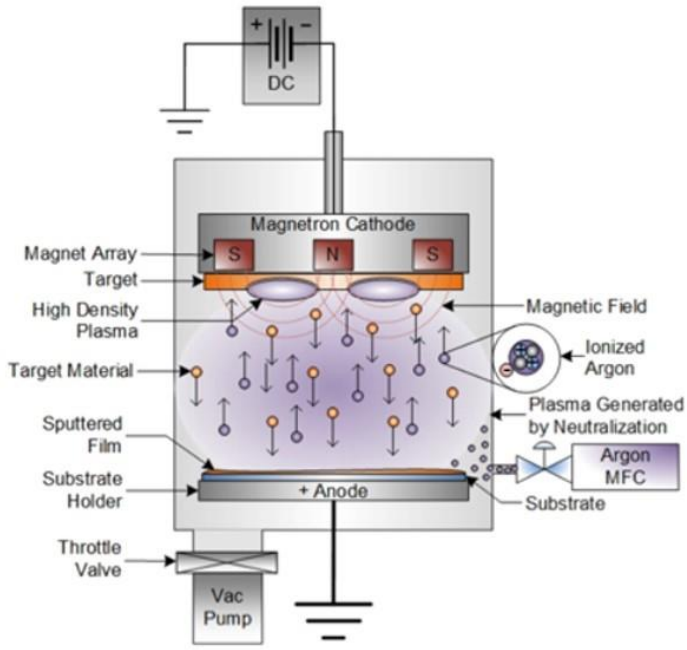


**Figure** 1-36 Diagram of the DC Magnetron Sputtering Process. Adapted from www.semicore.com

Magnetron sputtering has recently been used for synthesis of 2D-TMDCs. Ling *et al.*,[129] has demonstrated a large scale 2D-$MoS_2$ by Magnetron sputtering. They have unraveled the photoresponsivity of the deposited material by realizing a photodetector integrated with five monolayers of $MoS_2$. The device shown a high responsivity of 1.8 A/W at 850 nm excitation wavelength, and an external quantum efficiency exceeding 260 %. The deposition process involves the growth of atomically thin $MoS_2$ film by DC magnetron sputtering of Molybdenum target in a vaporized sulfur ambient, using a substrate temperature of 700$^{o}$C. The sulfur and Argon partial pressures were $4.0\times10^{-7}$ and $6.0\times10^{-4}$ mbar, respectively.

Despite the considerable photoresponsivity of the material, the quality of the deposited $MoS_2$ crystal seems to be low as the FWHM of the XPS core levels shown in **Figure** 1-37b, which is in the range of 1.2 - 3.5 eV.

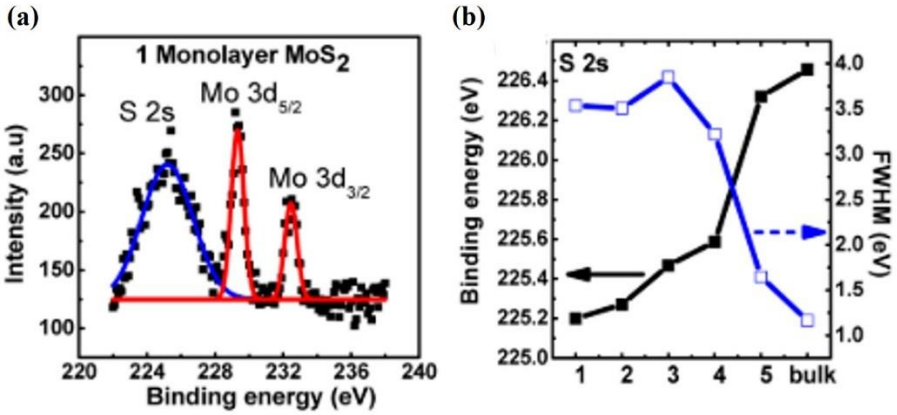


**Figure** 1-37 (a) Deconvolution of the XPS spectrum for the 1 monolayer $MoS_2$ film, (b) S 2s peak binding energy position increases, and FWHM decreases as the number of $MoS_2$ layers increases. Adapted from [129].

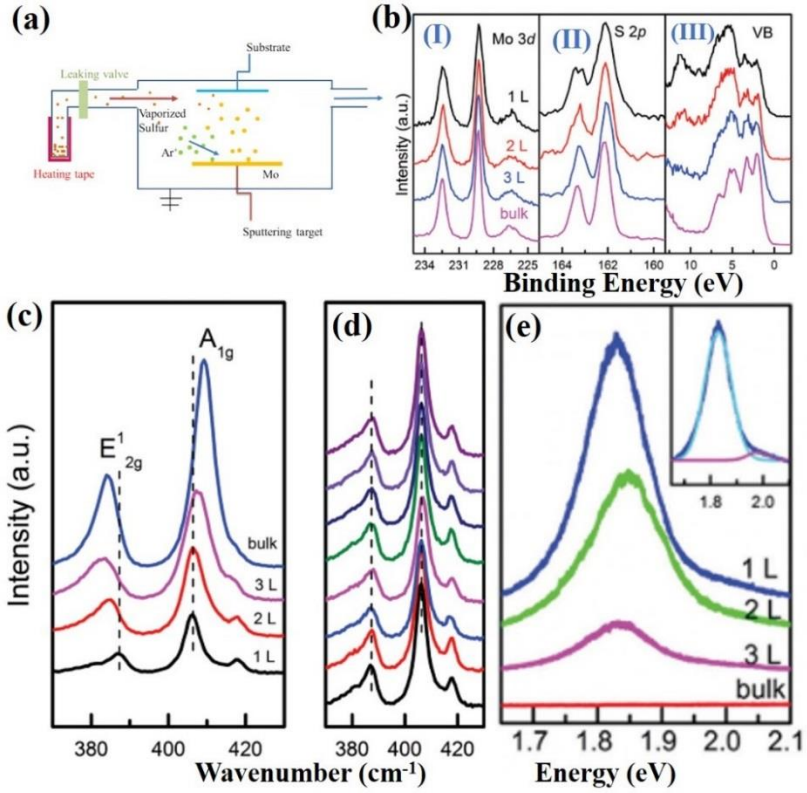


**Figure** 1-38 (a) Schematic drawing of the growth setup. (b) Normalized XPS spectra of as-grown $MoS_2$ on sapphire. (I) Mo 3d, (II) S 2p spectra and (III) valence band (VB) as a function of the film thickness. Raman spectra of the as-grown $MoS_2$ on sapphire: (c) Thickness-dependent variation of the Raman spectra. (d) Raman spectra collected from eight random spots of the $MoS_2$ monolayer film. All of the measured frequency separation ($\Delta k$) is 19.3 $cm^{-1}$. (e) Thickness-dependent photoluminescence spectra of $MoS_2$ films on $SiO_2$. Adapted from [132].

Moreover, in the Mo3d-S2s XPS core levels given in **Figure** 1-37 a, the S2s peak located at the lower binding energy relative to Mo3d found to be too dominant, indicating the presence of a great amount of sulfur content in the system leading to a non-stoichiometric $MoS_2$.

In another work, Tao *et al.*[132] demonstrated a p-type $MoS_2$ grown at high temperature (700$^o$C) using Mo metal target sputtered in vaporized sulfur ambient. Sulfur was vaporized using heating tape wrapping around the sulfur container before leaking into the chamber (**Figure** 1-38a). The Raman and photoluminescence spectroscopy indicate comparable optical qualities of the as-grown $MoS_2$ with other methods (see **Figure** 1-38c-e). The XPS Mo3d-S2s and S2p core levels of as-grown $MoS_2$ on sapphire also shows well-resolved spectrum in comparison to the previous work carried out by Ling *et al.*[129] (see **Figure** 1-37a), indicating a better crystallinity of the deposited material. They have also demonstrated a transistor based on the magnetron sputtered $MoS_2$, with p-type performance, on/off ratio of $10^3$ and hole mobility of up to 12.2 $cm^2V^{-1}s^{-1}$. Such p-type behavior of the transistor was expected as the VBM of the film is too close to the Fermi level as given in **Figure** 1-38b-III.

However, in comparison to the exfoliated $MoS_2$ with mobility at around $200^2V^{-1}s^{-1}$,[7] the magnetron sputtered $MoS_2$, shows far lower mobility and needed to be improved.

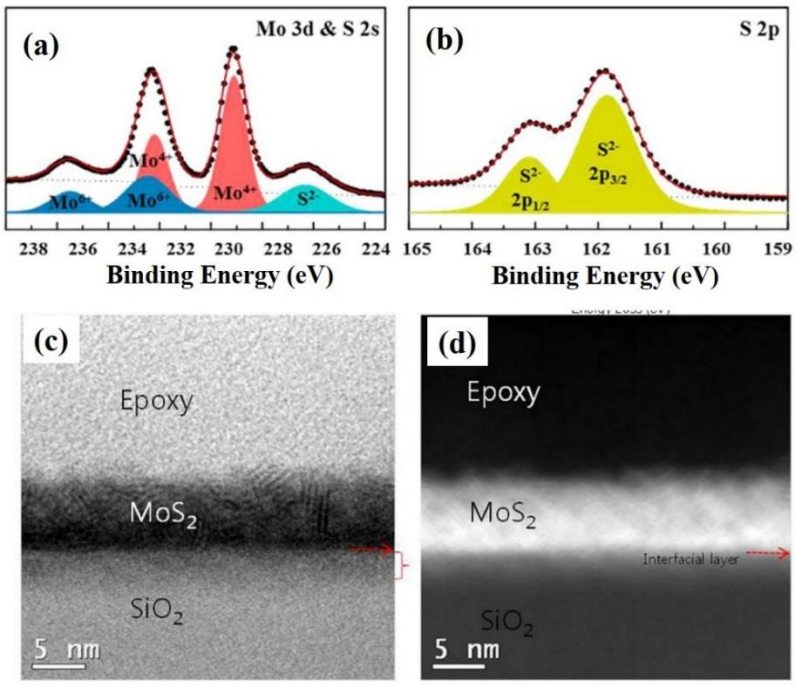


**Figure** 1-39 (a), (b) XPS spectra of $MoS_2$ films annealed at 700 °C. Mo and S atoms binding energy spectra for 1 min sputter time. (c) HRTEM and (d) STEM-HAADF image of few layer $MoS_2$, 5 min sputter. Adapted from [130].

Recently, Hussain *et al.*[130] reported the highest electron mobility for a FET based on magnetron sputtered $MoS_2$. In their work, the as-deposited film was subjected to post-annealing to improve crystalline quality at 700$^{o}$C in sulfur and Argon environment. They have claimed that the high mobility is originated from low charged impurities of the film and dielectric screening effect arises due to formation of an interfacial $MoO_xSi_y$ layer between $SiO_2$/Si substrate and the $MoS_2$ film, as confirmed by XPS analysis and cross sectional TEM images (see **Figure** 1-39).

In entire attempts to grow $MoS_2$ by magnetron sputtering technique, a high deposition temperature is needed, unless a post annealing is foreseen. However, the optical and electrical properties of the magnetron sputtered $MoS_2$ still drop far below the exfoliated counterpart and further works is still needed to be carried out to obtain a high quality TMDCs film.

# Chapter 2

# Experimental details

## 2.1 Introduction

In this work a wide range of characterization techniques have been used to study the chemical, physical, optical and surface electronic properties of $MoS_2$. Detailed explanation of the techniques and the apparatus used in this thesis are given in the following sections. Among all the applied techniques, since X-ray and ultraviolet photoemission spectroscopy (XPS/UPS) have been widely used, and a major part of the discussions are relying on the results obtained by these two techniques, a further emphasis on explaining the details of the experimental process, apparatus description and fundamentals of photoemission process has been put, in comparison to the other characterizations.

## 2.2 The ultra-high vacuum (UHV) apparatus

In order to perform the core level, valence band and work function (WF) analysis, as well as investigation of the chemical compositions, a UHV apparatus, mainly developed from an original project designed in the Trento IMEM-CNR Laboratory has been used. This apparatus also facilitates the in-situ high vacuum annealing by the heating system installed on the sample holder, through which, the properties of UHV annealed sample can be studied without exposure to the atmosphere.

The main chamber is isolated from a fast-entry chamber by means of gate valve. In this configuration, the sample is being introduced from atmosphere to the fast-entry chamber and by using a manipulator, the inserted sample can be transferred to the main analysis chamber (**Figure** 2-1). In the fast-entry chamber, the final pressure is in the order of $10^{-8}$ mbar. Also, a liquid nitrogen trap in the fast-entry chamber is used to reduce the water vapor flow to the main analysis chamber during sample transference.

### 2.2.1 Main analysis chamber (XPS and UPS)

The analysis chamber (**Figure** 2-1) is made of μ-metal, a special steel alloy able to screen the earth magnetic field and also to significantly reduce the intrinsic magnetism of stainless steel.

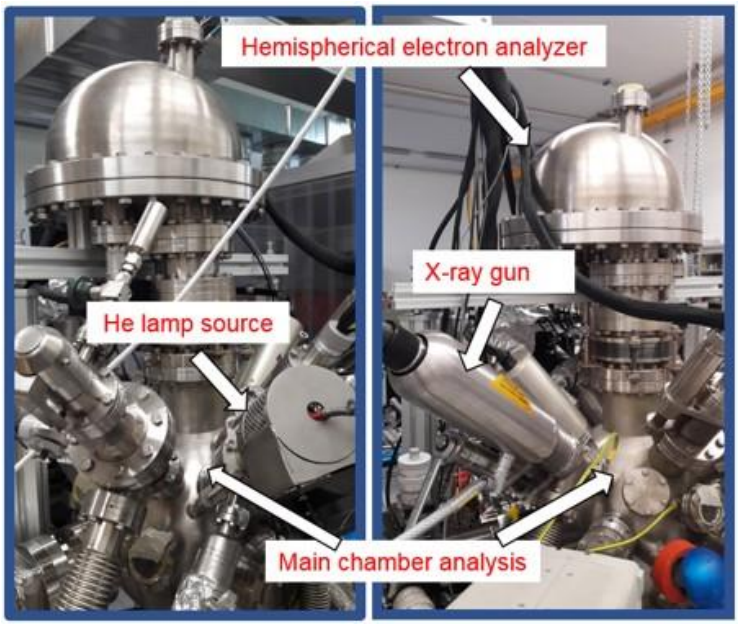


**Figure** 2-1 Main analysis chamber; IMEM-CNR laboratory in Trento, Italy.

This UHV chamber is pumped by a main system constituted by a dry primary pump (Edward, Scroll type 15$m^3$) connected with a magnetic-levitation turbomolecular pump (Edward STP451 MAGLEV); the pumping system is totally dry and oil free. After the bake-out procedure (the entire system is heated up to 150 $^oC$), this pumping system (**Figure** 2-2) assures a base pressure of about $1\times10^{-10}$ mbar. In order to further improve the UHV conditions, down to $5\times10^{-11}$ mbar, the main camber can be pumped by a titanium-sublimation stage together with a liquid nitrogen cold wall.

The analysis chamber is a sphere so that the photons and electrons probing sources radially converge to the chamber focus point (i.e. sphere center). The sample holder is a VG XL25 type, made by a sample carrier with an on-board heater and cooling system (-100$^o$C to 1200 $^o$C temperature range); a thermocouple is present to monitor sample temperature.

The sample is precisely positioned at the focus point by means of a 5 degree of freedom manipulator, which also guarantees the correct sample positioning for both surface analysis and film deposition. A VG HPT type manipulator is used: it allows three translational degrees of freedom (x, y, z movements) and two rotational degrees (Φ, azimuthal and Θ,

polar). Moreover, UHV electrical feedthrough provide electrical contact to bias the sample surface, as well as the necessary wiring to resistively heat the sample and measure of the temperature. Moreover, annealing temperature can also be monitored remotely, through an optical infrared pyrometer, positioned outside the chamber pointing to the sample through a glass window. The infrared pyrometer operates in the temperature range of 300 $^{o}$C up to 1100 $^{o}$C.

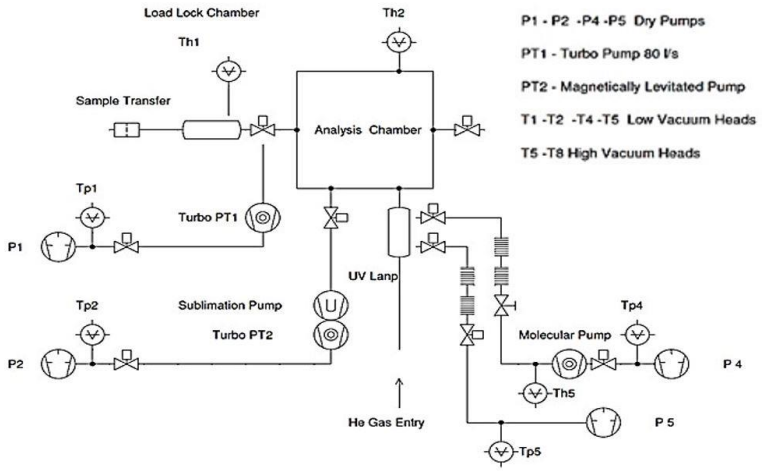


**Figure** 2-2 Sketch of the analysis chamber and the pumping system.

### 2.2.2 Electron energy analyzer

The electron energy analyzer is a hemispherical type (VSW HA100), with a sphere's radius of 100mm. This analyzer acts as a narrow energy pass filter, letting pass only the electrons that have a specific KE, and has three main components: the lenses system, to focalize and adjust initial electron energy, the analyzer, composed by two hemispherical and concentrical lenses, and five Channel Electron Multipliers (so called Channeltrons) to collect and reveal the electrons **Figure** 2-3. Different surface electron techniques exploit this analyzer, namely X-ray and UV Photoelectron spectroscopies (XPS and UPS), Auger electron spectroscopy (AES), electron energy loss spectroscopy (EELS).

Using this analyzer, the maximum energy resolution achieved for XPS and UPS techniques is 0.78 and 0.1eV, respectively, while for AES is 0.5eV. The collection geometry is such that the sample surface is typically normal to the analyzer in XPS, UPS and AES spectroscopies, while excitation sources are positioned at different angles with respect to the sample's surface: **Figure** 2-4 is the scheme of the collection/excitation geometry.

The analyzer is interfaced with a PSP RESOLVE power supply unit which receives signals from the analyzer and gives a digital output signal in terms of counts. Then, the acquisition software (PSP Collect) plots this output as a function of electrons KE (AES, UPS) or binding energy, BE (XPS).

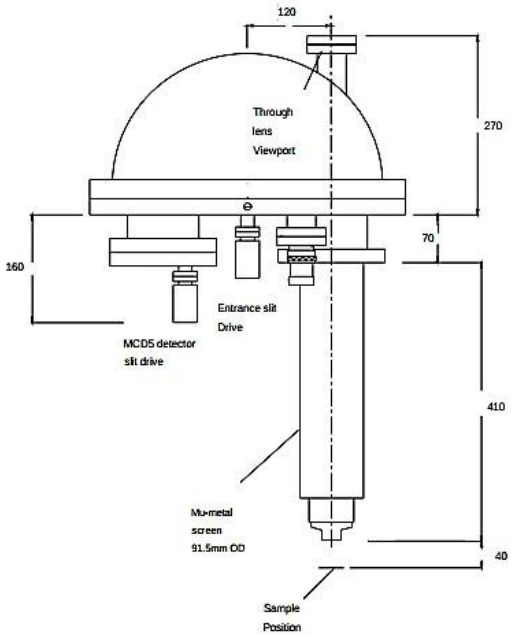


**Figure** 2-3 Scheme of the VSW HA100 electron energy analyzer

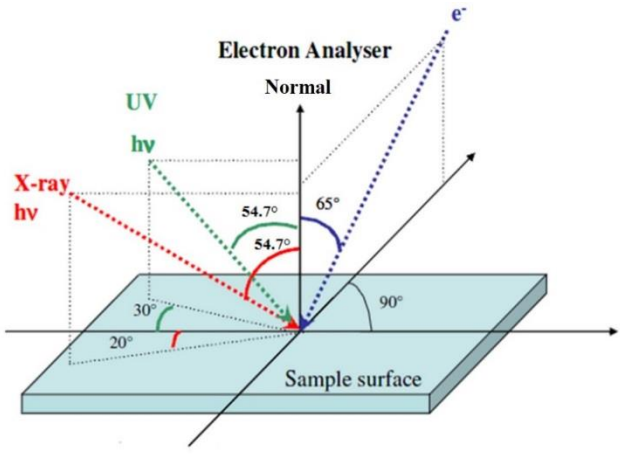


**Figure** 2-4 Excitation and collection geometry referred to sample's surface, for characterization techniques present on analysis chamber.

### 2.2.3 Surface photoemission spectroscopy: an overview

Several surface electron spectroscopies (SES) were used to characterize in-situ and ex-situ the synthesized and grown films, which will be briefly described in the following. SES are

considered surface spectroscopies due to the nature of the electron-matter interaction and the regime they are operated.

Electrons that are emitted from a solid surface undergo several collision and interaction processes with matter before exiting the sample surface. In particular, electrons with a kinetic energy ($KE_{el}$) in the range of 10-1000 eV undergo diffusion processes in the solid and their mean free path (λ) is of the order of about 10 Å. Let's consider now the electron escape probability as a function of the creation's depth. If α is the take-off angle (i.e. the angle between the analyzer and the sample surface) this probability can be written as:

$$P = exp(-d/\sin\alpha) \quad (1)$$

As is clear in **Figure** 2-5a, the large majority of the electrons leaving the surfaces comes from a maximum depth of 4λ.

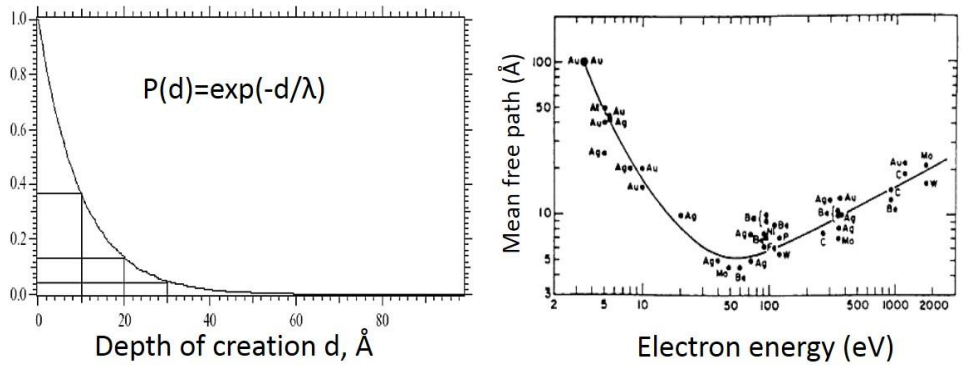


**Figure** 2-5 (a) probability of electrons escaping without loss as a function of their creation depth, for SES. (b) electron escape depth as a function of their KE for various metals.

As can be seen, the escape depth is in the 5-20Å range: taking into account the previous considerations, only the upper surface contributes, and the electrons signal comes from a maximum length 80Å. It is noteworthy that UHV conditions are mandatory for SES, and not only for the strong interaction of escaping electrons with surrounding atmosphere (that would lead to energy loss processes). In fact, assuming that the sticking coefficient for the most common residual gases in a vacuum chamber is 1, at a chamber pressure of $10^{-6}$ mbar it takes only 1sec to completely cover the whole surface, i.e. a coverage of 1 Monolayer (ML) on the surface.

**Figure** 2-5 b represents the electron escape depth as a function of their $KE_{el}$ (this curve is known as the "universal curve").

For pressures in the range of $10^{-9}$ mbar, it takes about 1000s to have the surface fully covered, so that pressures in the low $10^{-10}$ mbar range are necessary to perform a surface spectroscopy experiment for an extended period of time. Emitted electrons can be characterized in energy and spatial distribution. In the first case, instruments are generally based on electrostatic condenser (cylindrical or hemispherical), biased in such a way that only electrons having specific velocity (i.e. kinetic energy) will reach the final detector, while the others will hit the internal surface of the condenser. Energy analysis is thus achieved by using a voltage ramp applied to the condenser plates.

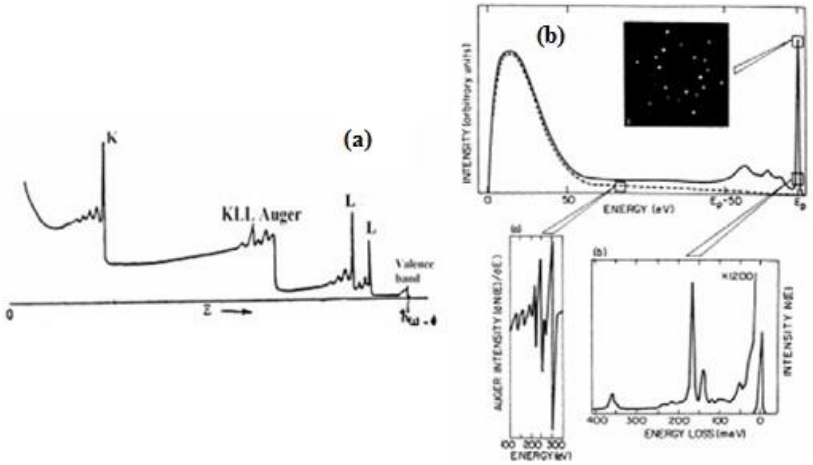


**Figure** 2-6 (a) photoelectron spectrum showing the several electrons emitted by the surface: core electrons (K and L shell), Auger electrons, VB valence band electrons. b) Energy distribution of scattered electrons: example of the Rh (111) surface covered by ethylene. The elastic peak and together with the losses and Auger peaks are outlined in the panels. Adapted from [170].

By using this apparatus, different surface electron spectroscopies can be performed.

- ***X-ray Photoelectron spectroscopy (XPS):***

This technique is based on the photoelectric effect, by means of which when a surface is hit by X-ray photons, their energy (from few hundreds of eV to thousands of eV) can be absorbed by an electron of a core level, thus escaping original parent atom, and from the surface sample.

**Figure** 2-7 is an outline of this process: electrons are generated from a core level and leave the surface with a $KE_{el}$ that depends, in a first approximation, from the initial photon energy, the binding energy and the work function of the solid.

The fundamental relationship that describes the photoemission process traces that used for the first photoelectric experiments:

$$KE_{el} = h\nu - BE - \phi \quad (2)$$

where $KE_{el}$ is the final electrons kinetic energy, BE the binding energy they had in the solid (i.e. the binding energy of core level from which they were ejected) and ϕ the work function of the system (considering the sample in electric contact with the analyzer, and at the same ground potential).

This relationship is based on the so called *one-electron approximation.* A more accurate description of the processes involved in the photoelectron process requires to take into account:

1. the relaxation processes occurring in the excited parent atom that has N electrons at the beginning, while in the final state becomes an ion having N-1 electrons;
2. the energy loss processes that electrons experience while moving in the solid (electron-phonon coupling and plasmon losses).

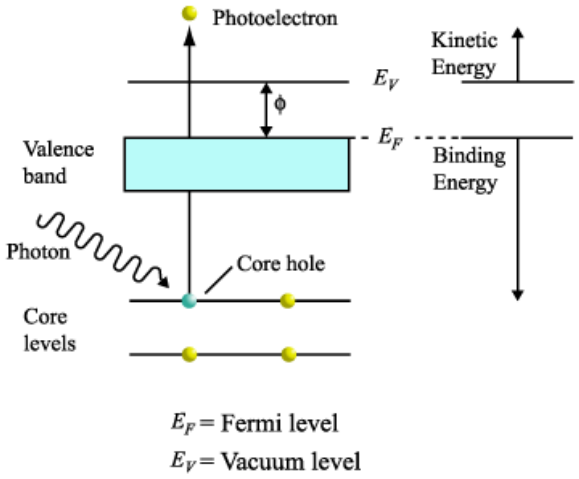


**Figure** 2-7 Scheme of the photoemission process.

These processes lead to a final energy distribution that is composed of main features, reflecting the core level density of states, and secondary peaks, due to transport processes. The photoemission process is so fast that is usually described under the so-called sudden approximation: the system cannot reach the equilibrium state prior to the photoemission; hence the final state can have two configurations. In the first configuration one electron lies in one atomic excited state, while in the second an electron is ejected, leaving the atom double ionized. These processes decrease the $KE_{el}$ of the photoemitted electrons and give rise to satellite peaks, such as the so-called shake-up and shake-off features. A detailed

description of these processes is beyond the scope of this thesis and can be found in Ref. [171].

The photoelectron spectrum is obtained by measuring the $KE_{el}$ of photoemitted electrons and plotting the intensity (usually expressed as counts per seconds) versus the $KE_{el}$. It consists of several features: core-hole lines, shake-up and shake-off excitations, Auger peaks, valence band peaks and secondary peak due to minor physical processes.

XPS is a powerful technique in surface science since it allows the observer to get information about the chemical properties and the elemental composition of the studied surface (see sketch in **Figure** 2-8).

Elemental characterization is possible due to the intrinsic uniqueness of each atom electronic configuration, just by evaluating the Binding Energy position.

Quantitative analysis can be performed measuring the peak area associated to an element, weighted by a sensitivity factor that takes into account the excitation efficiency of each element.

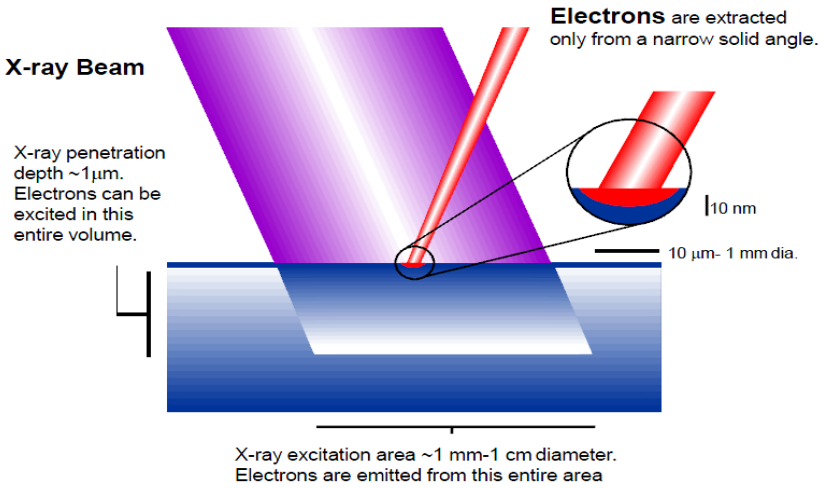


**Figure** 2-8 XPS probing area and surface sensitivity.

For a homogeneous sample with an isotropic elastic diffusion of the photoemitted electrons, the photocurrent intensity can be expressed as:

$$I_i(KE_{el}, i) = I * N_i * \sigma_i(k) * \lambda(KE_{el}) * H \quad (3)$$

where I is the incident photon flux, N the atomic concentration of the i-species, $\sigma_i$ the ionization cross section referred to the level i and to the incident photon, $\lambda(KE_{el})$ the escape

depth length at the $KE_{el}$, H an instrumental factor. Since ab-initio calculation of some of the factors in equation (3) is quite difficult, the general procedure for this type of analysis is the use of calibrated quantities and of the atomic sensitivity factors (ASF), which take into account the excitation probability of the element *i*, for a certain impinging photon. In such a way the relative atomic concentration of the element *i* can be expressed as:

$$N_i = \frac{A_i}{ASF} \quad (4)$$

in which the peak intensity is its integrated area $A_i$. The ASFs, which are also defined for the AES peaks, are tabulated taking as a reference the element *i* in a standard state.[171]

- **Ultraviolet photoemission spectroscopy (UPS):**

As excitation sources UPS uses UV photons the energy of which ranges from few eV up to few hundreds of eV. The main difference from the XPS spectroscopy hence is that only the most external electronic levels of single atom, molecular bands (Highest Occupied Molecular Orbital, HOMO, for example) of aggregates and high-laying energy bands in the case of solids (valence band maximum, VBM for semiconductors, for example) are involved in the process of photoelectron production. UPS has a probing depth of ~15Å and it is therefore used to extract important information about interaction processes involving the external electronic levels.[172]

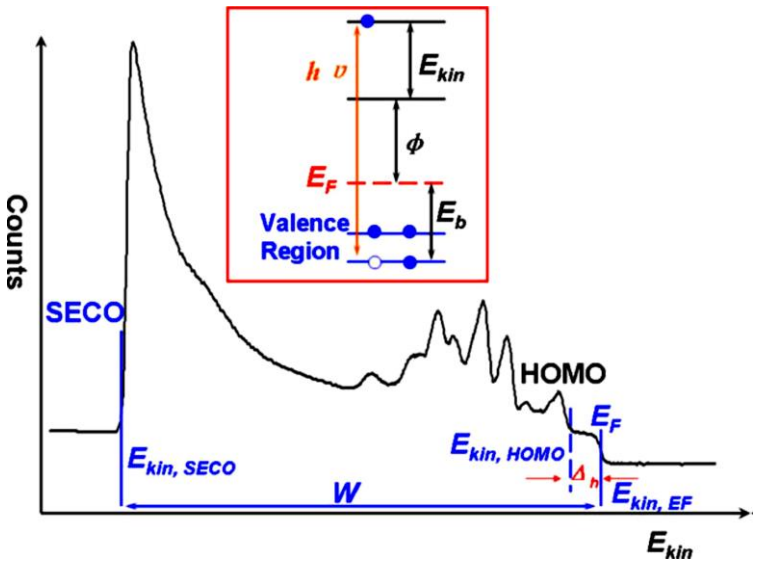


**Figure** 2-9 Typical UPS spectrum. The inset shows the photoelectron emission process in a PES experiment. Adapted from [173].

The photoelectric effect generates free electrons with a $KE_{el}$ which depends on the exciting photon energy *hv*, the work function of the sample ($\varphi$, that is the minimum amount of energy

needed to remove an electron from the sample), the binding energy of the excited electron and the inelastic scattering events in the sample.

**Figure** 2-9 represents a typical UPS spectrum, that can be divided in two regions:

- the left part is the low $KE_{el}$ secondary-electron region, that represents the secondary electron cut-off (SECO). This cut-off, named photoemission onset, is associated to the vacuum level ($E_{vac}$), since electrons with less energy cannot come out from the solid. This onset gives the position of $E_{vac}$ with respect to other photoemission features such as the highest occupied molecular orbital (HOMO) or valence band maximum (VBM).
- the right part is the high $KE_{el}$ valence band region, typically characterized by the presence of Fermi level (for metals) and VB offset, as well as HOMO (for molecules) or VBM for semiconductors.

From the spectrum is possible to calculate the sample work function in according to the following equation (5):

$$\varphi_{sample} = h\nu - w = h\nu - \left(E_{Kin,EF} - E_{Kin,SECO}\right) \quad (5)$$

where $E_{Kin,EF}$ and $E_{Kin,SECO}$ are the $KE_{el}$ of the sample Fermi level and the SECO respectively, and *w* is the spectrum width (the $KE_{el}$ difference between $E_{EF}$ and SECO).

In the case of a semiconductor, the Fermi level is located within the band gap (**Figure** 2-10), so that it is not possible to calculate the work function directly from the spectrum, but we have to consider the ionization potential (*IP*), calculated as the energy difference between the leading edge of the HOMO peak and the vacuum level.

In this case the work function can be calculated as difference between *IP* and the quantity ε, defined as the difference between Fermi level and HOMO:

$$\varphi_{sample} = IP - \varepsilon \quad (6)$$

Work function changes in the order of 1 eV are typical in metal and semiconductors depending on the surface conditions. These variations are generated by electric dipoles at the surface, which can change the amount of energy required for an electron to leave the sample.

For organic materials, ionization potential (*IP*) is calculated from the UPS spectrum as the difference energy between the HOMO and the vacuum level. In a similar manner to the equation (5) *IP* is calculated by the relation:

$$P = h\nu - \left(E_{Kin,HOMO} - E_{Kin,SECO}\right) \quad (7)$$

where $E_{Kin,HOMO}$ is the linear extrapolation of the high-KE of the HOMO peak.[174]

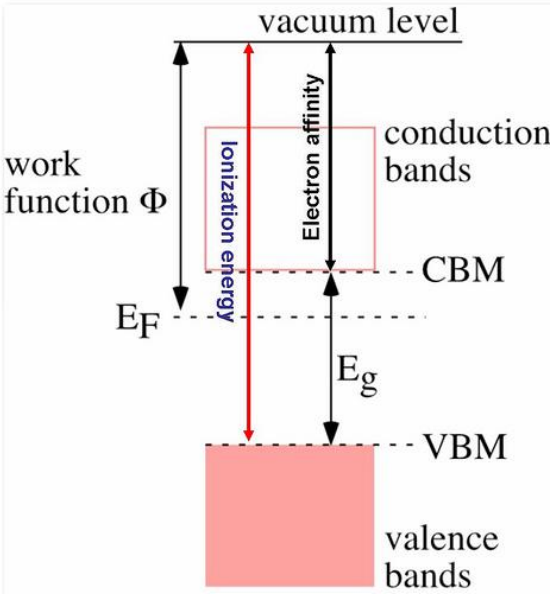


**Figure** 2-10 Scheme of the energy levels in a semiconductor.

Irrespective of the nature of the sample analyzed, for a correct measurement of the SECO, it is necessary to consider the secondary electrons of the analyzer as well, which are generated by the impact of the sample photoelectrons with the surface analyzer. These electrons are superimposed to the secondary edge of the sample spectrum and make difficult to determine the position of the secondary edge of the sample. To overcome this problem, an accelerating potential (Bias) is applied between sample and analyzer: electrons coming from sample are accelerated and the spectrum is shifted ahead respect to the analyzer secondary electrons in order to distinguish sample and analyzer secondary edges. In this work, we applied for all the characterizations a bias of -7V.

In this thesis, the XPS and UPS analysis were performed as follow: after thermal treatment (when necessary), XPS and UPS analyses were achieved with a non-monochromatized Mg Kα X-ray source (emission line at 1253.6 eV) and a helium discharge lamp (emission line at 21.21 eV). The total resolution was 0.8 eV for XPS and 0.10 eV for UPS analysis. The binding energy (BE) scale of XPS spectra was calibrated by using the Au 4f peak at 84.0 eV

as a reference, while UPS BEs were referred to the Fermi level of the same Au clean substrate. Core level analyses were performed by Voigt line-shape deconvolution after background subtraction of a Shirley function.

### 2.3 μ-Raman and photoluminescence (PL)

Non-resonant Raman and PL spectra were acquired at room temperature using a LabRAM Aramis (Horiba Jobin-Yvon), which is equipped with a diode-pumped solid-state laser line of 532 and 630 nm. The laser line was focused on the sample by a 100× objective lens. The luminescence signal was monitored with a double monochromator equipped with a cooled photomultiplier in the photon counting mode, whereas Raman spectra were detected with an air-cooled charge-coupled detector (CCD). The collected light was dispersed by an 1800 grooves/mm spectrometer. In Raman spectra acquisition, the Rayleigh line below 100 $cm^{-1}$ was filtered and also, the Silicon Raman band which is located at 520 $cm^{-1}$ was used as reference. The resolution of the spectra obtained was 1 $cm^{-1}$. All analyzes have been carried out in the lab of IFN-CNR institute, in Trento.

### 2.4 X-ray diffraction (XRD)

X-ray diffraction is being widely used in experimental science to study the atomic and molecular structure of a crystal, in which crystalline structure causes a beam of x-rays to be diffracted to many specific directions. Based on measuring the angles and intensities of diffracted beam, one can reproduce an image representing the crystallographic information.

The XRD measurement of the samples in this thesis, have been carried out at Engineering Department of University of Trento in Italy. XRD spectra were collected on films with a Rigaku D/max III diffractometer in glancing incident configuration, using Cu Kα radiation and a graphite monochromator in the diffracted beam. Asymmetric scan geometry was adopted in order to enhance the signal stemming from the IJD-$MoS_2$ thin film. The typical measurements were performed in the 2Θ range of 10-70$^o$ with an incidence angle of 1$^o$, sampling interval of 0.05$^o$, and counting time of 8 s.

### 2.5 Transmission electron microscopy (TEM)

Transmission electron microscopy (TEM) is a very powerful tool to characterize the materials in sub micrometer scale. In this technique, a high energy beam of electrons is shone through a very thin sample (usually less than 1μm), and the interaction between the electrons

and the atoms can be used to observe features such as crystal structure and features in the structure like dislocations and grain boundaries. Moreover, TEM can be used to study the growth layers, compositions and defects in semiconductor materials.

The TEM apparatus, principally operates in the same way as light microscope, but since it uses electrons instead of light, the optimal resolution attainable for TEM images is many orders of magnitude better than that from a light microscope. Thus, TEMs can reveal the finest detail of internal structure, in some cases as small as individual atoms.

A typical TEM apparatus mainly consists of three components:

- The illumination system: it is compromised by the gun and condenser lenses; the latter one is for collecting the electrons coming from the gun and guide them through the specimen.
- The objective lens: is responsible for magnifying the image
- The imaging system: this section is an arrangement of several lenses to magnify the image coming from the objective lenses and to project the image on to a visualizer i.e. phosphorescent screen

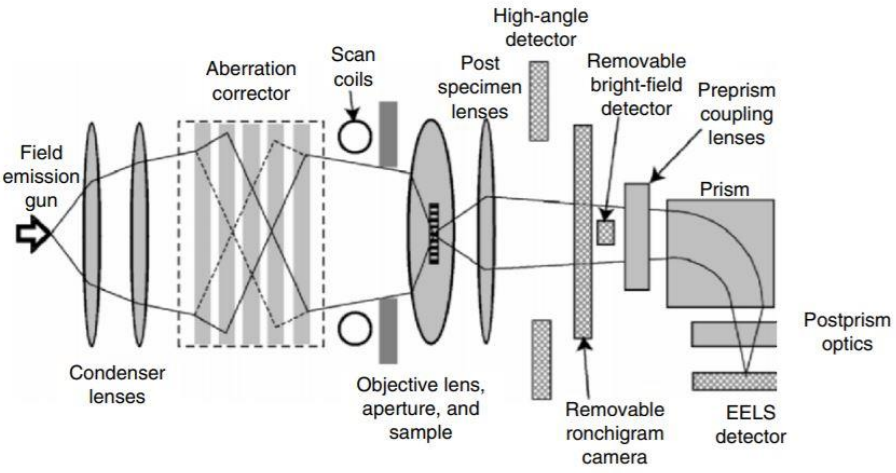


**Figure** 2-11 Simplified schematic of an aberration-corrected STEM. Adapted from [175].

TEM analysis of the samples described in this work have been performed at IMEM-CNR Institute in Parma, Italy, by means of a JEOL 2200FS microscope operating with 200 kV in scanning (STEM) mode.

## 2.6 Electron energy loss spectroscopy (EELS)

Due to the broad range of inelastic interactions of the high energy electrons with the specimen atoms, ranging from phonon interactions to ionization processes, electron energy-loss spectroscopy (EELS) offers unique possibilities for advanced materials analysis. It can be used to map the elemental composition of a specimen, but also for studying the physical and chemical properties of a wide range of materials and biological matter. Electron energy-loss spectroscopy (EELS) is an analytical technique that is based on inelastic scattering of fast electrons in a thin specimen. In a transmission electron microscope (TEM) it can provide structural and chemical information about a specimen, even down to atomic resolution.[176]

For some materials (especially wide band gap materials), the band gap ($E_G$) from low-loss spectra obtained by EELS technique can be determined by eye observation of the single scattering distribution (SSD) spectrum. In this case, $E_G$ is defined as the energy corresponding to the first onset in the spectrum, for instance, 0.67 and 1.12 eV for Ge and Si respectively, in the schematic spectra in **Figure** 2-12.

In this thesis work, electron energy loss spectroscopy (EELS) was carried out with a Leybold electron gun (EQ2/35) operated at 1000 eV of primary beam energy and a CLAM2 (VG Microtech) electron analyzer, with a resolution of 0.1 eV. Electron beam current on the sample was 2nA. The analysis was carried out at the Engineering Department "E. Ferrari", University of Modena and Reggio Emilia.

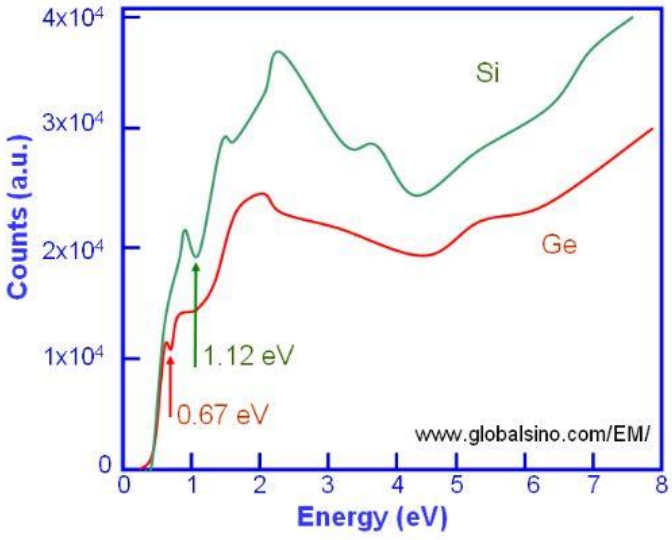


**Figure** 2-12 Schematic illustration of Si and Ge SSD spectra in the low-energy range. Adapted from [globalsino.com/EM/].

## 2.7 Scanning tunneling microscopy & spectroscopy (STM/STS)

Scanning tunneling spectroscopy can provide information about the density of state of electrons as a function of energy. In the measurement set-up, as schematically shown in **Figure** 2-13, a metal tip is moving on the surface of the sample without making a physical contact. Since, a bias voltage is applied between the moving metal contact and the sample, a current flow between the two occurs. This is as a result of quantum tunneling across a barrier, which is the distance between the tip and the sample.

STS can provide fruitful information regarding surface electronic states, band gap, the in-gap defect states etc. [63,75] At its simplest, a scanning tunneling spectrum is obtained by positioning an STM metal tip above a particular place on top of the sample, in which the distance between tip and the surface is fixed; then the electron current is being measured as a function of electron energy by varying the voltage between the sample and the tip. (see **Figure** 2-13) As a result, the plot representing the varying current as a function of electron energy will be obtained.

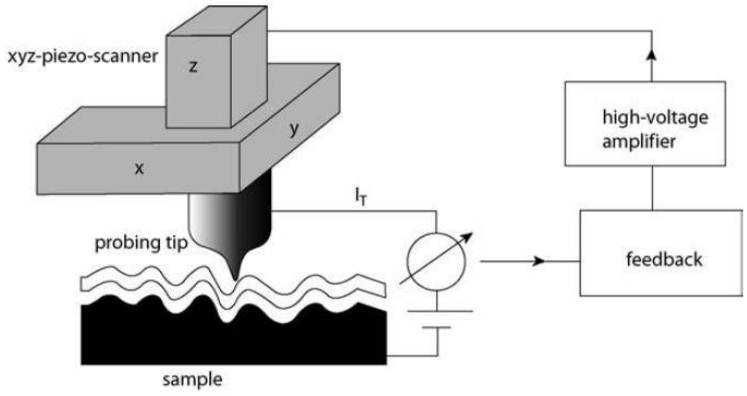


**Figure** 2-13 The scanning tunneling microscope (STM) system. The scanner moves the tip over the sample surface and the feedback loop keep the tunneling current constant.

In this thesis, the STS/STM has been used to study surface electronic stats of the IJD deposited $MoS_2$ films. The STM images were acquired in an ultra-high vacuum (pressure in low $10^{-10}$ mbar range) chamber in constant mode at room temperature, using an Omicron multiscan system. The Pt/Ir tip was prepared by electrochemical etching in saturated CaCl2 aqueous solution and subsequently cleaned in UHV by electron bombardment. Before the measurements, all the samples were degassed at approximately 120$^{o}$C at a pressure below $5\times10^{-10}$ mbar for at least 3 h up to 10 h, and subsequently moved to the scanner without

breaking the vacuum. The STM images were recorded in constant current mode with tip to sample bias ranging from -0.7 V to -2 V and tunneling current ranging from 0.5 nA to 2 nA.

Scanning tunneling spectroscopy (STS) data were acquired by the sample-and-hold technique at room temperature. For each point, the I-V and dI-dV curves were collected. The dI-dV curve was obtained by applying to the bias potential a modulating voltage of 20 mV and collecting the derivative with a lock-in amplifier. The stabilizing conditions for the different points are Vbias in the range of -1.6 to 2.0 V, and the I in the range of -0.5 to 2.0 nA. Each curve was obtained by averaging over more than 20 individual spectra to improve the signal-to-noise ratio. The DOS was calculated following eq. 3 in Ref. [177], that is independent on the tip to sample distance.

The measurement has been carried out at Dipartimento di Matematica e Fisica, Università Cattolica del Sacro Cuore, Brescia.

# Chapter 3

# Surface electronic properties of 2H-$MoS_2$

## 3.1 Introduction

In **Chapter** 1, the importance of obtaining a comprehensive understanding on the surface electronic properties of TMDCs materials and the role of sulfur vacancies has been precisely discussed. We showed the unresolved conflicts in the literature and the necessity of further investigation of the role of sulfur vacancies. In this chapter, our attempt on further elucidating the surface electronic properties of $MoS_2$ will be discussed.

## 3.2 Surface electronic properties of 2H-$MoS_2$ single crystal: role of sulfur defects

To fully harness the potential of $MoS_2$ and widen its application prospect, different studies concerning surface reactivity and chemical composition were done. In this scenario, sulfur vacancies, which are the most abundant defects play a crucial role, since they are found to be chemically more reactive[85] than the perfect lattice and they have the tendency to react with molecules or atoms, (i.e. dopants available, contaminants, as radicals species etc.), to form strong bonds.[103] This fact originates from the formation of unpaired electrons present along the edges and lattice defects of $MoS_2$.[105] It has been found that, regardless of the way $MoS_2$ has been prepared, either synthetic or natural flakes, different types of sulfur vacancies such as mono, double, tri, (multi-) line, and/or clusters are present.[178–181] In many studies,[12,71,91,95,101,102,105] the potential of sulfur defects has been exploited to functionalize $MoS_2$ with a variety of molecules containing thiol as an anchoring group. However, a deep investigation of the role of sulfur vacancies and surface stoichiometry on the electronic structure of 2H-$MoS_2$ and its implication on the surface reactivity and functionalization has not yet been reported. Recently performed density functional theory (DFT) calculations[182] predicted that thiol-derived molecules with electron-donating moieties promote a sulfur vacancy repairing reaction, whereas electron withdrawing groups facilitate the surface functionalization of $MoS_2$. As an instance, Nguyen *et al.*[183] functionalized $MoS_2$ with a variety of organic thiols with different electron-withdrawing capabilities, for tuning the electronic levels of $MoS_2$ flakes, which could pave the way for producing more efficient

electronic devices such as light emitting devices, photodetectors as well as solar cells.[184] Based on the above-mentioned studies, a more detailed knowledge of the phenomena at the surface of $MoS_2$, that leads important chemical and electronic modification such as generation of superficial dipoles, surface charge redistribution, and work function change, with respect to the amount of surface defects and functionalizing molecules becomes of fundamental importance. To maximize the benefit from molecular functionalization, the coverage can be improved with a high density of anchoring sites promoting the chemical reactivity. Since the sulfur vacancies present on the edge and the basal plane of $MoS_2$ are found to be the active sites for the thiol group, it can be inferred that the functionalization efficiency depends on the amount of sulfur vacancies present on the edge and basal plane of $MoS_2$.[102] In the case of $MoS_2$ nanoflakes derived by chemical or mechanical exfoliation, due to the harsh nature of the processes, the yielded product is highly defective and suitable for efficient functionalization processes.[185] A remarkable functionalization efficiency has been achieved, in particular due to the high number of edge defects present on the flakes.[95,103,186] However, this is not the case for large-area $MoS_2$ layers, which can be obtained by chemical vapor deposition (CVD), pulsed laser deposition (PLD), or other scalable synthesis techniques, since the edges play a minor role and the material properties are dominated by the basal plane.

The purpose of the experiment we performed was to investigate the change of both electronic structure and reactivity of highly stable 2H-$MoS_2$ single crystal (as a paradigm of layered structure of $MoS_2$), after thermal annealing and introducing sulfur defects.

### 3.3 Experimental procedure

To systematically investigate the influence of sulfur defects on surface electronic properties of 2H-$MoS_2$, in-situ vacuum annealing has been employed to intentionally introduce sulfur defects; this process has been followed by XPS/UPS measurements to trace the core level changes, as well as valence band and work function. To further evaluate the chemical reactivity and electronic level changes of defective surface, a thiol molecule has been used as a molecular probe. Molecular interaction with thiol derivatives is expected to passivate the sulfur defects, hence, brings further clarification on the effect of defects on surface electronic levels such as work function and surface band bending. Furthermore, as the sulfur defects found to be the active sites, facilitating the thiol-functionalization of $MoS_2$, an

enhancement in the functionalization degree is expected in the functionalized defective $MoS_2$.

The experimental process flowchart comprising of sulfur defects generation and the following surface electronic studies of the sample is schematically given in **Figure** 3-1.

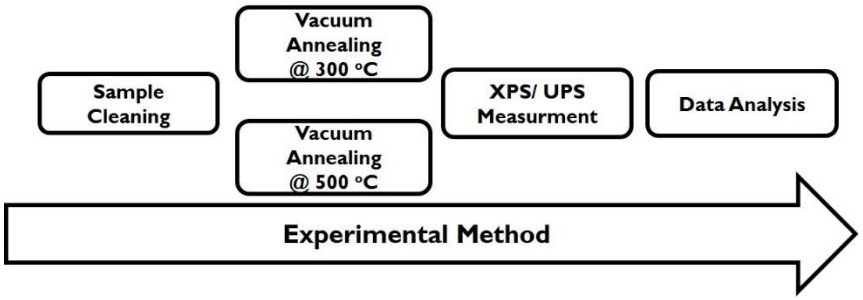


**Figure** 3-1 Experimental process flowchart 1: investigation of the influence of defects on surface electronic properties of $MoS_2$.

The second part, which is attributed to molecular interaction of the thiol-molecule with defective surface and the consequent electronic level changes is schematically given in **Figure** 3-2.

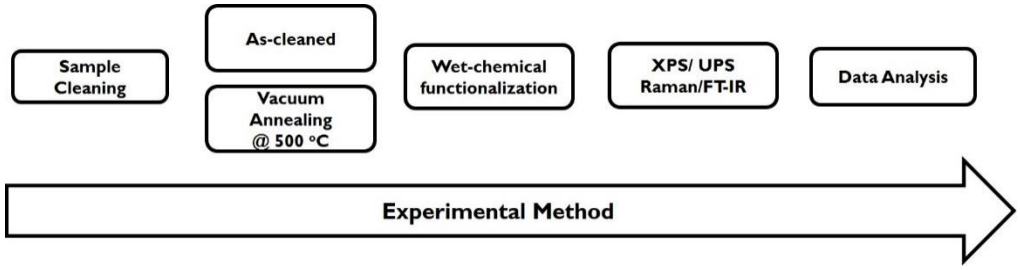


**Figure** 3-2 Experimental process flowchart 2: thiol-molecule interaction with defective $MoS_2$ and the consequent electronic properties modification.

In each experimental process, several samples have been prepared and studied to validate and confirm the experimental results. More details on the experimental parts are given in the following section.

### 3.3.1 Sample preparation

Thermal treatment and surface functionalization were carried out on $MoS_2$ bulk single crystals (SPI Supplies, purity >99.9%). To eliminate the surface contaminations which may possibly be present on the as-received sample, a routine cleaning process has been carried out. The as-received crystals were sonicated in trichloroethylene, acetone, and 2-propanol consequently for 10 min in each solvent and finally dried with a nitrogen gas flux. In order

to exclude any potential effect of the typical contaminants stemming from the atmosphere (i.e. oxygen, carbon and nitrogen) in the surface phenomena, the C 1s, O 1s and N 1s core levels spectra of the as received and solvent cleaned $MoS_2$ single crystal is given in **Figure** 3-3. The C 1s, O 1s, and N 1s core levels reported in the panel a, b and c, respectively prove that neither carbon, oxygen, nor nitrogen were present on the pristine and solvent cleaned $MoS_2$ single crystals before thermal annealing in UHV.

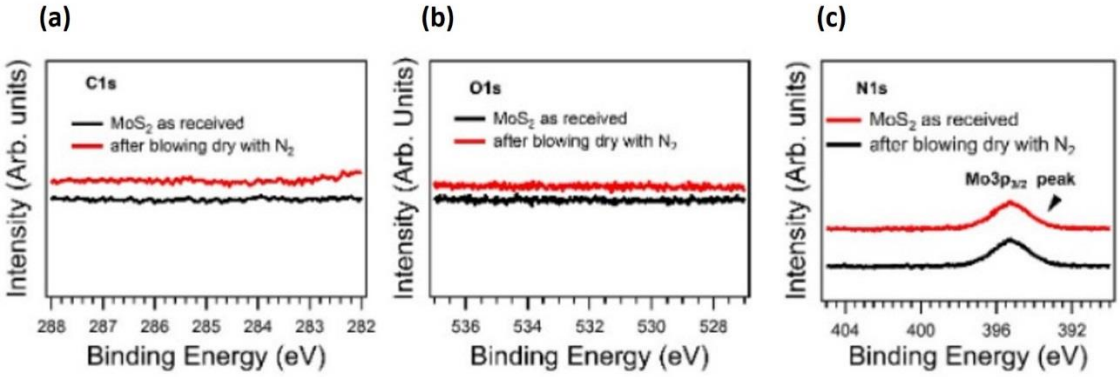


**Figure** 3-3 XPS analysis of $MoS_2$ single crystal as received and after solvent cleaning: (a) C1s, (b) O1s and (c) N1s core levels, before and after solvent cleaning and $N_2$ blowing.

### 3.3.2 In situ ultra-high vacuum annealing

In order to introduce sulfur vacancies in a controllable manner, thermal treatment has been carried out in an ultrahigh vacuum chamber with a working pressure of $\sim 4 \times 10^{-10}$ mbar. More detailed information on the UHV chamber and the annealing system is given in **section** 2.1.

The samples were heated at two different temperatures, 300 (TT300) or 500 °C (TT500), each for 1 h. In the following, the thermally treated samples are denoted as TT300 and TT500. It is assumed that thermal treatments at two different temperatures would yield $MoS_2$ with two different surface defect densities.

### 3.3.3 Characterizations: overview

To study the influence of sulfur vacancies generated by vacuum thermal annealing on surface electronic properties of 2H-$MoS_2$ single crystal, and the effect of post-process surface thiol functionalization on pristine and defective samples a wide range of spectroscopies have been used. Among those, XPS analysis was used to trace the possible core level properties, while UPS analysis was used to study the valence band, surface electronic states and the relative changes on Fermi level position and work function. The surface functionalization of 2H-$MoS_2$ by thiol molecules, was investigated by μ-Raman and FT-IR analysis in order to

validate the functionalization protocol and investigate the chemical interaction within thiol molecule and the surface Sulphur defects. In particular shifts in the position of the two characteristic Raman mode of 2H-$MoS_2$ is an indication of the strength of the formed bond between molecule and the substrate.[187] Hence the quality and the nature of the functionalization can be assessed by µ-Raman analysis. FT-IR analysis can provide further proofs on the presence of chemical species attributed to the molecule on the surface of $MoS_2$, which is also an indication of successful functionalization of the substrate.

More detailed information on the characterization tools and the applied parameters are given in **Chapter** 2.

### 3.4 Work function changes in defective 2H-$MoS_2$: contribution of dipole components

In-situ UHV annealing at two different temperature has been used to introduce sulfur vacancies. In order to investigate the induced changes on chemical states and electronic properties of the surface, XPS analysis has been carried out. The Mo 3d and S 2p core levels of pristine and thermally treated $MoS_2$ single crystals are shown in **Figure** 3-4.

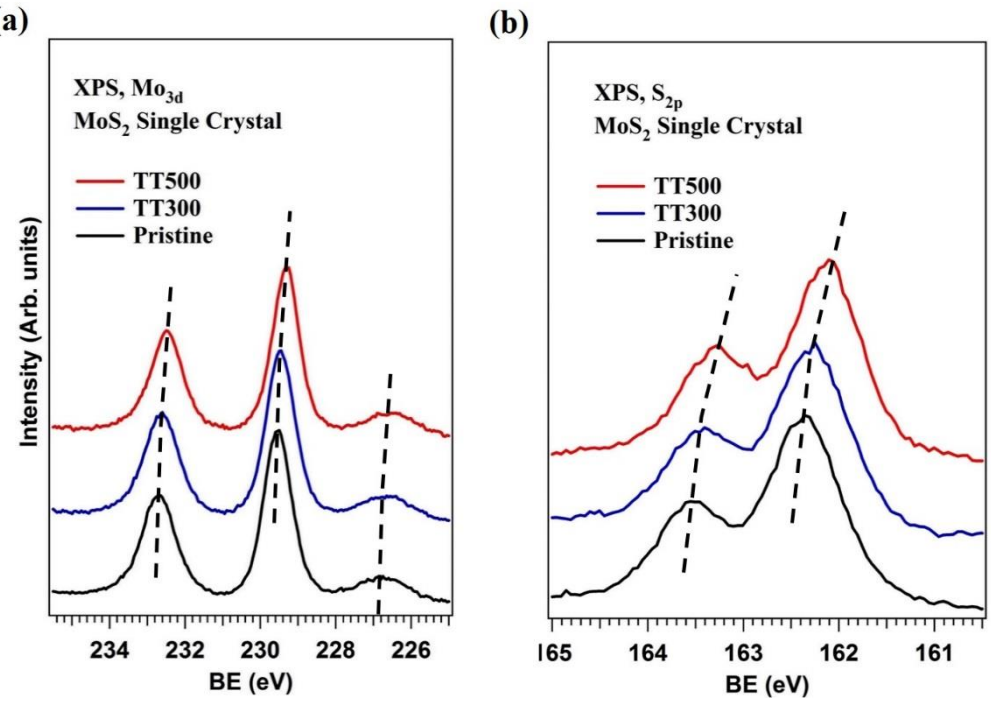


**Figure** 3-4 XPS characterizations of pristine and annealed $MoS_2$: (a) Mo 3d and (b) S 2p core level spectra of pristine and thermally treated (TT300 and TT500) 2H-$MoS_2$ single crystals.

The binding energy shifts of the thermally treated samples with respect to the pristine one and the relative stoichiometry are summarized in **Table** 3-1.

The peak corresponding to the Mo 3d5/2 core level of the pristine sample was found to be at a binding energy (BE) of 229.55 eV, whereas the S 2p peak was found at 162.36 eV, as already reported.[188] After annealing, for both core levels lineshape does not change, suggesting that no important change in the chemical state took place with the annealing. However we observe a rigid shift to lower BEs of -0.10 and -0.25 eV for TT300 and TT500, thus increasing with the treatment temperature, which once more is in agreement with previous findings.[86] Moreover, the stoichiometry evaluated by the ratio between the S 2p/Mo 3d peak areas was found to be 1.92 for the pristine 2H-$MoS_2$ and decreases to 1.86 and 1.72 for the TT300 and TT500 samples, respectively (**Table** 3-1).

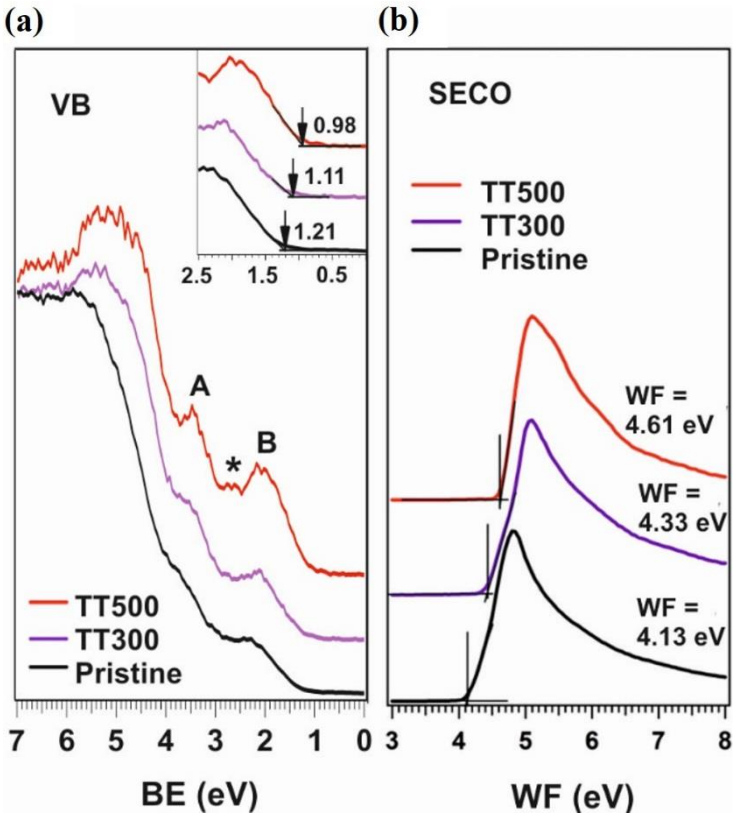


**Figure** 3-5 UPS characterizations of pristine and annealed $MoS_2$: (a) Valence band region and (b) SECO spectra. The inset in panel a) shows zooms into the near $E_F$ region.

The gradual decrease of stoichiometry ratio is a first clear evidence of sulfur loss on the surface. As stated before, in previous studies[83,85,86] downward shifts of the core levels due to thermal annealing has been reported and related to excess of negative charge on the surface. On the other hand, it has been shown that sulfur vacancies are the origin of surface electron accumulation.[75] This effect can be originated from the removal of sulfur from the surface, leaving behind an excess of molybdenum atoms with electron lone pairs (see schematically in **Figure** 3-6a). As a result, it can be inferred that, introducing more sulfur vacancies by

means of UHV annealing at increasing temperatures, would lead to further excess of negative charge on the surface. Thus, the surface is enriched with negatively charged sulfur vacancies.[189] This makes the surface locally more negative; however, the surface remains globally neutral and not in an anionic state. Moreover, since sulfur vacancies have the lowest formation energy among all of the possible defects in the $MoS_2$ lattice,[190] they are expected to be the most abundant defects on the surface after thermal treatment.

Concerning UPS analysis, as shown in **Figure** 3-5 the valence band maximum (VBM) of the thermally treated samples is found at lower BEs, in agreement with the core level shifts. In fact, the VBM shift for both samples TT300 and TT500 is almost equal to the shift in the corresponding Mo 3d and S 2p core levels, being -0.10 and -0.23 eV respectively.

**Table** 3-1 Binding Energy (BE), Valence Band Maximum (VBM), and Work Function (WF) Values and Corresponding Changes in Pristine and Thermally Treated Samples.

| | **$Mo3d_{5/2}$ (ΔBE) [a]** | **$S2p_{3/2}$ (ΔBE) [a]** | **VBM (ΔBE) [a]** | **WF (ΔWF) [a]** | **S/Mo [2.0]** |
|---|---|---|---|---|---|
| **Pristine** | 229.55 | 162.36 | 1.21 | 4.13 | 1.92 |
| **TT300** | 229.45 (-0.10) | 162.26 (-0.10) | 1.11 (-0.10) | 4.33 (+0.20) | 1.86 |
| **TT500** | 229.30 (-0.25) | 162.11 (-0.25) | 0.98 (-0.23) | 4.61 (+0.48) | 1.72 |

[a] BE, ΔBE, and WF are expressed in eV

Besides VBM shifts, we observed that the two major states at around 3.8 and 2.4 eV (labeled as A and B in **Figure** 3-5a) appeared more prominent after annealing at 300 °C. By further increasing the temperature up to 500 °C, another state located between the two latter ones appeared at around 3.0 eV (labeled as * in **Figure** 3-5a). As already reported in some studies based on density functional methods,[191,192] it can be related to new defect-induced electronic states. In **Figure** 3-5b the corresponding secondary electron cutoff (SECO) spectra of the samples are reported. Thermal treatments lead to an increase in the work function of +0.20 and +0.48 eV for TT300 and TT500, highlighting a p-type behavior[193,194]of the thermally treated $MoS_2$ surface. It is noteworthy that any gas adsorption (such as oxygen/water and/or nitrogen) at S vacancies that has been previously shown to induce p-type doping[50,195] can be ruled out, since pristine samples showed no detectable contaminations (see **Figure** 3-3a-c), and both annealing and analysis were performed in the same UHV chamber. The information

regarding core levels positions, VBM and the WF of pristine and thermally treated samples, as well as the stoichiometry changes are summarized in **Table** 3-1.

The origin of WF change and the underlying mechanism can be understood by considering the chemical environment of an individual sulfur vacancy, as shown in **Figure** 3-6 a. After S removal, an excess of negative charge ($\delta^-$) is generated by the electron lone pair localized on the topmost Mo center with respect to the Mo center in the next $MoS_2$ layer ($\delta^+$). Even though there might be some interlayer charge compensation due to the repulsive Coulombic interaction in the topmost vacancy-rich $MoS_2$ layer, the absence of covalent bonds between the different $MoS_2$ layers (only vdW forces) will not allow for full charge compensation, leading behind a net excess of negative charge localized on the topmost $MoS_2$ layer. Hence, modification of the surface occurred due to the introduction of surface defects by annealing the bulk single crystal 2H-$MoS_2$ so that the electrostatic field close to the surface changes.

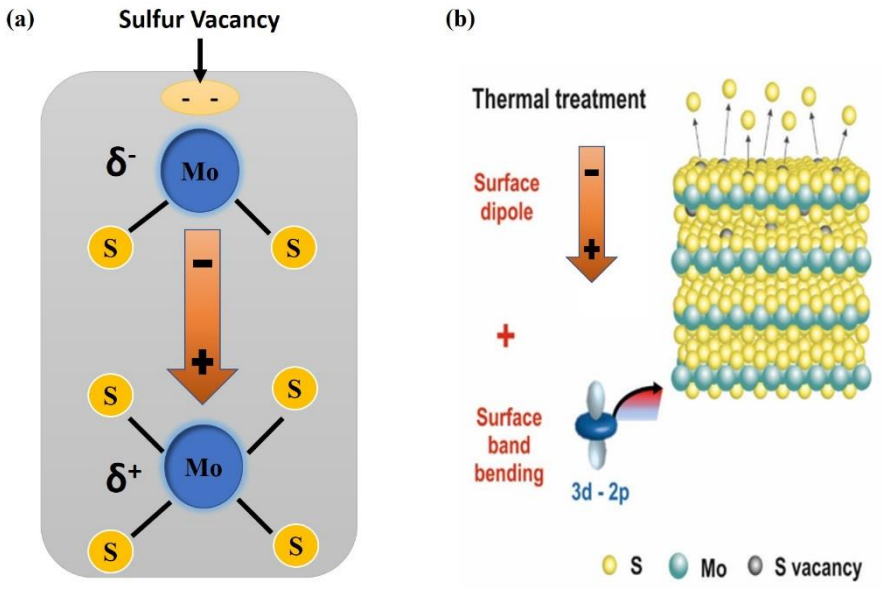


**Figure** 3-6 (a) Schematic illustration of the chemical environment of an individual sulfur vacancy. (b) The removal of sulfur atoms from the $MoS_2$ surface by UHV thermal treatment leads to the formation of a surface dipole and band bending.

To account for the modified electrostatic field, we assume an electrostatic model previously developed to elucidate work function changes due to molecule adsorption,[196] where the total change of the work function ($\Delta\phi_{tot}$) can be determined by the sum of independent contributions. In the present study, we attribute the total change of the work function after thermal treatment to the formation of an interface dipole $\Delta$Vint. dip (due to the net excess of negative charge localized on the topmost $MoS_2$ layer), in analogy to the adsorption of electron acceptor/donor molecules on semiconducting surfaces,[44,90] where net charge

transfer between donor/acceptor and substrate occurs. This interface dipole can be typically divided into a surface band bending ($\Delta\phi_{BB}$) contribution and the formation of a surface dipole moment ($\Delta\phi_{SD}$):

$$\Delta\phi tot = \Delta Vint.\ dip = \Delta\phi_{BB} + \Delta\phi_{SD} \quad (8)$$

For the samples TT300 and TT500, the downward shift observed for core levels is -0.10 and -0.25 eV (see **Table** 3-1), which is assumed to be equal to the surface band bending and is partially responsible for the work function increase of each sample, according to other studies where it has already been found that surface defects are one of the principal reasons for surface band bending.[81,86] In addition, the formation of a net dipole pointing toward the bulk (see **Figure** 3-6) implies an increase of the sample work function.[197,198] Therefore, we attribute the other part of the work function increase (0.10 and 0.23 eV, respectively) to the formation of a surface dipole moment. The simple model in **Figure** 3-6b summarizes the fact that both the formation of a surface dipole and surface band bending contribute to the increase of the work function and hence p-type behavior of thermally treated $MoS_2$.

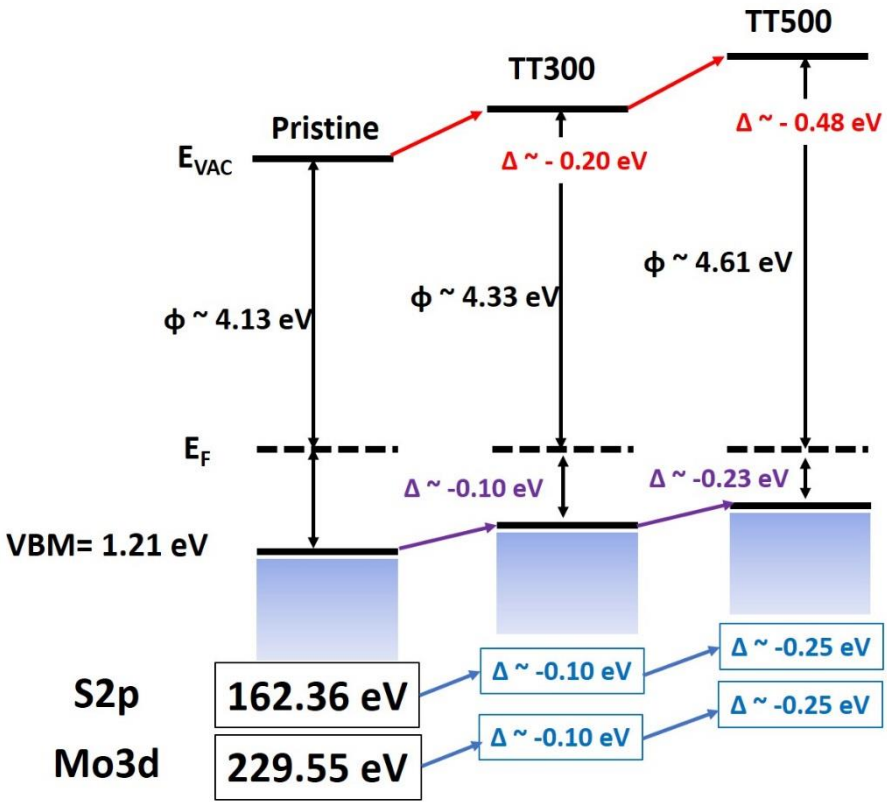


**Figure** 3-7 Band diagram evolution by introducing sulfur defect and the resulted energy level diagram of pristine and thermally treated samples.

**Figure** 3-7 schematically shows the interfacial energy level diagram of pristine and thermally treated $MoS_2$ surfaces, as derived from our UPS and XPS measurements. According to the above discussion, the total WF change, depicted in red, is the sum of surface band bending, depicted in cyan, and the surface dipole, depicted in violet.

### 3.5 Quantitative assessment of sulfur defects

As shown in previous section, UHV annealing introduces sulfur defects of different amount depending on the annealing temperature. The first evidence of the amount of sulfur loss has been obtained by evaluating the ratio of the S2p over the Mo3d signal collected by XPS.

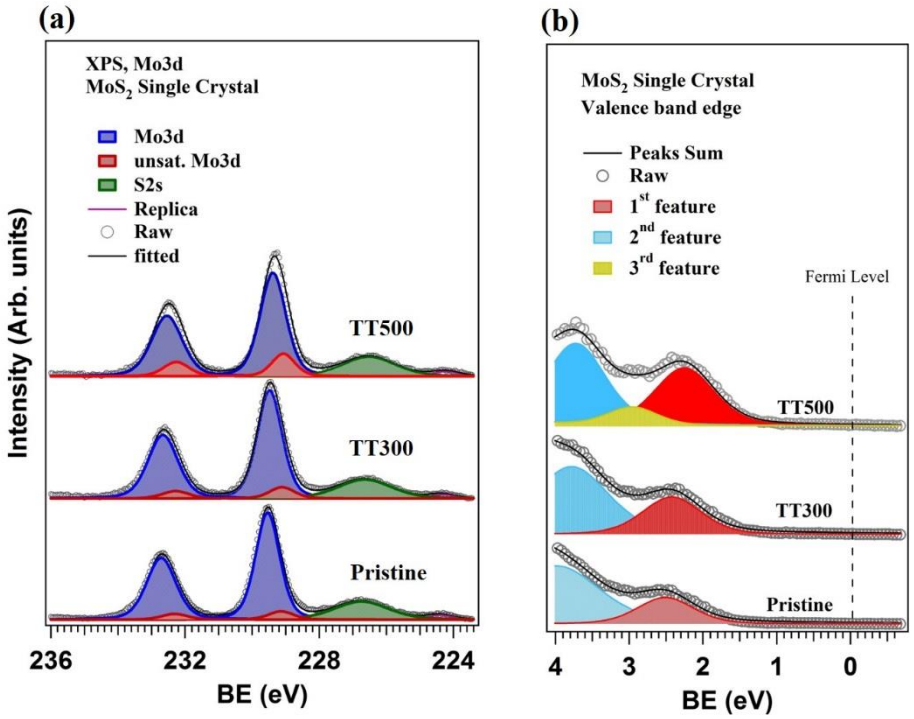


**Figure** 3-8 Evolution of defect-induced states after annealing: Fitted Mo3d-S2s and VB spectra obtained by XPS and UPS analysis (a) Fitted Mo 3d−S 2s core levels and (b) fitted valence band of pristine and thermally treated (TT = 300, 500 °C) $MoS_2$ single crystals.

However, the amount of introduced defects can also be discussed based on the Mo3d core level and valence band deconvolution. It was found that the Mo 3d line shape cannot be fitted by a single Mo 3d doublet (**Figure** 3-8a), unless another doublet located -0.3/-0.4 eV below the main doublet is added. The main doublet (in the following denoted by $Mo_{MoS2}$) corresponds to the six coordinated molybdenum atoms that are located at the center of the trigonal prismatic crystal structure of 2H-$MoS_2$. The appearance of the second doublet in Mo 3d spectra, here denoted by $Mo_v$, has already been reported in some other works.[63,76,199,200] It can be attributed to unsaturated molybdenum atoms, which are present in

the thermally treated samples mainly due to sulfur removal. Interestingly, sulfur vacancies are also present in the pristine sample in a low amount which arises from intrinsic defects in the as-received crystals.[81] By annealing the sample up to 500 °C, the full width at half maximum (FWHM) of the $Mo_{MoS2}$ peak increased from 0.85 to 0.91 eV, suggests the formation of defects and disorders in the crystal structure.[200]

The areas attributed to the doublet peak corresponding to unsaturated molybdenum in pristine and thermally treated samples at 300 and 500 °C are found to be (8.0 ± 0.4), (10.5± 0.5), and (19.6 ± 1.0) % of the total Mo 3d area. In other words, annealing the sample at 300 °C for 1 h increased the amount of defects by ∼30% relative to the pristine sample; this value becomes ∼143% for the sample annealed at 500 °C. It is important to note that the obtained values do not represent the absolute amount of surface defects but are an estimation of their relative increase induced by annealing.

Assuming that the relative increase of the structure in the valence band edge states is attributable to the higher amount of sulfur vacancies,[83,201] an increase of ∼33 and ∼139% in the area of the valence band edge states for the samples TT300 and TT500 is found (see **Figure** 3-8), thus in good agreement with the values found in Mo3d core level analysis.

## 3.6 Surface molecular interaction of MUPA with defective 2H-$MoS_2$: thiol functionalization

Surface functionalization with an 11-mercaptoundecylphosphonic acid (MUPA) (**Figure** 3-9a) was used to investigate the effect of sulfur vacancy compensation via a thiol anchoring group on the electronic structure of $MoS_2$. In particular, the functionalization was performed on pristine and thermally treated 2H-$MoS_2$ samples and the change in the electronic properties was investigated. It is expected that the thiol group (−SH) will react with a sulfur vacancy and the electron withdrawing end group (i.e., phosphonic acid) facilitates functionalization with the functionalizing molecule attached to the surface, over a local sulfur vacancy substitution, where only the $S^{2-}$ generated from the thiol group can be covalently bound to Mo centers.[182] (**Figure** 3-9b) Independent of the structure of the S vacancies present on the sample, e.g., mono, double, line, or clusters,[178–181] the chemical reactivity with a thiol group will be similar[202] and they can strongly bind the MUPA molecule.

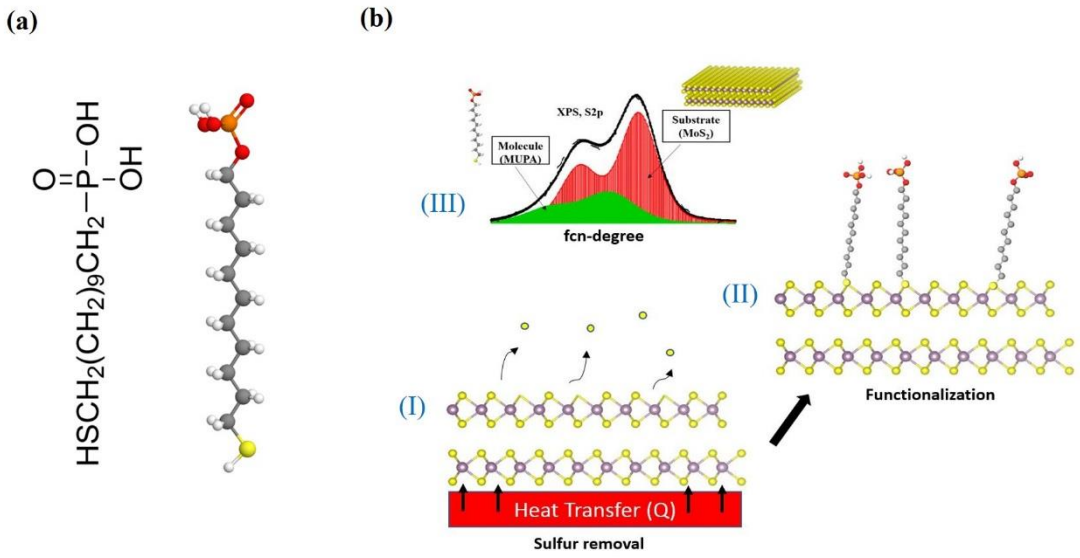


**Figure** 3-9 (a) MUPA chemical composition and Ball Stick model of the molecule and (b) Schematic illustration of functionalization process: (I) UHV annealing and introducing defects, (II) molecular functionalization and (III) XPS measurement, which evidence the presence of MUPA molecule on $MoS_2$,.

Furthermore, MUPA was chosen due to its negligible intrinsic dipole moment. Thus, any changes on the $MoS_2$ electronic structure can be mainly referred to binding effects. Besides this, the phosphonic acid end group provides a molecule fingerprint in the XPS spectra to evaluate the functionalization efficiency.

Concerning the functionalization process of (untreated) pristine and TT500 2H-$MoS_2$, a wet-chemical approach was used. The samples were immersed into a 1 mM ethanol solution of MUPA (purchased from Sigma-Aldrich) and kept for 24 h. Thermally treated $MoS_2$ samples were extracted from UHV and immediately immersed into a solution a 1 mM ethanol solution of MUPA (Sigma-Aldrich), to minimize atmosphere contamination surface. After 24 h, they were sonicated for 5 min in ethanol to remove weakly bound molecules, dried with nitrogen and inserted into the analysis chamber.

### 3.6.1 Assessment of interaction between organic thiol and 2H-$MoS_2$ substrate

**Figure** 3-10a shows the P 2p core levels of the untreated pristine sample (i.e., neither thermal treatment nor functionalization) and two functionalized samples, namely, functionalized pristine (without thermal treatment) and functionalized thermally treated (TT500) samples. Whereas the P 2p core level region of the untreated pristine sample reveals a negligible signal in the phosphorus energy region, the two functionalized samples exhibit a detectable P 2p peak stemming from the molecule.

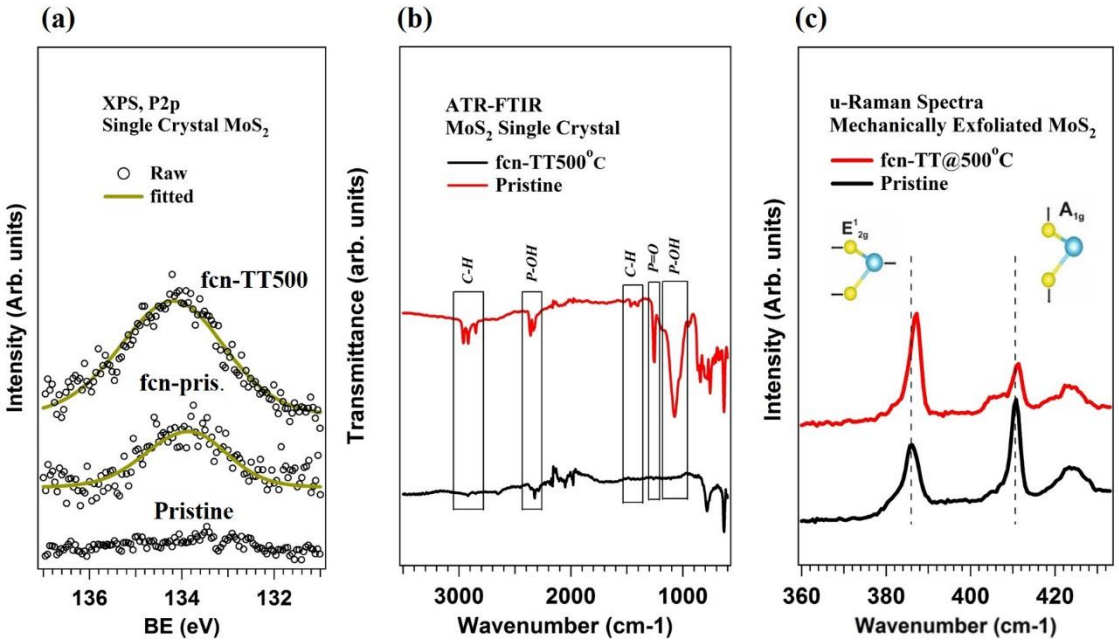


**Figure** 3-10 (a) P 2p core level of untreated pristine, functionalized pristine (fcn-pristine), and functionalized thermally treated (fcn- TT500) $MoS_2$ single crystal. (b) FT-IR spectra of pristine and functionalized (TT500) $MoS_2$ single crystal and (c) μ-Raman, showing 2.5 $cm^{-1}$ blue shift of the two main characteristic peaks after functionalization.

As can be seen, the intensity of the P 2p core level is higher for the functionalized + thermally treated sample than for the only functionalized pristine one, which is a clear indication of a higher number of molecules present on the thermally treated sample.

To further prove the presence of intact molecules on the surface, μ-Raman and FT-IR measurements were performed on the pristine and functionalized TT500 samples; see **Figure** 3-10b and c. The Raman spectra (**Figure** 3-10c) show the typical $E_{2g}{}^1$ and $A_{1g}$ vibrational modes which arise from in-plane opposite vibration of two sulfur atoms with respect to molybdenum and out-of-plane vibration of two sulfur atoms in opposite directions, respectively. Due to functionalization and the consequent interaction at the interface of molecule/substrate, a shift toward higher wavenumbers occurs in the Raman peaks. Similar observation has already been reported by Cho *et al.*[101] Moreover, an inversion in the peak ratio occurred, which is a clear indication of surface atomic modification. This is mainly because, the more restriction is imposed to atomic vibration in vertical direction due to the attachment of molecules with a certain molecular weight. The FT-IR spectrum obtained from functionalized $MoS_2$ (**Figure** 3-10b) is mainly dominated by the components of the phosphonic acid and the carbon chain of the molecule, which once more confirms the presence of MUPA molecules on the surface.

Since the samples were sonicated after the functionalization process to remove any unbounded molecules, we can assume that all the molecules detected on the surface strongly interact with the $MoS_2$ substrate.

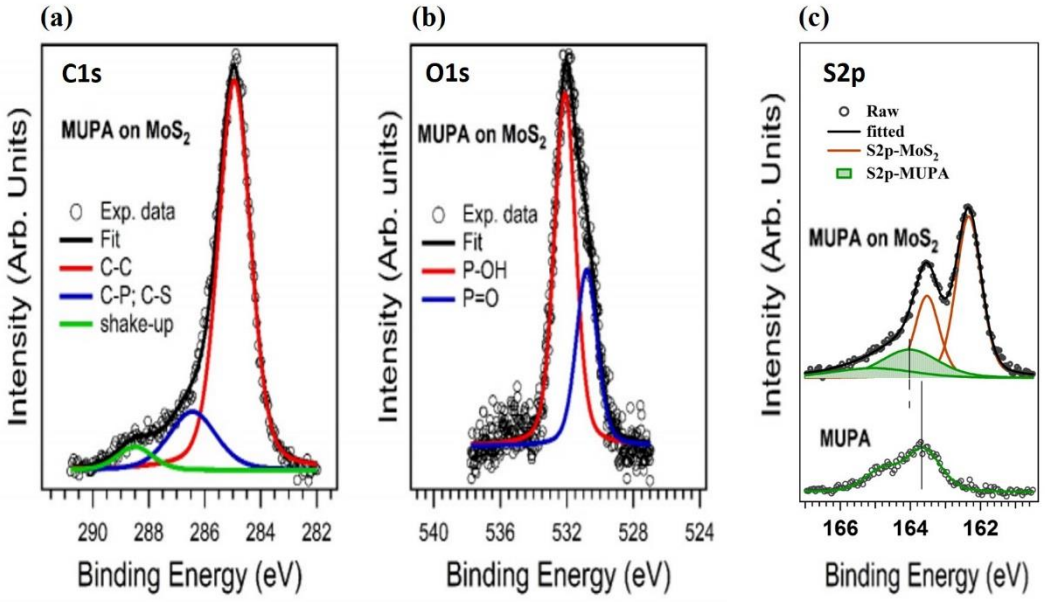


**Figure** 3-11 (a) C 1s and (b) O 1s core levels of thiol-functionalized (thermally treated) $MoS_2$ single crystal, indicating the presence of MUPA molecule on $MoS_2$. (c) S2p core level of the same sample (up), as well as the S2p core level of bulk MUPA (down).

The typical C 1s and O 1s core level spectra of the intact MUPA molecule chemisorbed on the thermally treated $MoS_2$ surface (TT500) are shown in **Figure** 3-11a-b, further confirming the presence of MUPA molecule on 2H-$MoS_2$. C1s shows typical C-C component at about 285 eV, while presence of C-S and C-P bonds are convolved in a single peak at 286.30eV. A further satellite is present at288.32eV and can be attributed to shake-up process, typical of organic molecules. O1s core level has two components, related to P-OH groups (at 532.15eV) and P=O bond (530.80eV). S2p core level of bulk MUPA and the MUPA on $MoS_2$ is given in **Figure** 3-11c. It can be seen that, the S2p doublet attributed to MUPA, experience a shift to higher binding energy (from 163.64eV to 164.10eV) when interacting with $MoS_2$, which is an indication of electronic environment change of sulfur atoms of MUPA, evidencing the strong interaction of the molecule with $MoS_2$.

### 3.6.2 Passivation of sulfur defects and recovery of surface electronic properties

Thiol treatment of defective $MoS_2$ has already been discussed in **Section** 1.4.2. Choi *et al.*,[84] has shown that, through thiol functionalization of defective $MoS_2$, the core levels shifts toward higher binding energy and ended up somewhere close to the BE position of the

untreated sample (see **Figure** 1-17), which is an indication of partial sulfur vacancies passivation. **Figure** 3-12a–c shows the Mo 3d and S 2p core levels and SECO spectra of the functionalized TT500 sample (fcn-TT500) in comparison with the untreated pristine and TT500 sample. It can be seen that, after attaching the MUPA molecule, the Mo 3d and S 2p core levels, completely shifted back to their initial position (relative to untreated $MoS_2$). Details are given in **Table** 3-2.

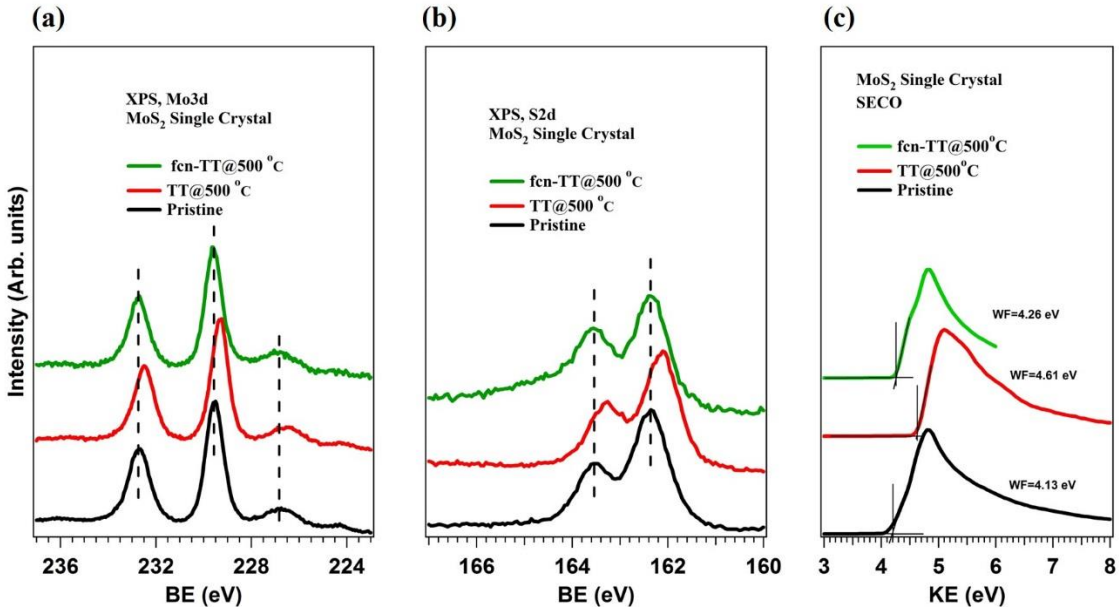


**Figure** 3-12 (a) Mo 3d and (b) S 2p core levels and (c) SECO of functionalized (fcn) sample after thermal treatment (TT = 500 °C) in comparison with pristine sample and thermal treatment only.

In addition, the work function is decreased and almost reaches its initial value (see **Figure** 3-12c). The backward shift of the core levels is an indication of passivation of the defects through filling the sulfur vacancies at the surface by the thiol group of the molecule. Hence, the surface charge is partially neutralized, and the corresponding surface dipole is much smaller than that in the thermally treated sample (see **Figure** 3-13a).

Furthermore, band bending effects are reversed, pointing to an almost complete compensation of the electric field at the surface. Such a backward shift of the Mo 3d and S 2p core levels implies a strong interaction between the molecule and the substrate, suggesting an effective filling of the surface vacancies.

The change of the electronic structure of 2H-$MoS_2$ after functionalization (i.e., sample fcn-TT500), leading to an almost complete recovery of the initial 2H-$MoS_2$ electronic structure, is summarized in the energy level diagram reported in **Figure** 3-13b. The 0.08 eV difference

in WF with respect to the TT500 surface, is probably related to a residual surface dipole due to few unfilled Sulphur vacancies.

**Table** 3-2 Binding Energy (BE), Valence Band Maximum (VBM), Work Function (WF), and S/Mo Ratio Changes after Functionalization by MUPA

| | **$Mo3d_{5/2}$ (ΔBE) [a]** | **$S2p_{3/2}$ (ΔBE) [a]** | **VBM (ΔBE) [a]** | **WF (ΔWF) [a]** | **S/Mo [2.0]** |
|---|---|---|---|---|---|
| **TT500** | 229.30 | 162.11 | 0.98 | 4.61 | 1.72 |
| **Fcn-TT500** | 229.55 (+0.25) | 162.36 (+0.25) | 1.21 (+0.23) | 4.21 (-0.40) | 1.89 |

[a] BE, ΔBE, and WF are expressed in eV

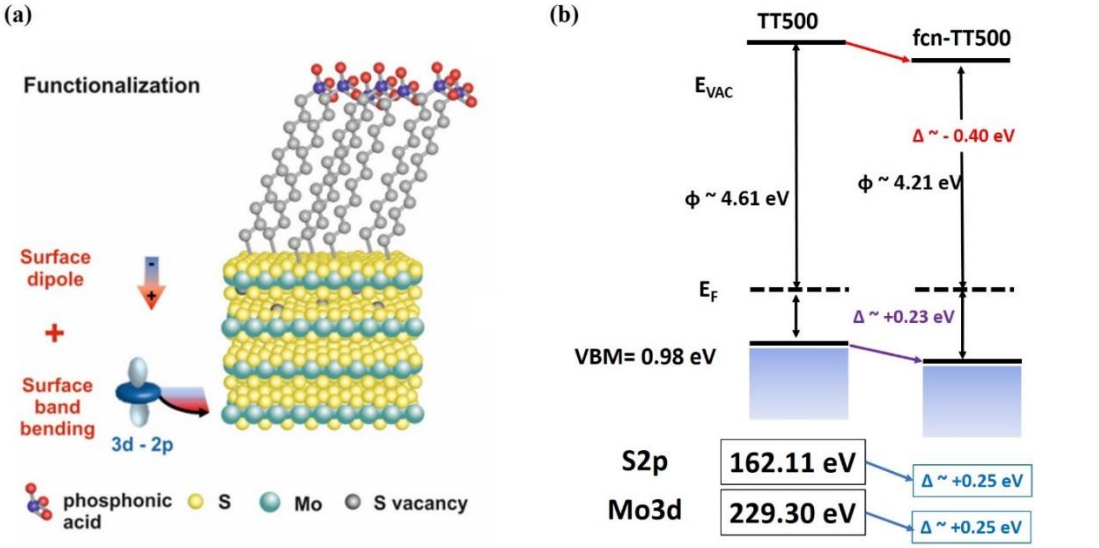


**Figure** 3-13 (a) Schematic illustration of the functionalization of thermally treated $MoS_2$. (b) Energy level diagram of thermally treated and functionalized samples.

**Figure** 3-14 shows the deconvolution of the (a) Mo 3d−S 2s and (b) S 2p core levels for the functionalized pristine and functionalized TT500 samples. For the sake of comparison, the core levels of the untreated pristine sample are also reported. The Mo 3d−S 2s core level region confirms the presence of a second S 2s peak (green in **Figure** 3-14a) that only appears in functionalized samples, and therefore, it is attributable to the molecule. The S 2s peak of the molecule is located at 227.97 eV, which is ~1.30 eV higher than the S 2s peak arising from the substrate. The S 2p core levels of the functionalized samples (**Figure** 3-14b) are comprised of two doublets that correspond to sulfur atoms of the molecule at ~164.0 eV and the 2H-$MoS_2$ substrate at ~162.35 eV.

Although surface functionalization was achieved by filling sulfur vacancies with thiol groups, the S 2p BE of surface-bound (i.e., reacted) MUPA lies ~1.65 eV above the S 2p

stemming from sulfur sites in the 2H-$MoS_2$ environment, which is due to the presence of the long alkyl chain and phosphonic acid group in the molecule.

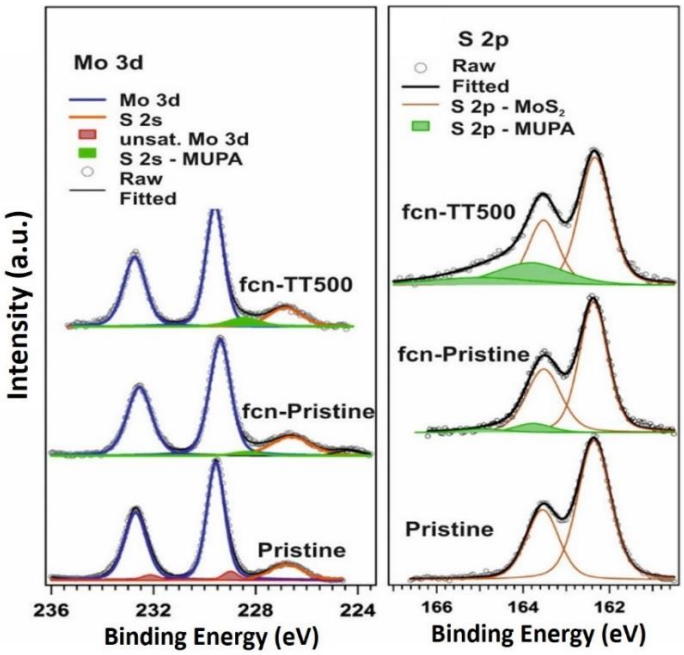


**Figure** 3-14 Fitted (a) Mo 3d−S 2s and (b) S 2p core levels of pristine, functionalized pristine, and functionalized thermally treated (TT500) $MoS_2$ single crystal, showing the increase in molecule-attributed states after functionalization.

### 3.6.3 Functionalization degree and surface coverage

The molecular surface coverage per surface area was calculated to estimate the functionalization efficiency. The approach is based on the fact that the photoelectrons from the substrate are exponentially attenuated by the organic layer.[203] Hereafter, we assume that the immersion of the samples in the molecule's solution followed by sonication yielded a monolayer of MUPA, which is uniformly distributed on the $MoS_2$ substrate. The signals from substrate are exponentially attenuated by the molecule monolayer; the formulation to calculate the MUPA surface coverage on $MoS_2$ has been adopted from Wang *et al.*[45]

Basically, the intensity of the signal from the MUPA is given by:

$$dI_{MUPA} = I_{O,MUPA}\exp(-t/\lambda_{MUPA}\cos\Theta)dt \quad (9)$$

$$I_{MUPA} = I_{O,MUPA}[1 - \exp(-d_{MUPA}/\lambda_{MUPA}\cos\Theta)] \quad (10)$$

$$I_{O,MUPA} = NI_{ph}\sigma_{MUPA}\lambda_{MUPA}T(E)\cos\Theta \quad (11)$$

Where, $d_{MUPA}$ denotes the thickness of the MUPA (**Figure** 3-15), $I_{O,MUPA}$ denotes the signal intensity of an infinitely thick film; N is the surface density of the MUPA; $I_{ph}$ is photon flux at the analysis position in photons.cm$^{-2}$.s$^{-1}$; $\sigma_{MUPA}$ is the photo-ionization cross section; $\lambda_{MUPA}$is the inelastic mean free path (IMPF); T(E) is the intensity/energy response function of the spectrometer; $\theta$ is the angle between surface and the MUPA chain, in this experiment we can assume to be 90$^{o}$.

The intensity of the XPS peaks from the underlying $MoS_2$ substrate is given by subtracting the attenuation of the MUPA:

$$I_{MoS2} = I_{O,MoS2}\left[\exp\left(-\frac{d_{MUPA}}{\lambda_{MoS2,MUPA}\cos\theta}\right)\right] \quad (12)$$

where, $I_{O,MoS2}$ denotes the signal intensity of an infinitely thick $MoS_2$ film; $\lambda_{MoS2,MUPA}$ denotes the electron Inelastic Mean Free Path (IMFP) of the $MoS_2$ in the MUPA.

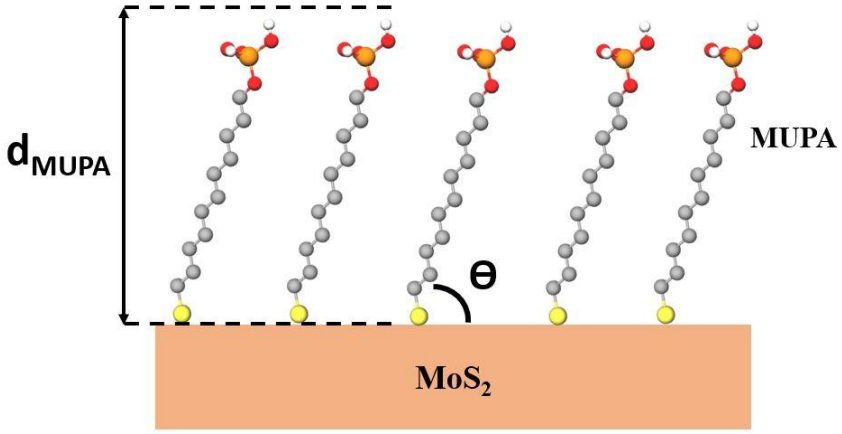


**Figure** 3-15 Schematic illustration of SAM of MUPA on $MoS_2$ substrate.

As a result, for the S 2p in **Figure** 3-14b, the intensity of the peak can be described as:

$$I_S = I_{O,S}\left[1 - \exp\left(-\frac{d_{MUPA}}{\lambda_{S,MUPA}\cos\theta}\right)\right] \quad (13)$$

Where $d_{MUPA}$ is the thickness of the MUPA monolayer, corresponding to the projection along z axis; $\lambda_{S,MUPA}$is the IMFP of the S 2p at the kinetic energy of about 1090 eV.

For the Mo3d, in which the intensity is attenuated by MUPA layer, the measured XPS peak intensity can be described as:

$$I_{Mo} = I_{O,Mo}\left[\exp\left(-\frac{d_{MUPA}}{\lambda_{Mo,MUPA}\cos\theta}\right)\right] \quad (14)$$

Where $\lambda_{Mo,MUPA}$ is the electron IMFP of the Mo3d at the kinetic energy of about 1020 eV. The ratio of $I_S$ to $I_{Mo}$ would be as following:

$$\frac{I_S}{I_{Mo}} = \frac{N_S \sigma_S \lambda_{S,MUPA}}{N_{Mo} \sigma_{Mo} \lambda_{Mo,MUPA}} \frac{1-\exp\left(-\frac{d_{MUPA}}{\lambda_{S,MUPA}\cos\theta}\right)}{\exp\left(-\frac{d_{MUPA}}{\lambda_{S,MUPA}\cos\theta}\right)} \quad (15)$$

where, $N_{Mo}$ is the density of the Mo atoms in $MoS_2$. The surface coverage of the MUPA molecule on $MoS_2$ substrates given by $N_S \times d_{MUPA}$.

Calculation of the surface coverage was done assuming a density for the 2H-$MoS_2$ single crystal and the MUPA film of 5.06 and 1.4 g/cm$^3$, respectively. The surface coverage for the functionalized pristine and functionalized TT500 samples is found to be ~0.87 and ~2.1 mol/nm$^2$, respectively. According to these values, the number of molecules on the thermally treated sample is about 3 times higher than the number of molecules present on the untreated sample. Hence, the sulfur defects introduced on the surface by thermal treatment facilitate the thiol molecules to be attached on the surface, which yielded a 3 times higher functionalization efficiency relative to the untreated functionalized substrate.

Such effective functionalization for the TT500 sample leads to an almost complete clearance of the surface band bending, as evidenced in **Figure** 3-12a-b by the backward shift of the substrate core level. Moreover, the almost negligible intrinsic dipole moment of the MUPA molecule, together with the compensation of the negative charge at the surface, leads to a substantial annihilation of the surface dipole that allows for an almost complete recovery of the substrate's initial work function **Figure** 3-12c. This process can be explained and justified by an effective compensation of charges: the excess of negative charges localized on the Mo centers, which is initially generated by the sulfur vacancies after thermal annealing, is compensated by filling the sulfur vacancies with the thiol groups of the functionalizing molecule.

### 3.7 Conclusions

Since sulfur vacancies play a crucial role in determining the electronic structure of $MoS_2$ by changing the surface reactivity for any subsequent molecular functionalization, a fundamental study to investigate the formation of such defects and their role in the surface electronic structure was performed. For this purpose, a pristine 2H-$MoS_2$ single crystal was thermally treated at 300 and 500 °C (in UHV) and compared with the pristine state. The

amount of sulfur vacancies, as estimated via XPS, increased by about ~30 and ~140%, respectively, in comparison to the vacancies natively present on pristine 2H-$MoS_2$.

The subsequent excess of negative charge on the Mo centers at the surface leads (on 2H-$MoS_2$ thermally treated at 500 °C) to the formation of a band bending of ~0.25 eV and a surface dipole that strongly modify the electric field at the surface allowing a WF increase of ~0.48 eV . The possibility to fill the vacancies and restore the original electronic structure of the 2H-$MoS_2$ surface was tested by means of molecular functionalization of the thermally treated surface with a thiol derived molecule, having a phosphonic acid group at one end.

The surface functionalization resulted in the formation of a homogeneous and densely packed layer of MUPA (i.e., surface density of ~2.1 mol/$nm^2$) that filled almost completely the sulfur vacancy sites generated by thermal treatment. The excess of negative charge on the Mo centers was then compensated by the thiol (−SH) groups of the molecule, bringing back the surface to the almost neutral state. Consequently, the surface band bending is completely recovered, and the Mo 3d and S 2p core levels move back to the original values as in the pristine 2H-$MoS_2$. The WF of the MUPA functionalized sample almost recovers the initial value with an offset of only 0.08 eV with respect to the pristine surface. This is attributable to a small surface dipole, related to the presence of only a few remaining sulfur vacancy sites.

The present study highlights how the surface treatment of 2H-$MoS_2$ and specifically the generation of sulfur vacancies at the surface can strongly affect the electronic structure of the first interface and consequently its reactivity. Moreover, via an efficient molecular functionalization, we demonstrated how the sulfur vacancies can be filled via a thiol-derived molecule, restoring the initial properties of the 2H-$MoS_2$ surface. The rationalization of the change in the electronic structure of 2H-$MoS_2$ after thermal treatment and molecular functionalization paves the way for a more efficient and effective engineering of both the 2H-$MoS_2$ surface and chemically engineered molecules with specific functionalities that will affect 2H-$MoS_2$ based device performances. Moreover, despite the many attempts to study the density of defects in TMDCs materials by different microscopy and spectroscopy techniques, for the first time a feasible experimental approach based on valence band edge analysis has been proposed to approximate the relative increase in the defect density. One of the main advantages of this approach is the relatively large area, which can be probed with UPS spotlight that collects the photoelectrons from an area in the range of few hundreds of

micrometers, which makes the results more reliable. However, further works must be done to obtain an accurate approach for more quantitative analysis of the defects based on photoemission spectroscopy.

The results presented here, have been published in the scientific paper:

**A. Ghiami**, M. Timpel, M. V. Nardi, A. Chiappini, P. Nozar, A. Quaranta and R. Verucchi, "Unravelling work function contribution and their engineering in 2H-$MoS_2$ single crystal discovered by molecular probe interaction", **Journal of Physical Chemistry C 124**, 6732 (2020)

# Chapter 4

# Synthesis of quasi-2D $MoS_2$ film

## 4.1 Introduction

Since the most intriguing optical and electrical properties of $MoS_2$ appears when the material is in its 2D form, methods for scalable synthesis of ultra-thin film of $MoS_2$ with high quality are highly desirable and must be developed.

Despite the many achievements have been obtained in deposition of 2D-$MoS_2$ via different techniques, a novel deposition process is demanded since any of the formerly discussed techniques (in **Section** 1.5) are suffering from certain limitations. For example, chemical vapor deposition (CVD) has been successfully applied for growth of recently emerged 2D-TMDs, but this technique shows some drawbacks such as high growth temperature up to 1000 °C, time consuming processes and use of toxic precursors.[149]

As an alternative, pulsed laser deposition (PLD) has also been widely used to synthesize $MoS_2$ thin films. PLD is based on ablation induced by a pulsed-laser beam when focused on the surface of target material. Despite several advantages such as reproduction of target stoichiometry, PLD is also suffering some limitations. For example, when laser strikes a target, the interaction of electromagnetic wave with the surface results in a series of cascade process such as target material ionization, electron oscillation, heat generation and the consequent ablation processes that still not well understood and make it rather complicated to find the correct parameters to grow different material.[204] On the other hand, the elevated cost of an excimer laser and the energy consumption of the laser source cannot be ignored when summed up with the low conversion efficiency of the process in which only about 1-2% of each laser shots are transformed to heat and results in ablation. Moreover, dependency of PLD process to the optical properties of material also restricts the range of materials can be deposited by this technique. As an instance, $SiO_2$ with ~10 eV optical bandgap is transparent to 248 nm of Kr-F excimer laser radiation which is typically utilized in PLD. Last but not least, PLD process is often accompanied with "splashing effect", which involves the production of microparticles between 0.1 and 10 μm, which reduces the quality of

deposited film.[205,206] For more detailed information on the achievements and the limitations of different approaches for synthesis of 2D-TMDs materials refer to **section** 1.5.

In this work we used a novel technique, so called Ionized Jet Deposition (IJD) to synthesize quasi-2D $MoS_2$ film with outstanding optical and electronic properties. The technique is similar to pulsed electron deposition (PED) and benefits from all the advantageous of this technique, e.g. the ablation process is induced by an electron beam with high voltage/high current pulses. In the reviews carried out by Mazzer *et al.*,[207] and Nistor *et al.*,[208] the widespread applications of PED technique to deposit thin films has been presented. PED, in addition to its relatively lower cost than PLD, brings about new advantages like independency of the technique to optical properties, i.e. refractive index, of the materials which facilitate the deposition of a wider range of materials with high optical and electronic bandgaps. This possibility relies on the fact that the kinetic energy of the electrons striking the target, regardless of the material optical properties, can be easily absorbed on the surface and results in material ablation. Thanks to this feature, materials which are transparent or highly reflective to laser light can be processed. Moreover, it has been found that the electron beam in comparison to laser light with the same power density shows higher efficiency and hence, results in a larger amount of material ablation.[209]

In the following sections, the advantages of IJD over PED technique will be discussed. In this work, IJD has been used for the first time to grow $MoS_2$ thin film. The morphological, structural, chemical, optical and physical properties of IJD-$MoS_2$ with special focus on surface electronic properties of the material will be thoroughly discussed.

### 4.2 Ionized Jet Deposition (IJD)

IJD is an evolution of the PED approach, developed with the aim to solve its weaknesses. These techniques work in high vacuum environment, so all processes occur inside a vacuum chamber and not an Ultra High Vacuum chamber, as in case of PLD. Briefly, a PED source is composed of a hollow cathode where the electron extraction from a carrier gas occurs by means of a pulsed negative discharge, often triggered by a small power pre-discharge to facilitate the plasma formation. Electrons are accelerated towards the target at ground potential (the anode) by passing through a dielectric tube, confining the electron beam till the target surface. The pulse intensity and frequency are regulated mainly by gas pressure and HV power supply parameters (voltage, discharge capacity, frequency). Main drawbacks in PED process are related to presence of the dielectric tube. At high frequencies it suffers

massive overheating, while after few hundreds of working hours, carbonization processes occur and both processes inhibit electron transport. Replacement of the dielectric tube is often necessary making PED hardly scalable towards industrial exploitation. IJD has been patented by Skocdopolova in 2013.[214]

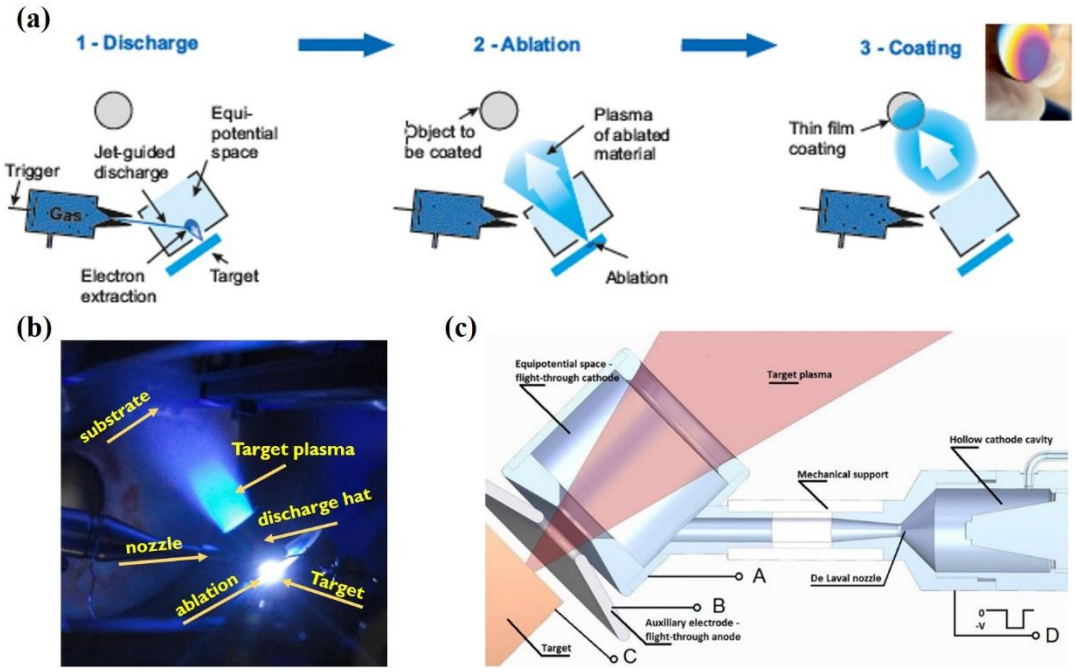


**Figure** 4-1 (a) IJD deposition steps, (b) IJD nozzle holding plasma plume, (c) The main components of the IJD deposition source; A, B, C, and D mark the electrical connection points to the high voltage source. Adapted from [211].

Differently from PED (see **Figure** 4-1a),[211] the cathode (cylinder shape with opening in both bases) is close to the target and receives a continuous gas flow, a supersonic molecular beam (generated by a Laval nozzle) that can be ionized by a trigger discharge to create the necessary plasma density to ignite the main hollow cathode discharge (**Figure** 4-1c).[215] Electron extraction is highly efficient and all generated particles can hit the target surface, leading to an efficient material ablation. The generated plasma carrying the ablated material, becomes densified on the substrate facing the target material (**Figure** 4-1b).[209,214] This technique overtakes the main drawback of PED, i.e. the need for periodically substituting the dielectric tube confining the generated electron beam. This also leads to superior pulsed electron beam power and robustness on the target surface.[214] Moreover, one of the main advantages of IJD, which makes it more industrially favorable relative to PLD, is the higher energy conversion efficiency of the process, which is in the range of 82% to 88%. The higher efficiency also leads to a more optimized (and optimizable) ablation process, which makes it more suitable for deposition of multicomponent materials such as photovoltaic

semiconductors or superconducting oxides, crystalline films and deposition on any kind of substrate including thermosensitive materials.[209]

IJD electron source is able to generate ultra-short electric discharges of 300-600 ns, 1 kA using a high voltage pulse up to 25 kV and a duration as short as 1µs.[214] Under certain condition which can be reached by specific deposition parameters, the target material stoichiometry can be preserved in the deposited thin film. The lateral extension of the deposited film has typically a diameter of 10cm, thus enabling coverage of large substrate area.

The IJD apparatus utilized in this thesis work is shown in **Figure** 4-2. It is a high vacuum chamber with a pumping system comprised of a turbomolecular and a primary pump. Two rotors shown in the top and bottom of the main chamber are responsible for rotating the target material and the substrate to guarantee a homogenous deposition during ablation. The substrate holder is not heatable. On the right-hand side of the picture, the electron gun is shown, which was dissembled from the main chamber for maintenance purposes.

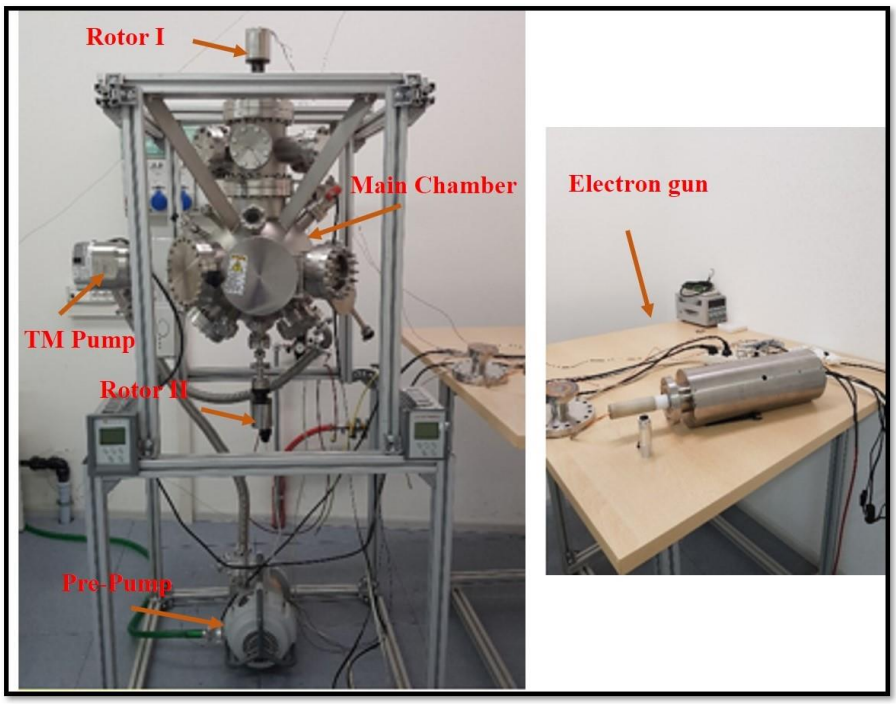


**Figure** 4-2 Components of IJD apparatus available at IMEM-CNR institute used in this thesis work.

The IJD source, in principle, could be mounted also on an UHV chamber, thanks to the presence of CF type flanges. To this end, a system for target replacement must be specifically designed as now this is possible through a quick access flange with viton sealing.

To date, IJD has been utilized to prepare ceramic coatings with superior tribological, mechanical and chemical properties,[210,211] deposition of thin films applicable in photovoltaic,[207,212] as well as deposition of polymer material.[213] To the best of our knowledge, no works has been reported to synthesis any materials of TMDCs class. For the first time, we will describe the successful deposition of quasi-2D $MoS_2$ layers on Si (001) with native oxide and metallic platinum substrates at room temperature by IJD technique.

### 4.3 Experimental procedure

Commercial $MoS_2$ pellet (Stanford Advanced Materials, Ø = 5 cm, thickness = 0.5 cm) of 99.95% purity has been used as the target material. Si (001) with native oxide and Pt (50 nm)-on-Si (see Ref. [216] for details of substrate preparation) thin film have been used as substrates for thin film deposition. These are the very first experiments of TMDC deposition by IJD technique, so it has been necessary to solve several feasibility issues concerning growth process. For this reasons, non-crystalline substrates have been chosen, e.g. instead of sapphire, as main goals were focused on $MoS_2$ synthesis rather than epitaxy or ordered growth (also considering it is not possible, in our growth chamber, to heat substrate during deposition). Substrates were cut into pieces with dimension of 1 cm×1 cm. Substrates were facing the target in the deposition chamber and the target to substrate distance was 15 cm. To improve material consumption and film uniformity, both target and substrate kept rotating in opposite direction during deposition process. The base pressure in the deposition chamber was $5\times10^{-6}$ mbar, which increased up to around $4\times10^{-3}$ mbar after plasma formation. All growths have been carried out with substrate at room temperature.

IJD process have different parameters, which play a significant role on the quality of the final product. Discharge (acceleration) voltage and deposition frequency are among the most important one. Thus, in order to find the optimal process parameters, for IJD deposition on silicon template, we used electric pulses at three different acceleration voltages, 12, 15 and 18 kV, with 1 μs duration and two different deposition frequency, namely, 150 and 250 Hz. However, we found that 250 Hz often induces increased temperature on target material, as evidenced by a deep red color detectable on the target during deposition. So, we decided to use only 150 Hz frequency. The optimal process parameters found in deposition on Si substrate, were applied in the deposition on Pt substrate, which were 150 Hz and 15 kV for deposition frequency and acceleration voltage, respectively. The transport gas leading to the discharge was pure Argon (N6). The distance between gun hat (smaller bottom opening of

the hollow cylinder) and the target was set to about 1 cm, while substrate was positioned about 12-13 cm from the top of the hollow cylinder.

Several IJD-$MoS_2$ films have been prepared on different substrates. A post deposition annealing treatment in UHV, at different temperatures was performed on several films. To obtain a comprehensive understanding on the chemical, vibrational, physical and surface electronic properties of the IJD-$MoS_2$ thin films and also the role of post annealing, a variety of characterization techniques have been used such as XPS and UPS for chemical/electronic properties, μ-Raman and XRD to evaluate crystallinity, SEM and AFM for surface morphology. Regarding the samples deposited on Pt substrate which have been prepared by adopting a fully optimized process, EELS, STS and PL measurements were carried in addition to previously cited analysis. Finally, to further prove the electrical performance and the versatile applicability of the IJD-$MoS_2$ thin film for electronic components, a resistive random memory (ReRAM) device based on IJD-$MoS_2$ has been realized.

More detailed information on the characterization tools and the applied parameters are given in **Chapter** 2.

### 4.4 IJD deposition of $MoS_2$ on Silicon substrate

The growth of $MoS_2$ ultra-thin layer on Si substrate has been studied as first test case of IJD deposition. The advantages of $MoS_2$ deposition on a semiconductor material like Si pave the way for obtaining a semiconductor-semiconductor heterojunction which can be applied for a variety of interesting purposes, such as developing highly efficient light sensors,[217,218] and photovoltaic devices.[219]

IJD-$MoS_2$ thin film has been prepared by 15 kV acceleration voltage (the deposition time is 1 h in all cases, unless it is mentioned). The XPS wide range spectrum in **Figure** 4-3a confirms the presence of molybdenum and sulfur on the as-deposited thin film, as well as Silicon, $SiO_2$ (due to the substrate) with its oxygen counterpart and carbon related to contaminations during the growth process and/or after air exposure.

Deconvolved spectra are shown in **Figure** 4-3b-c. S2p core level is characterized by a 1/2-3/2 doublet (due to spin orbit coupling), but in our case two doublets are present. Also, Mo3d core level shows a 3/2-5/2 doublet, as expected for $MoS_2$ (see **Chapter** 3). In the as-deposited sample, the $Mo3d_{5/2}$ and $S2p_{3/2}$ are located at binding energies (BEs) of 228.99 and 161.86 eV with FWHM of 1.41 and 1.52 eV, respectively. If compared to values for

single crystal $MoS_2$, there is a significant shift towards lower BEs of about 0.55eV for both Mo3d and S2p core levels, and an increase in FWHM of about 0.56eV for $Mo3d_{5/2}$ peak, the latter could be an indication of the presence of a certain degree of disorder in the IJD as-deposited film. Further evidences come from the presence of a second S2p core level doublet, located at higher binding energy at 163.08 eV ($S2p_{3/2}$), which can be attributed to unbonded, free elemental sulfur in the as-deposited IJD-$MoS_2$. The free sulfur also appears in the Mo3d-S2s core level (**Figure** 4-3b), leading to local enlargement in the line shape at 227.25 eV.

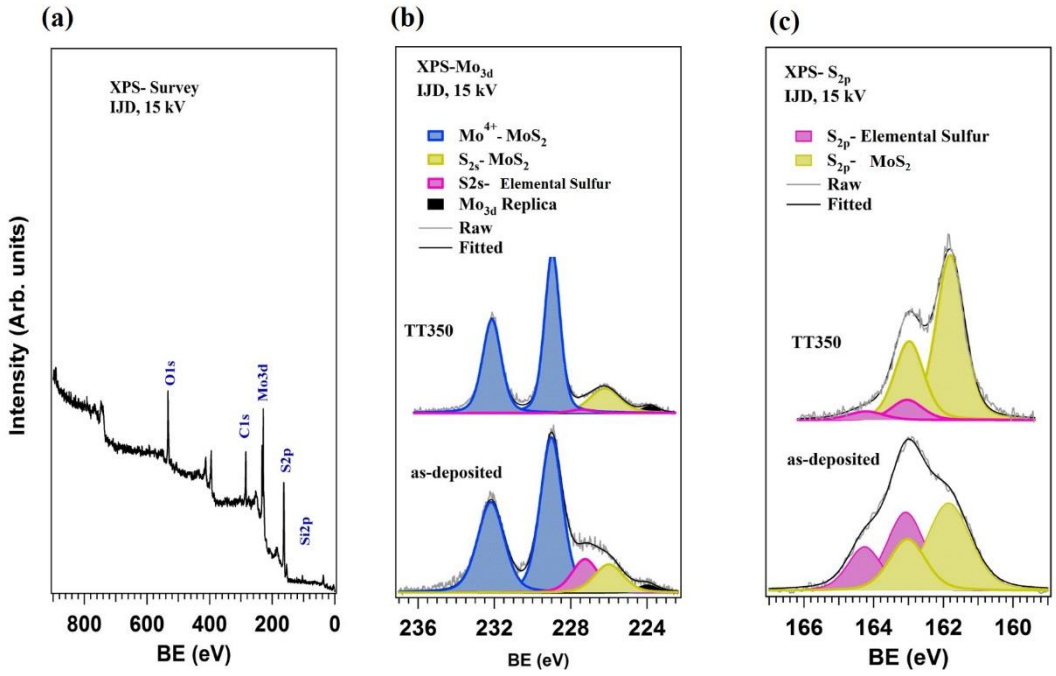


**Figure** 4-3 IJD-$MoS_2$ thin film deposited by 15 kV acceleration voltage, (a) survey spectra from as grown film, fitted (b) Mo3d and (c) S2p core levels from as grown and thermal treated at 350°C.

As stated previously, the Mo3d and S2p core levels showed considerable differences in BE with respect to the typical $MoS_2$ crystal (see **Chapter** 3). However, from a chemical point of view, the material is $MoS_2$, as can be inferred from the energy distance between $Mo3d_{5/2}$ and $S2p_{3/2}$, which is about 67.16 eV, the same value found for 2H-$MoS_2$, 67.19eV. Thus, we deposited at room temperature by IJD a $MoS_2$ thin film, having an excess of sulfur and probably a disordered structure.

In order to reduce the presence of elemental sulfur and possibly improve the crystal quality of $MoS_2$, we performed several thermal treatments in UHV at 190, 280 and 350 $^oC$ for 1 h, analyzing with in-situ XPS/UPS after each annealing (**Figure** 4-4). It is worth noting that the absence of any heating system in the IJD deposition chamber requires external thermal treatments, when they are necessary.

As depicted in **Figure** 4-4 b, by increasing the annealing temperature, the high BE side shoulder of the S2p core level gradually decreases, which is an indication of sequential free sulfur elimination. At the maximum temperature, as shown in the deconvoluted S2p core level (**Figure** 4-5c), a small amount of free sulfur is still present, suggesting that annealing at 350 $^{o}$C for 1 h does not completely remove the free sulfur. Similar results can be found for Mo3d analysis, as shown in **Figure** 4-4a. At increasing annealing temperature, the intensity of the broad feature around 287 eV decreases, which is a further indication of free sulfur gradual elimination. Furthermore, the FWHM of $Mo3d_{5/2}/S2p_{3/2}$ found to be 1.41/1.52, 1.33/1.44, 1.30/1.35 and 1.02/1.01 eV for, as-deposited, TT190, TT280 and TT350 samples, respectively. The energy difference for the two core levels is always about 67.16 eV, confirming presence of $MoS_2$ also after thermal treatments. As can be understood from the decreasing trend of FWHM values, by increasing the annealing temperature, the initial disorder of the film structure is (probably) gradually lost.

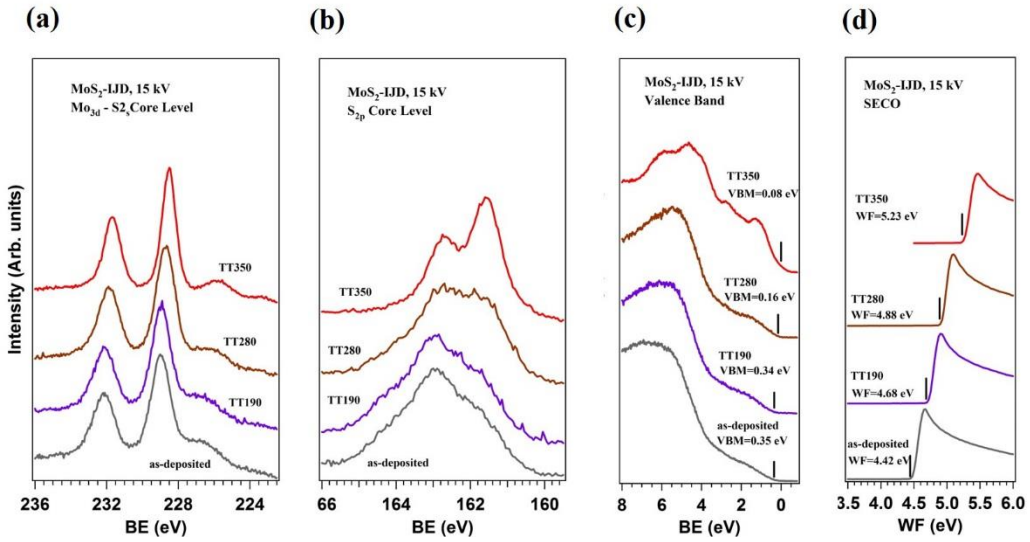


**Figure** 4-4 Thermal treatments of IJD-$MoS_2$ deposited at 15 kV acceleration voltage. Evolution of (a) Mo3d, (b) S2p, (c) valence band and (d) SECO.

The stoichiometry calculation of the as deposited and annealed samples has been evaluated. Considering the total amount of sulfur species, the S/Mo ratio found to be 3.81, 3.62, 2.88 and 2.39 for as-deposited, TT190, TT280 and TT350 samples, respectively (**Table** 4-1). The values for single crystal $MoS_2$, which were reported in **Chapter** 3 are also presented for the sake of comparison. The gradual decrease of the S/Mo ratio further evidences an increasing trend of Sulphur loss with the annealing temperature. Another evidence of the chemical quality of our IJD $MoS_2$ films comes from the evaluation of the S/Mo disregarding the small amount of free (elemental) sulfur (see **Figure** 4-3c). As can be seen in **Table** 4-1, for as

deposited, TT190, TT280 and TT350 we found 2.11, 1.98, 1.95, 2.14, that are in good agreement (within the typical errors for XPS analysis) with nominal expected one. This means annealing remove free sulfur and indeed improve film chemical structure, with less dangling bond, unreacted species, as previously evidenced, but already in as deposited film we are dealing with the $MoS_2$.

**Figure** 4-4c-d shows the valence band and SECO spectra of the as-deposited and annealed counterparts. By increasing the annealing temperature, the VBM and the WF shows a descending and an ascending trend, respectively. The increase of the WF is an indication of more p-type behavior of the material. Furthermore, similar to VBM, the S2p and Mo3d line shape also show a gradual downward shift by increasing the annealing temperature, which is consistent with the increasing trend of WF, in analogy to our former findings described in **Chapter** 3. The energy positions of the core levels, WF and VBM of the as-deposited and annealed samples are summarized in **Table** 4-1.

**Table** 4-1 Binding energy, FWHM, WF and S/Mo ratio of single crystal and IJD-$MoS_2$ deposited at 15 kV

| | **BE (eV)** | | **FWHM** | | **VBM (eV)** | **WF (eV)** | **S/Mo[a] [2.0]** | **S/Mo[b] [2.0]** |
|---|---|---|---|---|---|---|---|---|
| | ***Mo3d*** | ***S2p*** | ***Mo3d*** | ***S2p*** | | | | |
| **Single Crystal** | 229.55 | 162.36 | 0.85 | 0.91 | 1.21 | 4.13 | 1.92 | |
| **as-deposited** | 228.99 | 161.86 | 1.41 | 1.52 | 0.35 | 4.42 | 3.81 | 2.11 |
| **TT190** | 228.96 | 161.81 | 1.33 | 1.44 | 0.34 | 4.68 | 3.62 | 1.98 |
| **TT280** | 228.72 | 161.54 | 1.30 | 1.35 | 0.16 | 4.88 | 2.88 | 1.95 |
| **TT350** | 228.62 | 161.45 | 1.02 | 1.01 | 0.08 | 5.23 | 2.39 | 2.14 |

[a] all sulfur species has been taken into account
[b] only the sulfur specie attributed to $MoS_2$ structure have been taken into account

These results show a difficulty in removing the elemental sulfur from the deposited film, also at high temperature. However, from a chemical point of view, the material is $MoS_2$, as can be seen also from the energy distance of about 67.16 between $Mo3d_{5/2}$ and $S2p_{3/2}$. Concerning valence band, lineshape for TT350 film is very similar to what found for 500°C thermal treated 2H-$MoS_2$, even if in that case we found sulfur deficiency and evidence of defect formations (see Chapter 3). In our IJD film there is an excess of sulfur, WF has larger values and VBM is very close to Fermi level, so the material has significant differences from a $MoS_2$ single crystal.

To better identify the role of the electron energy in the IJD deposition process, we investigated other two acceleration voltages, 18 and 12 kV. It is noteworthy that acceleration voltages lower than 12 kV were not able to induce a reliable ablation process, thus we can consider 12 kV as a sort of energy threshold for $MoS_2$ IJD deposition.

Concerning the 18kV deposition, it has been observed an irregular plasma arising during IJD deposition, with the target reaching high temperatures as evidenced also by dark red color. Probably the deposited energy by the pulsed electron beam led a significant massive overheating, inducing sublimation processes and not only ablation, whose efficiency is then reduced. Nevertheless, we deposited an IJD-$MoS_2$ thin film at 18 kV acceleration voltage, annealed in UHV at 380 $^oC$ for 1 hour. The analyzed spectra of Mo3d- S2s, S2p and the valence band are given in **Figure** 4-5.

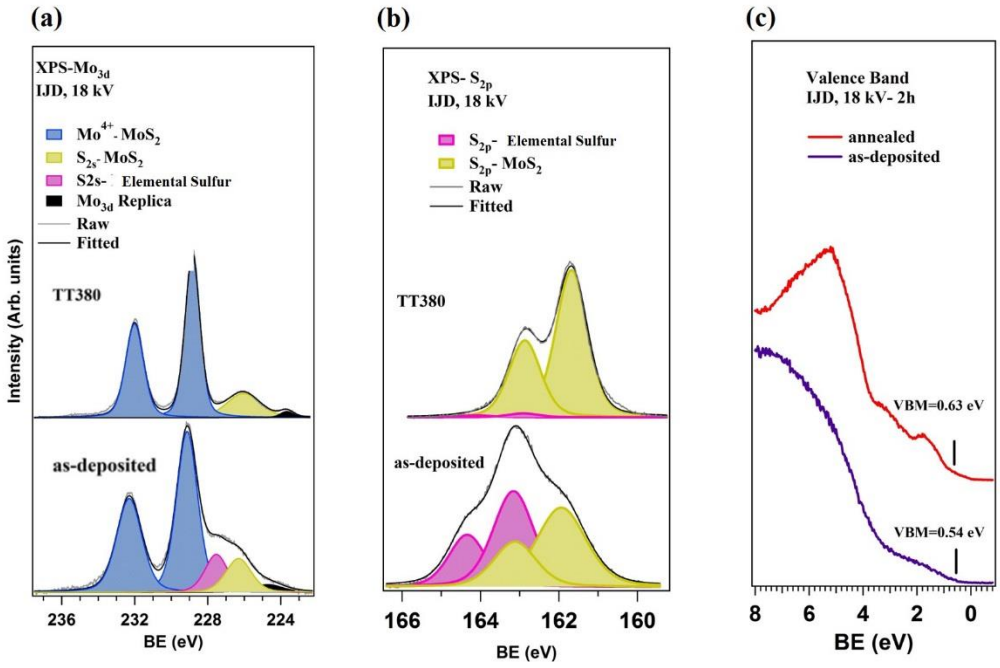


**Figure** 4-5 IJD-$MoS_2$ thin film deposited at 18 kV acceleration voltage; fitted (a) Mo3d-S2s and (b) S2p core levels and (c) valence band.

The energy positions of $Mo3d_{5/2}$ and $S2p_{3/2}$ found to be 229.09 eV and 161.94 eV, respectively, which have been shifted to the lower binding energy by annealing; the final position of the core levels were 228.78 eV and 161.63 eV, respectively. The energy difference between the two core levels is always 67.15 eV, thus typical of $MoS_2$. Moreover, the FWHM of the $Mo3d_{5/2}$ and $S2p_{3/2}$ core levels in the as-deposited sample found to be 1.46 and 1.57, which have been reduced to 1.06 and 1.08, respectively. The energy positions, FWHM, stoichiometry is summarized in **Table** 4-2. The VBM did not show any meaningful

shift after annealing, but still they are so closer to the Fermi level compared to the single crystal $MoS_2$, which is an indication of more p-type characteristic of the IJD-$MoS_2$. For these films, evaluation of WF resulted to be highly problematic, with not well defined SECO so no values are reported. Such a strange evidence will be discussed later.

**Table** 4-2 Binding energy, FWHM and S/Mo ratio of IJD-$MoS_2$ deposited at 18 kV

| | **BE (eV)** | | **FWHM** | | **VBM (eV)** | **S/Mo[a] [2.0]** |
|---|---|---|---|---|---|---|
| | ***Mo3d*** | ***S2p*** | ***Mo3d*** | ***S2p*** | | |
| **as-deposited** | 229.09 | 161.94 | 1.46 | 1.57 | 0.54 | 4.41 |
| **TT380** | 228.78 | 161.63 | 1.06 | 1.08 | 0.63 | 2.31 |

[a] To calculate S/Mo ratio, total amount of different sulfur species has been taken into account

Annealing eliminates almost entirely the elemental sulfur. However, despite the increased annealing temperature from 350 to 380 $^oC$, similar to the previous sample, a small amount of free sulfur still remained as can be seen in the S2p spectra, once more not detectable in the Mo3d-S2s region. The sulfur loss due to annealing has also been evidenced by the S/Mo ratio reduced from 4.41 to 2.31 after 1 h annealing at 380 °C. Interestingly, the value for the as deposited film is higher than in 15kV IJD deposition. Being well known that in case of sublimation from $MoS_2$, preferential emission of sulfur occurs, this is a further proof of what empirically observed during IJD growth, i.e. the deposited energy does not induce only local ablation but also whole target heating leading to sulfur sublimation that increases its concentration in the deposited film.

Another sample has been prepared by 12 kV acceleration voltage. The survey spectra confirmed the presence of molybdenum and sulfur in the thin film (**Figure** 4-6a). Also, since from the previous samples, 350 $^oC$ and 380 $^oC$ annealing temperature for 1 h did not completely removed the free sulfur, the annealing temperature was increased to 400 $^oC$. Mo3d-S2s and S2p core levels are presented in **Figure** 4-6b-c.

In the survey spectra (**Figure** 4-6a), Mo3d and S2p becomes more dominant after annealing, which can be attributed to the elimination of free sulfurs from the film surface, which results in increasing the detectability of the photoemission signals. As given in the analyzed spectra of Mo3d and S2p (**Figure** 4-6b and c), no free sulfur can be detected in the annealed sample, which indicates that the 400 $^oC$ annealing for 1 h is sufficient to completely eliminate the elemental sulfur from the IJD-$MoS_2$ thin film.

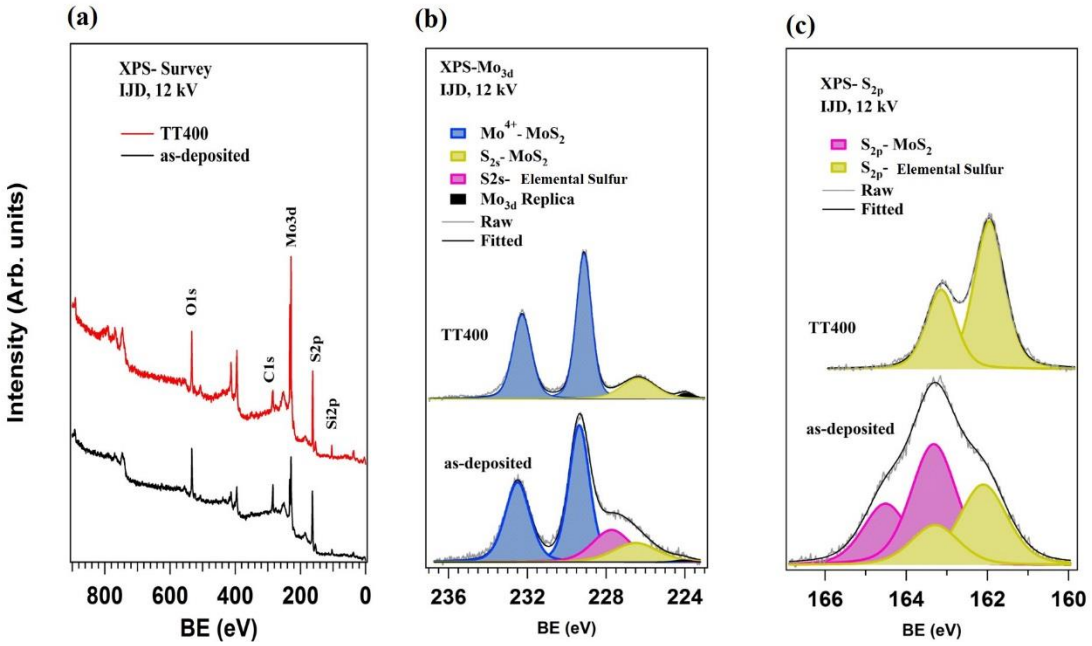


**Figure** 4-6 IJD-$MoS_2$ thin film deposited by 12 kV acceleration voltage, (a) survey spectra, (b) Mo3d-S2s and (c) S2p core levels.

The $Mo3d_{5/2}$ and $S2p_{3/2}$ binding energies of the as-deposited $MoS_2$ found to be 229.34 eV and 162.07 eV, with an energy difference between the two core levels of 67.27 eV, thus larger than the 2H-$MoS_2$ value of 61.19eV and the previously observed ~61.16eV. Moreover, the S/Mo ratio is 4.63, the highest observed in our experiments. After annealing at 400 ºC, both peaks experienced a downward shift. The final peak positions for $Mo3d_{5/2}$ and $S2p_{3/2}$ found to be 229.08 eV and 161.92 eV, respectively, with an energy difference of 67.16 eV, same as for other annealed IJD films and typical of $MoS_2$. The FWHM of $Mo3d_{5/2}$ and $S2p_{3/2}$ in the as-deposited sample found to be 1.35 eV and 1.34 eV, which after thermal treatment decreased to 0.94 and 0.98 eV, respectively.

S/Mo ratio reduced from 4.63 to 2.14, which also confirms the elimination of free sulfur. Interestingly, also in this case the value of the as-deposited film is higher than for 15 kV, suggesting an excess of sulfur whose origin is probably different from the 18 kV case. Although further analysis should be necessary, we can speculate that 12 kV does not enable a complete and efficient ablation process, leading to extraction of a plasma which is richer in the lighter species, i.e. sulfur. This is also in agreement with binding energy difference between $Mo3d_{5/2}$ and $S2p_{3/2}$ core levels, different from typical 2H-$MoS_2$, suggesting an ablation process with reduced efficiency in creating a proper plasma for material synthesis. Anyway, these results clearly identify 15 kV as the acceleration voltage for $MoS_2$ with best performances.

Regarding WF, for as-deposited and annealed counterpart found to be 4.65 eV and 4.79 eV, respectively (**Figure** 4-7b). No significant changes in the VBM value have been found (0.77 eV and 0.82 eV before and after thermal treatment), while shape of typical band of $MoS_2$ arises after annealing (**Figure** 4-7a). The core levels energy positions, WF and VBM of this sample are summarized in **Table** 4-3.

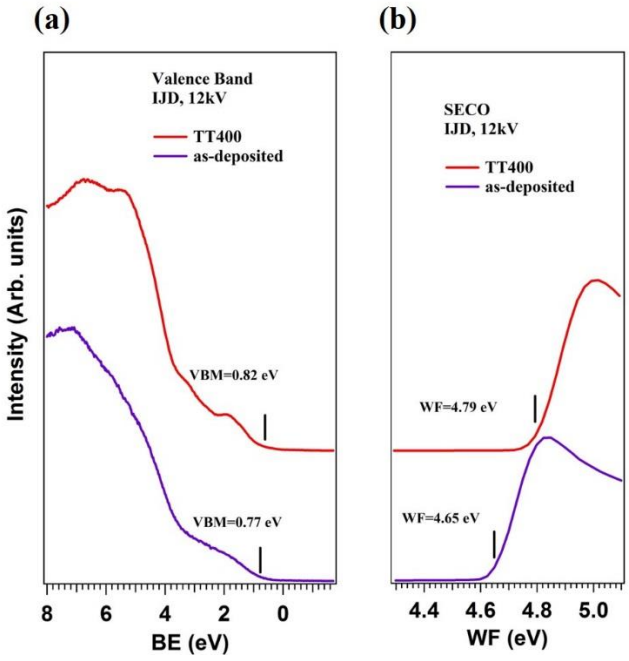


**Figure** 4-7 IJD-$MoS_2$ thin film deposited by 12 kV acceleration voltage. (a) Valence band and (b) SECO spectra.

**Table** 4-3 Binding energy, FWHM, WF and S/Mo ratio of IJD-$MoS_2$ deposited at 12 kV

| | **BE (eV)** | | **FWHM** | | **VBM (eV)** | **WF (eV)** | **S/Mo[a] [2.0]** |
|---|---|---|---|---|---|---|---|
| | ***Mo3d*** | ***S2p*** | ***Mo3d*** | ***S2p*** | | | |
| **as-deposited** | 229.08 | 162.07 | 1.35 | 1.34 | 0.77 | 4.65 | 4.63 |
| **TT400** | 228.34 | 161.92 | 0.94 | 0.98 | 0.82 | 4.79 | 2.14 |

[a] To calculate S/Mo ratio, total amount of different sulfur species has been taken into account

Moreover, comparing the core level position, WF and VBM of the samples deposited at 15 and 12 kV acceleration voltage, it can be inferred that IJD-$MoS_2$ thin film deposited at 15 kV is more n-type than its 12 kV counterpart, as VBM is closer to Fermi level even if WF is higher. Also, core level BEs are higher in the 12 kV IJD film, this suggests a complex scenario concerning the electronic levels and properties of this $MoS_2$ film.

In our experiments we have always found signal from Si substrate, even if the film at a glance was uniform and apparently covering the whole substrate surface. Taking into account an inelastic mean free path of the Si2p photoelectrons around 2 nm, we expected no substrate signal after film growth and, anyway, something related to the $MoS_2/SiO_2/Si$ interface. In order to better investigate this issue, another sample with 12 kV acceleration voltage and only 20 min deposition time (instead of 1 h) has been prepared. As can be seen from **Figure** 4-8a, the amount of molybdenum and sulfur content have been significantly reduced, but on the other hand a more intense signal of silicon was detected.

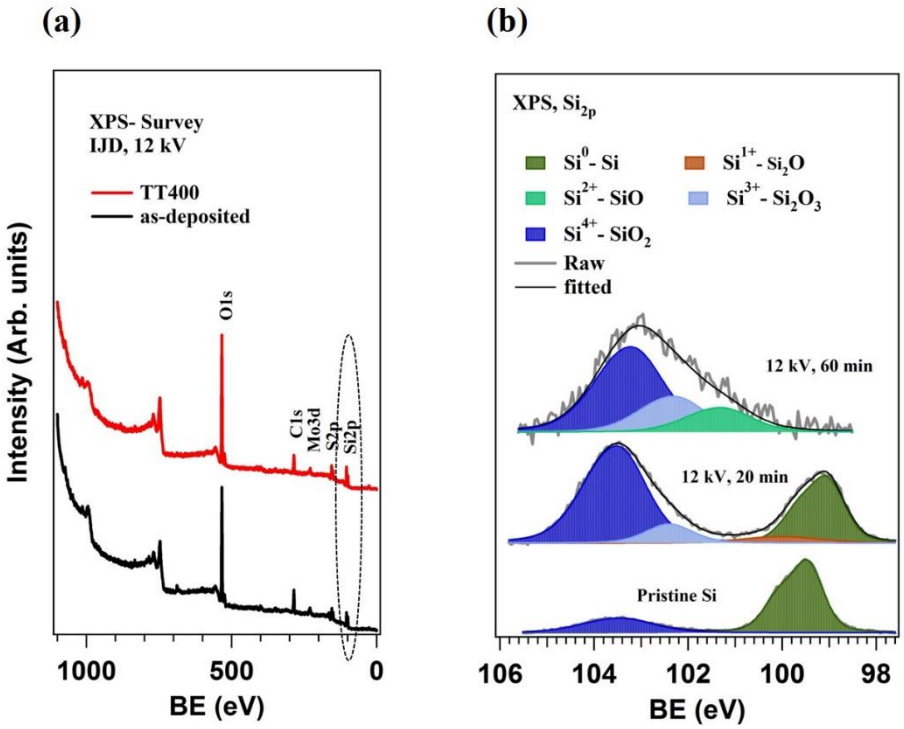


**Figure** 4-8 XPS analysis of silicon species at the interface, (a) wide range from IJD-$MoS_2$ with 20 min deposition, as deposited and after annealing at 400°C; (b) Si2p core level (normalized in intensity) from pristine Si substrate and from $MoS_2$ films (IJD at 12 kV) with 20 and 60 min deposition time.

In **Figure** 4-8b, the spectra of Si2p core level of Silicon with native oxide, along with IJD-$MoS_2$ (IJD at 12 kV) with two different deposition time are shown. Pristine silicon substrate is typically covered with a native oxide film having thickness of about 4-5 Å,[220] with Si2p core level showing two typical peaks with 0 and 4+ oxidation states attributed to Si and $SiO_2$ species and located at 99.45 eV and 103.51 eV. In the IJD-$MoS_2$ film prepared with 20 min deposition, an intense $SiO_2$ peak can be observed at about 103.5 eV. Moreover, two other silicon species, namely $Si_2O$ (BE= 99.96 eV) and $Si_2O_3$ (BE= 102.41 eV) were detected. $Si^0$ peak is still present at 99.15 eV, by increasing the deposition time and hence obtaining a thicker film, the signals attributed to $Si^0$ coming from substrate has completely disappeared.

The three oxide species are detected at 101.31 eV, 102.31 eV and 103.21 eV, which are attributed to SiO, $Si_2O_3$ and $SiO_2$, respectively, in good agreement with the literature.[221,222] The binding energy positions of silicon and silicon oxide species are summarized in **Table** 4-4.

These results suggest the formation of silicon oxides during the $MoS_2$ film growth. The base pressure in deposition chamber is in the $10^{-6}$ mbar range, thus it is reasonable that a partial pressure of water is present. During the IJD deposition, highly reactive oxygen radicals can be formed and transferred to the substrate, leading to formation of new $SiO_x$ species. This means that, during $MoS_2$ growth, a complex oxide interface between silicon substrate and the growing $MoS_2$ film is synthesized, altering the final properties of the TMDC film in a way that is not controllable a priori. The formation of silicon oxide interface has also been reported in $MoS_2$ deposition via other PVD techniques, i.e. magnetron sputtering.[130]

**Table** 4-4 Binding energy position of Silicon and silicon species

| | **BE (eV)** **Si** ($Si^0$) | **BE (eV)** **$Si_2O$** ($Si^{1+}$) | **BE (eV)** **SiO** ($Si^{2+}$) | **BE (eV)** **$Si_2O_3$** ($Si^{3+}$) | **BE (eV)** **$SiO_2$** ($Si^{4+}$) |
|---|---|---|---|---|---|
| **Pristine Silicon** | 99.95 | … | … | … | 104.01 |
| **Ultra-thin film** [a] | 99.65 | 100.46 | … | 102.91 | 104.06 |
| **Thin film** [b] | … | … | 101.81 | 102.81 | 103.71 |

[a] 20 minutes deposition, [b] 60 minutes deposition

Furthermore, a possible interaction of silicon with sulfur cannot be excluded a priori, being the Si2p core level in $SiS_2$ at 103.6 eV. Anyway, such an interface can explain the complex scenario we have found concerning values of core level BEs, WF, VBM at the different IJD acceleration voltages.

In order to obtain more comprehensive knowledge of the structural qualities of the thin film, µ-Raman and XRD analysis have been performed for the films growth at 18 kV, as deposited and annealed at 380°C. XRD spectrum of the annealed sample shows a peak at 14°, corresponding to the (002) direction of 2H-$MoS_2$ lattices (**Figure** 4-9a). However, the FWHM is very large, which indicates a high amount of disorders and defects in the structure. The as deposited film shows no diffraction, suggesting an amorphous character.

The Raman spectra of as-deposited and annealed IJD-$MoS_2$ thin film is given in **Figure** 4-9b. The two main characteristic Raman peaks of $MoS_2$, $E_{2g}{}^1$ and $A_{1g}$ can be observed at 380

$cm^{-1}$ and 405.2 $cm^{-1}$, respectively. Due to annealing, an increase in the relative intensity, as well as a decrease in the FWHM of both peaks can be observed, which is a clear indication of improved order. In the low frequency region, the peak at ~225 $cm^{-1}$ is the most prominent one. This peak is attributed to the defects and disorders in $MoS_2$ crystal structure.[156,223] One must bear in mind that the oxidized Molybdenum, which may form on the surface of the material also induce two vibrations in Raman spectra of $MoS_2$, one at ~820 $cm^{-1}$ and the other close to 226 $cm^{-1}$ which can be mistaken by the defect-induced Raman peak at 225 $cm^{-1}$.[223,224] Since there has not been detected any oxide species of molybdenum in XPS analysis (see **Figure** 4-9a), the Raman peak at ~225 $cm^{-1}$ can undoubtedly be assigned to the defects and disorder.

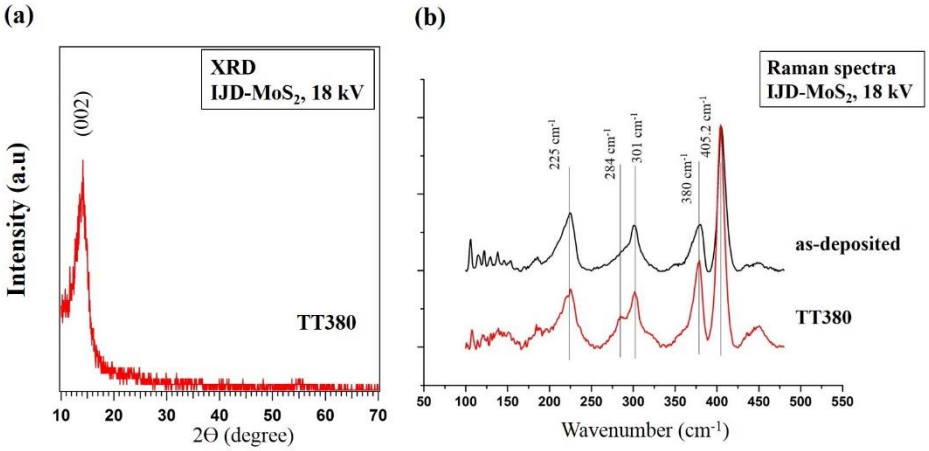


**Figure** 4-9 (a) XRD spectra of IJD-$MoS_2$ deposited at 18 kV and (b) µ-Raman analysis.

Another peak can be observed at around 284 $cm^{-1}$, which is attributed to $E_{1g}$ mode. $E_{1g}$ does not appear in back-scattering measurement set-up.[156,225] This is most likely due to the fact that the basal planes were preferentially situated perpendicular to the laser line irradiation, which prohibits the excitation of such transition. In this work, the Raman measurement was performed in back-scattering mode, means same objective lens was used to collimate and collect the scattered light. The observation of $E_{1g}$ peak, indicates that a considerable amount of $MoS_2$ (cluster of) lattices are misoriented relative to the axis perpendicular to the basal plane.

The two latter peaks are missing in Raman spectra obtained for single crystal $MoS_2$ samples,[226] a clear evidence of the presence of defects and disorders (LA (M) peak at ~225 $cm^{-1}$) as well as misoriented lattices of $MoS_2$ in our IJD film ($E_{1g}$ peak at ~285 $cm^{-1}$).

SEM images from IJD 18 kV as-deposited and thermally treated samples shows a homogenous deposition (**Figure** 4-10a and b). In the annealed sample, 50-100 nm size spots dispersed all over the surface can be see detected. This is attributed to the nature of the IJD techniques and the ablation process, when the highly energetic pulsed-electrons striking the target induces ablation with possible presence of clusters in the range of few nanometer to few micrometer size that can be transferred to the substrate. However, by further tuning the process parameters, this issue can be considerably overcome but is beyond the scope of this study.

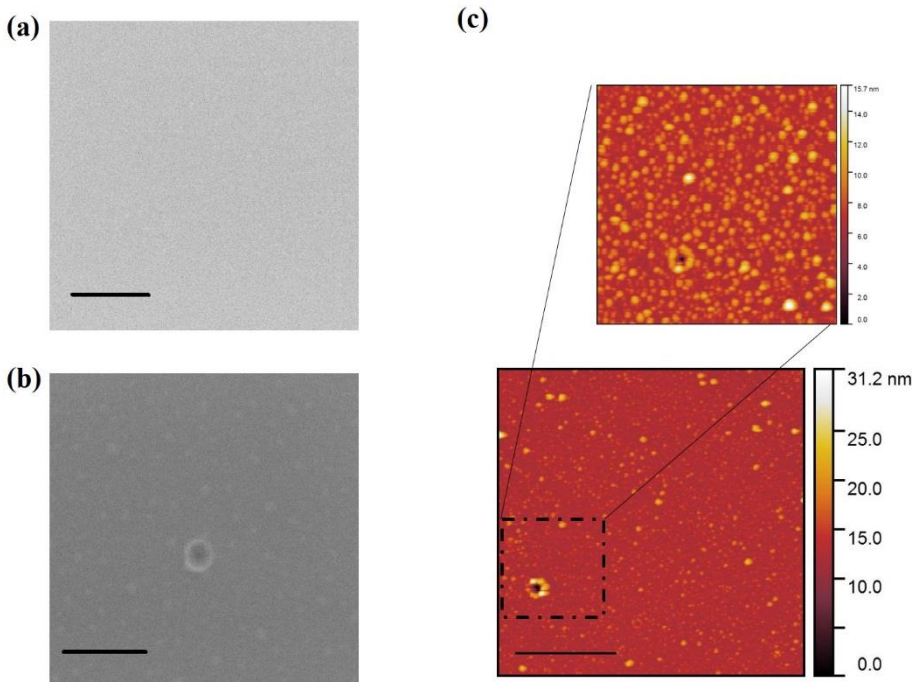


**Figure** 4-10 IJD-$MoS_2$ deposited at 18 kV; SEM image of (a) as-deposited and (b) TT380, and (c) AFM image of TT380. The scale bar size is 500 nm.

The surface morphology of the IJD-$MoS_2$ is presented in the AFM image (**Figure** 4-10c). The spots can more clearly be seen in the AFM image. The surface roughness of the film found to be RMS= 1.28 nm over an area of 5×5 $\mu m^2$.

### 4.5 Conclusions

The room-temperature deposition of $MoS_2$ on silicon substrate by IJD technique has been demonstrated. We found that acceleration voltages lower than 12 kV were not able to induce the ablation process, probably the deposited energy was not enough for $MoS_2$, while values higher than 18 kV led to local explosion of large target pieces rather than a uniform plasma plume, also with strong target overheating. Regarding the deposition frequency, 250 Hz

leads to increased temperature of target material. This can strongly alter the ablation process, also leading to its inhibition and sublimation of the target material, with preferential emission of the lighter species (sulfur in our case). Among the three acceleration voltages tested, 15 kV seems the best compromise in terms of efficient ablation process and absence of target overheating. Deposited films show chemical properties typical of $MoS_2$, with an excess of free, unbounded sulfur and an amorphous matrix, with different type of defects. Sulfur excess can be removed by annealing in the 300-400°C temperature range. Thermal treatment also leads to a certain degree of structural order with misoriented lattices, while electronic properties show an increased WF (sometimes not measurable) and typical p-type semiconducting properties, quite unusual for $MoS_2$ that is n-type. However, the overall scenario is quite difficult to explain, with some films that have shown also undetectable WF values. The origin is probably related to the formation of an interface between $MoS_2$ and silicon substrate, composed of several type of silicon oxides that can significantly change the TMDC film chemical and physical properties. Being probably related to oxidizing processes of water molecules in the vacuum chamber during the growth, such a process cannot be controlled or removed. Thus, a substrate with higher resistance toward oxidation is highly desirable.

### 4.6 IJD deposition of $MoS_2$ on Platinum substrate

Deposition of TMDCs materials on metal substrate has its own advantageous, including but not limited to a reduction in growth temperatures and ease of producing metal-semiconductor contacts without film transfer. (T. Loh, et al., ACS Appl. Mater. Interfaces 2014, 6, 15966-15971). Among available metal substrates (Ag, Al, Cu, Pt), Platinum has been chosen since it has the highest density (21.45 $g/cm^2$), in which, the species present in the IJD plasma, tends to show less solubility into the substate, which can leads to elimination of interface formation.

Room temperature growth of $MoS_2$ thin films on Pt substrate has been performed. The growth template was 50 nm thick platinum deposited on Si by e-beam evaporation (see Ref. [216] for details of growth template preparation). The IJD acceleration voltage was set to be 15 kV. To prevent exertion of excess energy to the target material, the deposition frequency has been set to 150 Hz. All IJD-$MoS_2$ thin films have a thickness of about 200nm. Regarding the annealing temperature, taking into account results achieved for $MoS_2$ growth on silicon, we found that, annealing at 250 $^oC$ (i.e. a temperature also compatible with the majority of

the flexible / polymeric substrate) for 3 hours can induce the desired chemical rearrangement in the as-deposited thin film leading to the desorption of the free sulfur and to a final stoichiometry closed to the nominal one. These values are significantly different from what observed for growth on silicon substrate, in particular same results previously achieved at 350-400°C for 1 h were found at 250°C for 1 h, thus just increasing the annealing time we have been able to completely remove the sulfur excess. This further suggests that the formation of an oxide interface highly affected the film properties for growth on silicon.

### 4.6.1 Chemical analysis

X-ray photoemission spectroscopy (XPS) analysis has been performed to investigate the chemical composition of as-deposited and annealed IJD-$MoS_2$. The survey spectra, Mo3d-S2s and S2p core levels are presented in **Figure** 4-11.

In accordance with the IJD-$MoS_2$ deposited on silicon substrate, the core levels of the as-deposited samples are shifted in binding energy with respect to the typical Mo3d and S2p core level position in $MoS_2$ crystal, and there is presence of unbonded (free) sulfur in the as-deposited film. The BE of $Mo3d_{5/2}$ and $S2p_{3/2}$ peaks in the as-deposited sample were found to be 229.5 eV and 162.3 eV, respectively, which were both shifted to the lower binding energy by annealing the sample. The final binding energy position of the core levels for the annealed $MoS_2$ thin film were found to be 228.9 and 161.8 eV for $Mo3d_{5/2}$ and $S2p_{3/2}$, respectively, which shows a shift of 0.6 eV to lower BE. The energy difference between $Mo3d_{5/2}$ and $S2p_{3/2}$ is always ~67.1 eV, in agreement with 2H-$MoS_2$ expected value and what already observed for IJD growth on silicon. Moreover, the FWHM of the as-deposited sample for $Mo3d_{5/2}$ and $S2p_{3/2,\ MoS2}$ was found to be, 1.4 and 1.3, respectively, which have been reduced by 50% after annealing. The obtained FWHM for annealed sample was found to be 0.9 and 1.0 for $Mo3d_{5/2}$ and $S2p_{3/2}$, respectively. The S/Mo ratio in the as-deposited sample was found to be 2.45, which reduced to 2.11 (i.e. in good agreement with the nominal one) after annealing at 250 $^{o}$C for 3 h.

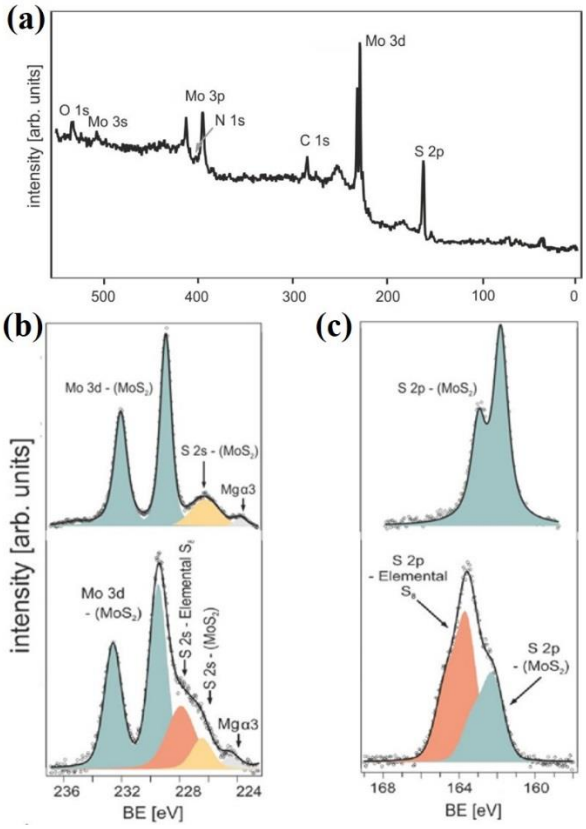


**Figure** 4-11 XPS analysis of IJD-$MoS_2$ on Pt: (a) Survey spectra, (b) Mo3d-S2s and (c) S2p core levels.

### 4.6.2 Structural and morphological characterization

Surface morphology of the as deposited and annealed samples was investigated by SEM and AFM analysis. The low-magnification SEM image of the as-deposited film shows crater-like features. Due to annealing the big features have been disappeared and surface turned out to be more smoothened (**Figure** 4-12c and d). The strain during the thermal treatment probably leads the formation of fractures in the film, as evidenced by the low magnification image for the annealed sample (**Figure** 4-12b).

The AFM image of the annealed sample is also given in **Figure** 4-12e and f. The 20 µm × 20 µm probed area shows a continuous film. However, the crater-like features, pores and protrusions can be detected. To have a closer look to the surface features, the holes and protrusions are shown in the 1 µm × 1 µm probed area **Figure** 4-12e. All the features are in the range of sub-micrometer size.

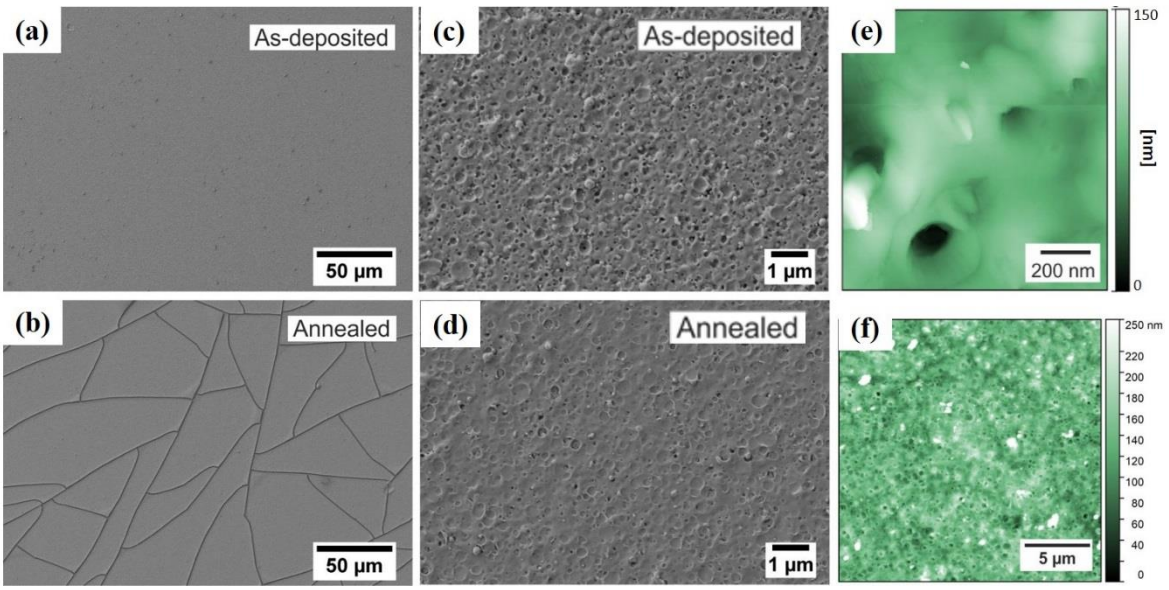


**Figure** 4-12 (a)-(d) SEM images of IJD-$MoS_2$ before and after annealing, (e) and (f) morphology of annealed IJD-$MoS_2$ on Pt obtained by AFM.

The evolution of the crystal structure has been probed by X-ray diffraction. The XRD pattern of the deposited film before and after annealing is presented in **Figure** 4-13a. The as-deposited sample does not show any peak, which indicates that the film is comprised of amorphous structure. However, after annealing distinctive peaks attributed to $MoS_2$ crystal planes appeared. The peak assignment is done accordingly to Ref. [227]. The interlayer distance obtained via the Bragg law is found to be 6.19 Å, which is in good agreement with the standard hexagonal 2H-$MoS_2$ crystal.[228]

To further investigate the arrangements of the $MoS_2$ crystals in the thin film, transmission electron microscopy (TEM) was also employed. To prepare the sample for characterization, the annealed $MoS_2$ thin film was transferred from substrate by gently rubbing on standard carbon-coated copper grids. The bright-filed TEM image of the annealed sample is shown in **Figure** 4-13b. It was found that the film is comprised of crystalline $MoS_2$ nanosheets embedded in an amorphous matrix over entire area. The ring pattern of the corresponding Fast Fourier Transform (FFT) image (inset of the **Figure** 4-13b) indicates that the individual crystalline nanosheets exhibit different orientations. The interplanar distances were found to be 0.62 and 0.27 nm, corresponding to (002) and (004) planes.[229] Moreover, the number of $MoS_2$ layers in an individual nanosheet was found to be in the range 1-4 layer.

To have a deeper insight into the atomic arrangement of the annealed IJD-$MoS_2$, STM measurements has also been performed. The STM image of the crystalline $MoS_2$ nanosheets present in the annealed $MoS_2$ thin film is given in **Figure** 4-1 c-e. The corresponding image

in **Figure** 4-13 d reveals a hexagonal lattice with a periodicity of 0.28 ± 0.06 nm, which is in good agreement to the S-to-S distance between the individual S-Mo-S layers.

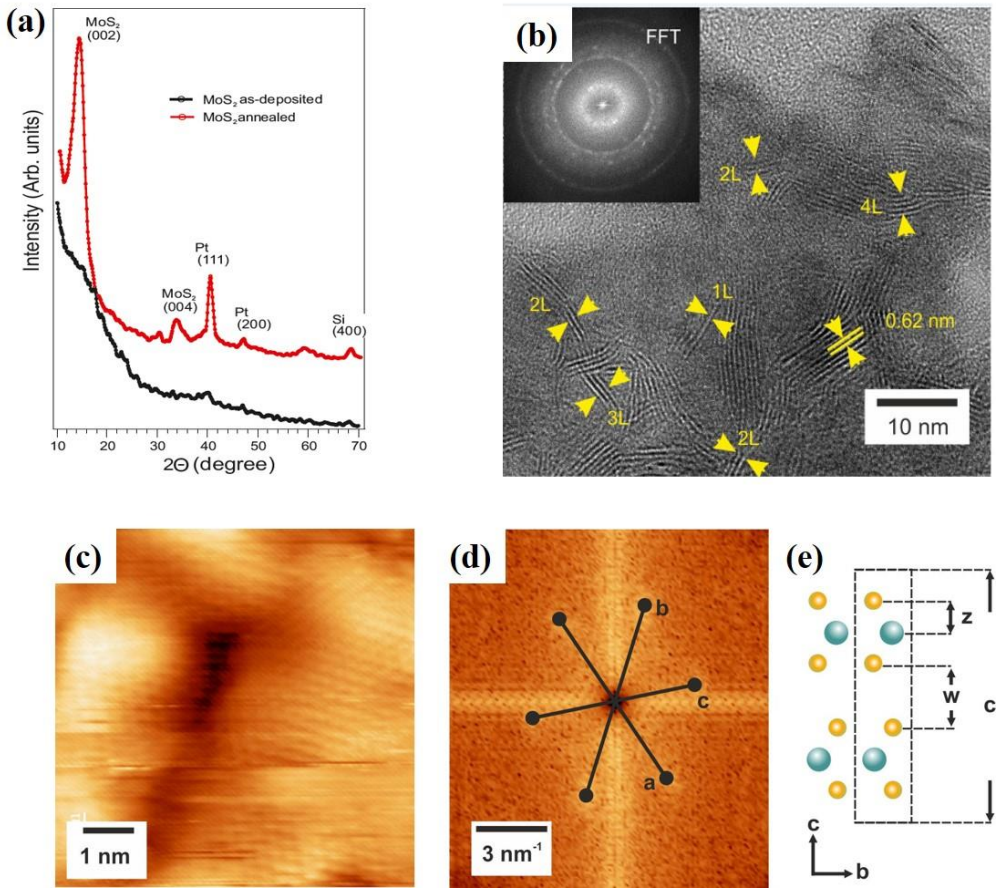


**Figure** 4-13 (a) XRD patterns, (b) High resolution TEM image (FFT image in the inset), (c) Atomic resolution STM image ($V_{bias}$ = -1.1 V, 1.0 nA) and (d) corresponding FFT image of the $MoS_2$ nanosheets; e) top view of the 2H-$MoS_2$ crystal structure showing the Mo-to-S atomic layer distance of z =1.593 Å and the S-to-S distance between the individual S-Mo-S layers of w = 2.959 Å.

### 4.6.3 Optical and vibrational characterization

Non-resonance Raman spectroscopy with excitation wavelength of λ=532 nm has been performed to elucidate the structural properties of the thin film before and after annealing. The $E_{2g}^1$ and $A_{1g}$ peaks were located at 383.0 $cm^{-1}$ and 408.0 $cm^{-1}$ for the as-deposited film and 384.2 $cm^{-1}$ and 403.5 $cm^{-1}$ for annealed film, respectively (**Figure** 4-14b). It can be seen that the distance between two characteristic Raman peaks reduced from 25 $cm^{-1}$ to 19.3$cm^{-1}$ after annealing.

The distance between two characteristic peaks is an indication of the number of layers, which varies from ~19.5 $cm^{-1}$ for monolayer to ~24.5 $cm^{-1}$ for bulk $MoS_2$.[107,156] Accordingly, from the obtained distance of $E_{2g}^1$ and $A_{1g}$ peaks, it can be inferred that the as-deposited IJD-$MoS_2$

shows typical bulk characteristic, which turns into 2D-like after annealing. Although different values have been obtained from the different spots on annealed sample (**Figure** 4-14e), all of them are systematically smaller than 24.5 $cm^{-1}$ with a minimum measured distance of 19.3 $cm^{-1}$. This observation further confirms the formation of mono-to-few layers $MoS_2$ in the annealed IJD-$MoS_2$, which was already evidenced by TEM characterization, with a distribution of flakes with different number of layers in the whole film.

PL measurement with the same excitation wavelength of λ=532 nm has been performed to investigate the optical properties of IJD-$MoS_2$ on Pt. Thanks to the indirect-to-direct band gap transition that occurs when $MoS_2$ confined in mono- and few-layer form, it is possible to distinguish between bulk and 2D-$MoS_2$. The PL spectra acquired from as-deposited and annealed IJD-$MoS_2$ thin film is shown in **Figure** 4-14a. Before annealing no PL signal is detected (black line curve in **Figure** 4-14a), but after annealing the $MoS_2$ remarkably displays a PL signal consisting of a major narrow peak and a minor peak, centered at 1.856 eV and 1.875 eV, which are corresponding to 668 and 661 nm wavelength, respectively.

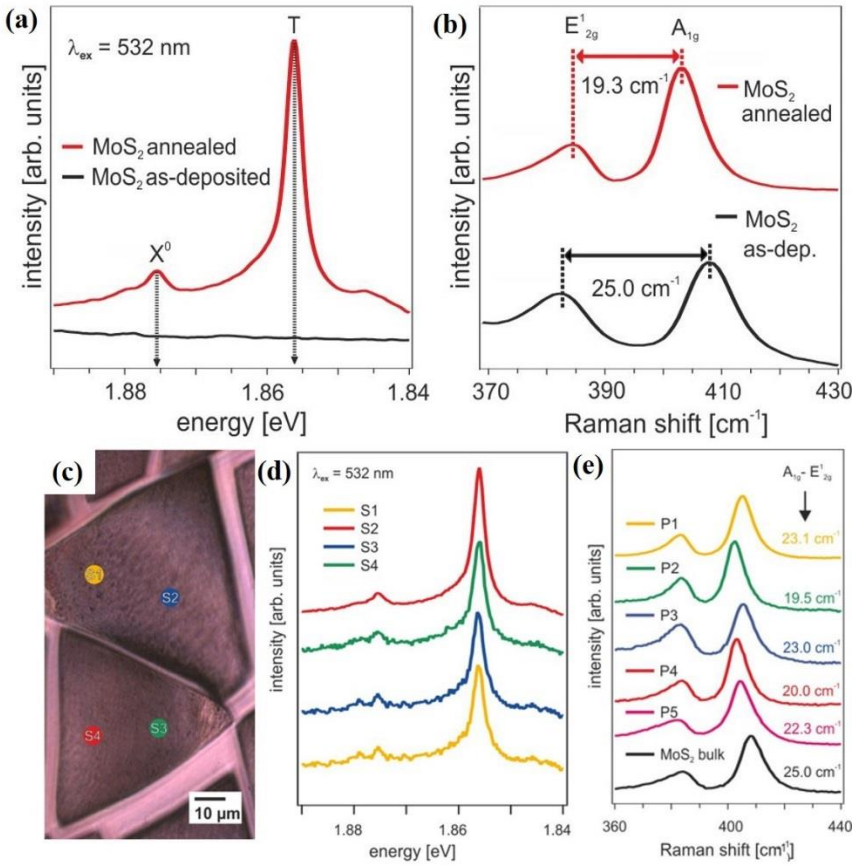


**Figure** 4-14 Vibrational and optical characterization of IJD-$MoS_2$ on Pt: (a) Photoluminescence, (b) non-resonant Raman, (c) optical micrograph showing different sample position for extra PL measurement, (d) corresponding PL spectrum (λ=532 nm), (e) non-Resonant (λ=532 nm) spectra of different sample positions.

It worth to be noted that, the acquired PL emission shows FWHM equal to 4 meV, which is considerably smaller than the previously reported values for room-temperature PL emission of 2D-$MoS_2$ (50- 100 meV).[32,41] Different to the typically observed broad peak centered at ~670 nm, and commonly ascribed to A exciton complexes,[230,231] the two narrow emissions shown by IJD-$MoS_2$ are similar to the low-temperature PL spectra of 2D-$MoS_2$ encapsulated in hexagonal boron nitride,[232,233] and corresponding to neutral excitons, labelled as $X^0$, and lower-energy charged excitons like trions, which are labelled as T (**Figure** 4-14a).More PL spectra obtained from different points on annealed sample with different excitation wavelength (λ=630 nm), confirms that the annealed IJD-$MoS_2$ thin film shows well-resolved PL emission despite the bulk nature of the system (**Figure** 4-14c-d). the observed differences confirm presence of a distribution of flakes in the film with one to few layers, as already observed by TEM and Raman analysis. This introduces further difficulties in properly identifying the mechanism at the origin of the observed PL, and other hypothesis as quantum confinement of these flakes in the amorphous matrix cannot be excluded a priori. Nevertheless, the intensive narrow PL emission indicates the formation of high quality $MoS_2$ thin film and provide strong evidence for being a direct band gap semiconductor material.

### 4.6.4 Surface electronic properties

Valence band and SECO spectra of the IJD-$MoS_2$ before and after annealing have been obtained. It should be noted that the obtained values for the as-deposited sample cannot be considered as a reference, since the film does not display the stoichiometry and crystalline characteristics of $MoS_2$. Similar results have been obtained also for IJD film on silicon substrate, were typical features of $MoS_2$ bands were observed only after annealing. Therefore, we will draw the attention only to the annealed film. However, for the sake of comparison, some measurements have been carried out on a bulk single crystal $MoS_2$. The valence band spectra of the annealed IJD-$MoS_2$ is shown in Figure 4-15c, while its SECO is given in **Figure** 4-15b in comparison with bulk single crystal $MoS_2$. The work function obtained by SECO spectra was found to be 4.95 eV and 4.33 eV for the annealed IJD-$MoS_2$ and bulk single crystal $MoS_2$, respectively. These values suggest more p-type behavior of the IJD deposited $MoS_2$. This has also been further evidenced by valence band maximum (VBM), which found to be 0.6 eV for IJD-$MoS_2$ (**Figure** 4-15c).

The valence band lineshape is also comparable to the one reported for $MoS_2$ single crystal (see **section** 3.4). In the valence band edge, two major components centered at 1.7 eV and 3.5 eV and a minor component centered at 2.6 eV can be seen. This is in accordance with our observation on the annealed single crystal $MoS_2$ (see **Figure** 3-8b).

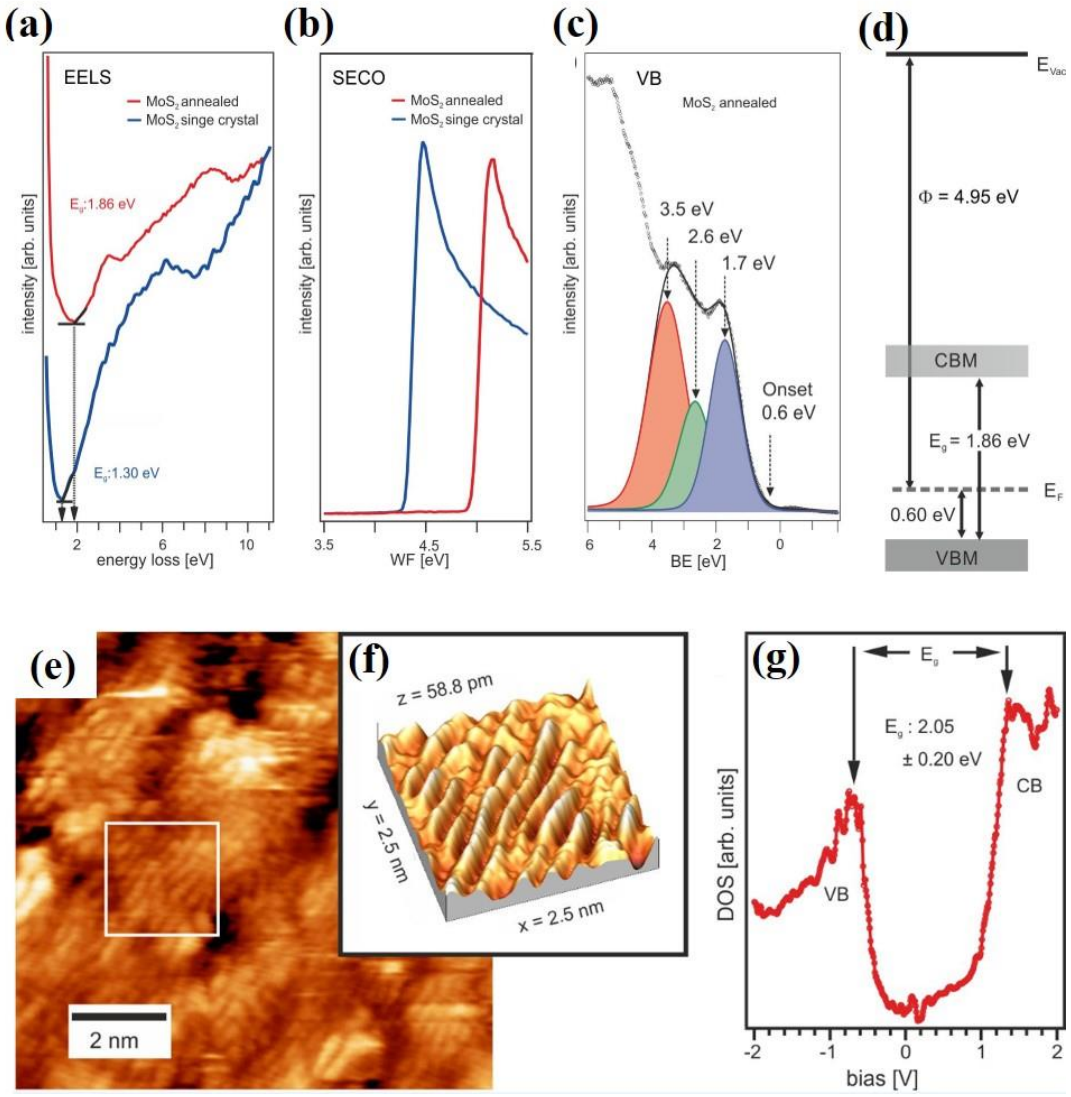


**Figure** 4-15 (a) EELS and (b) SECO spectrum of the IJD-$MoS_2$ vs single crystal $MoS_2$. (c) VB spectra of annealed IJD $MoS_2$. (d) energy level diagram, (e) STM image ($V_{bias}$ = -1.1V, 1.0 nA) of the IJD-$MoS_2$; (f) 3D height profile extracted from the region as marked in panel (e); (g) corresponding STS spectrum.

The optical band gap $E_g$ of the IJD-$MoS_2$ thin film was measured by EELS (**Figure** 4-15a).

For the bulk single crystal $MoS_2$, $E_g$ was found to be 1.30 eV, in good agreement with the previously reported EELS of bulk $MoS_2$,[234] whereas for the annealed IJD-$MoS_2$ thin film, $E_g$ was found to be 1.86 eV. This value is comparable to the one measured for 2D-$MoS_2$, which indicates the direct band gap characteristic of the IJD-$MoS_2$.[235]

To further investigate the 2D electronic characteristic of our thin film, scanning electron spectroscopy (STS) has been used. The local density of states (DOS) taken on the surface is shown in **Figure** 4-15g. The DOS is obtained by averaging over 30 different curves and then according to the procedure described in Ref. [177], the exponential dependence on the tunneling transmission probability of the electrons has been removed. This procedure avoids

the problem of obtaining a wide dynamic range in the tunneling current which in general is a limiting factor in determining band gap on semiconducting surfaces.[177] As a result, the obtained band gap was found to be 2.05 ± 0.20 eV, which lies within the range of previously reported STS band gaps of 2D $MoS_2$.[236,237] The Fermi level position lies in the lower half of the band gap indicating a p-type character, in accordance with the results obtained by UPS analysis.

### 4.6.5 Memristive behavior of IJD-$MoS_2$

Transitional metal dichalcogenides (TMDs) found to be a promising candidate for non-volatile resistive random-access memory, which may also be useful in neuromorphic computing.[238] Recent studies shows the considerable potential of 2D-$MoS_2$ material in memristive devices owing to their excellent resistive switching behavior.[36,239,240]

In order to fabricate an IJD-$MoS_2$ based Resistive Random Access Memory (ReRAM) device, the deposition has also been carried out on pre-patterned Au/$Si_3N_4$ substrate (**Figure** 4-16a), with the Au pads masked during the deposition with polymethyl methacrylate (PMMA), leaving the Au bottom-contacts uncovered for the $MoS_2$ deposition. In the final step (i.e. realization of the top Au contacts), the PMMA was peeled off. More in detail, cylindrical Au metal contacts with 400 µm diameter were deposited on a Si3N4-on-quartz substrate integrating contact lines for external connection to perform the electrical characterization, as displayed in **Figure** 4-16a and b.

The Au bottom contacts on the substrate for subsequent $MoS_2$ thin film and Au top-contact deposition is shown in optical (**Figure** 4-16a) and SEM (**Figure** 4-16b) images, respectively. The device cross sectional view and the obtained I-V characteristics are shown in **Figure** 4-16c and d, respectively.

The use of gold instead of platinum introduce a possible new parameter concerning the role of substrate. However, it can be inferred the equivalent chemical properties of the two metal should not change the MoS2 film final properties. The IJD The IJD deposition parameters were acceleration voltage of 15 kV and pulse frequency of 150 Hz, same as previously used.

Electrical characterization was carried out by contacting the line connected to the bottom electrode and the top electrode with two tungsten tips of a probe station.

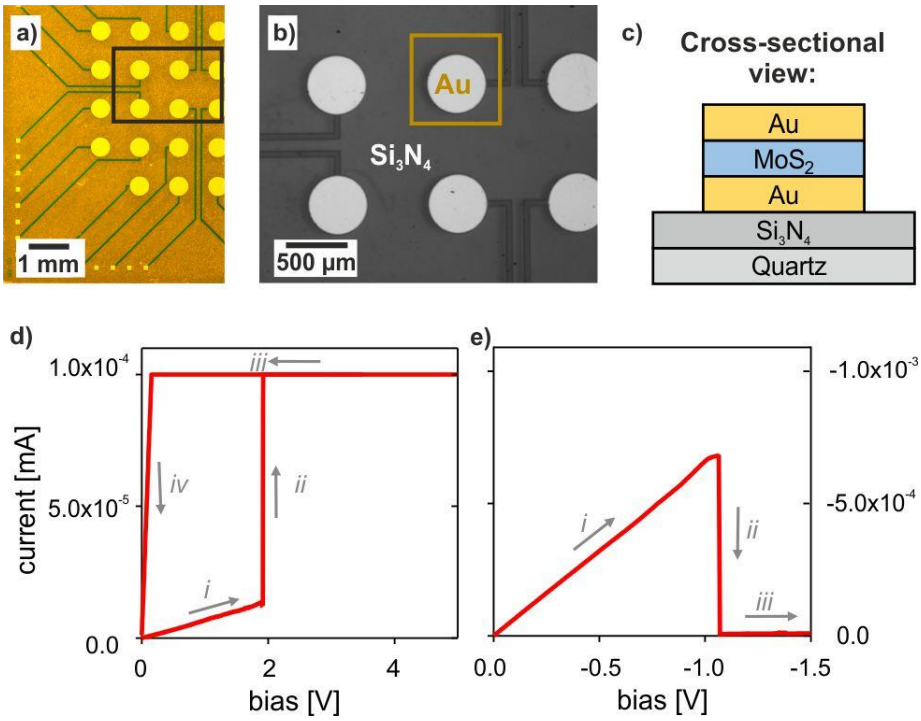


**Figure** 4-16 (a) Optical micrograph of the $Si_3N_4$-on-quartz substrate; (b) SEM image of the region marked in (a); (c) Schematic of the device cross section; I-V curve measurement, (d) forward bias and (e) reverse bias.

Current vs bias (I-V) curves where acquired by voltage sweep (0 V → 5 V → 0 V) while measuring the current through the devices. This leads to abrupt resistivity changes of the $MoS_2$ film, as displayed in **Figure** 4-16d. At the beginning of the sweep (i), linear I-V behavior is observed with constant resistance of $1.66 \times 10^5$ Ω. At a threshold voltage, the current increases abruptly (ii and iii) up to a pre-set compliance level (100 µA). During the back sweep (iii) the current stays at compliance level past the threshold level. A state of low resistivity is reached at $1.55 \times 10^3$ Ω. Reversibility is demonstrated by applying a reverse-biased voltage sweep without current compliance, as displayed in **Figure** 4-16e. An abrupt decrease of current is observed, returning the device to its previous high resistive state. Switching between both resistive states is demonstrated with an ON-OFF ratio of $>10^2$. The observed I-V characteristics are similar to behavior reported for ReRAM based on $MoS_2$ fabricated by other techniques.[188,241] These performances have been tested for several hundreds of cycles, showing good reproducibility and reliability.

The structural and physical properties of the $MoS_2$ film makes difficult the interpretation of the memristive mechanism observed in these devices. This will be further studied in the future, but in this work a clear example of exploitation of IJD $MoS_2$ films was given.

## 4.7 Conclusions

The Ionized Jet Deposition (IJD) technique has been successfully utilized to deposit $MoS_2$ thin film on Si and Pt substrate. The underlying mechanism which leads to ultra-thin $MoS_2$ nanosheets formation is schematically illustrated in **Figure** 4-17. The 1-4 monolayer thick nanosheet are responsible for 2D-like optical and electronic behavior of the annealed IJD-$MoS_2$. As depicted in **Figure** 4-17, molecular-sized species with undefined stoichiometry $Mo_x$-$S_y$ ablate from the $MoS_2$ target and condense on the substrate forming an amorphous film of clusters with nanometric size over entire deposited area. Mo and S atoms, initially form various chemical species, i.e. Mo-S-S-Mo, Mo-Mo-S, Mo-S-S, with a high number of defects, dangling bonds and different chemical environment of Mo atoms, as evidenced by detailed XPS core level analysis of the as-deposited thin film. Impurity atoms such as C, N and O, schematically represented by red atoms in **Figure** 4-17, are present due to the low operating vacuum during IJD deposition, which is around ~$10^{-3}$ mbar. The optimized annealing condition was found to be 250 $^{o}$C for 3 h, through which the rearrangement of $Mo_x$-$S_y$ species into layered crystalline 2D $MoS_2$ nanosheet clusters are enabled.

It was also found that, annealing results in a 0.6 eV downward shift of the core levels to the lower binding energy values relative to the as-deposited counterpart. Such observation can be attributed to the formation of $MoS_2$ 2D-like structure, which was previously found to result in BEs downward shifts with respect to the bulk values.[241] Also, the annealing per se, can lead to a strong change of the electronic properties of the $MoS_2$ thin film, as discussed in **Chapter** 3. The thermal treatment results in a more p-type characteristic of the annealed $MoS_2$ thin film, in agreement with the VBM and WF, which found to be 0.6 eV and 4.95 eV, respectively. Moreover, the observed p-type characteristic could be attributed to the incorporation of C, N and O impurity atoms into substitutional and/or interstitial sites of the $MoS_2$ crystal structure.

However, the most striking feature of the crystalline 2D $MoS_2$ nanosheets is the direct band gap of 1.86 eV, allowing for a strong and well-resolved PL emission. Up to date, such narrow PL emissions were only found in 2D $MoS_2$ encapsulated in h-BN and measured at low temperature.[232,233] In the present study, the well-resolved PL at room temperature might be related to the fact that the 2D $MoS_2$ nanosheets in the IJD-$MoS_2$ thin film are highly crystalline and encapsulated in an amorphous matrix. The encapsulation might effectively suppress inhomogeneous contribution to the exciton linewidth and protect against physisorption and impurities from the environment.[233,242]

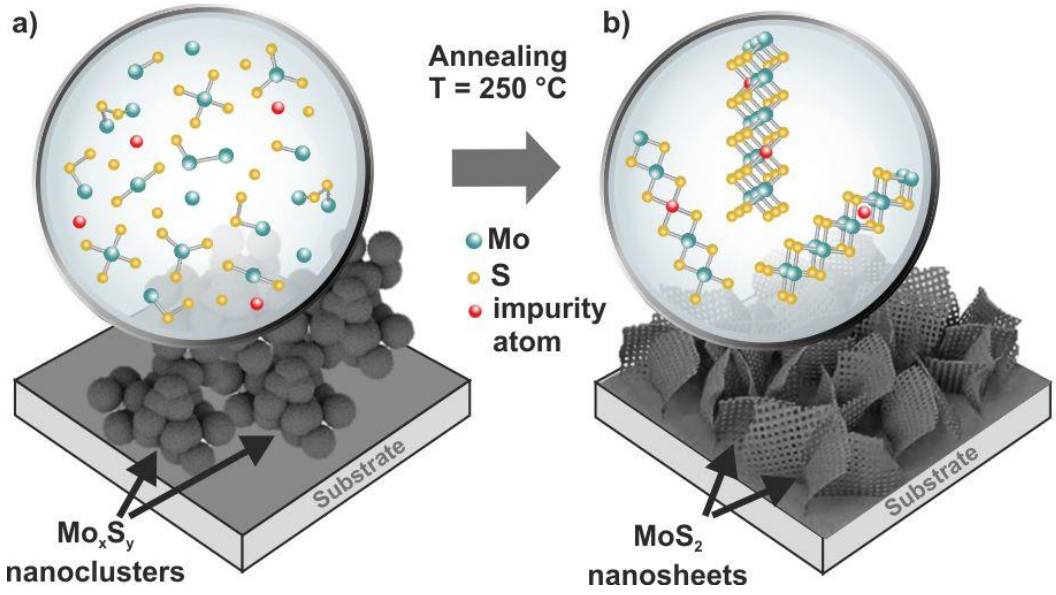


**Figure** 4-17 Schematic illustration of (a) $MoS_2$ nanoclusters in the as-deposited thin film and (b) few-layered $MoS_2$ nanosheets in the annealed thin film (amorphous matrix not shown), and their corresponding atomic arrangement.

In the end, the demonstrated ReRAM device with an abrupt ON/OFF ratio of more than 2 orders of magnitude proves the excellent qualities of the $MoS_2$ nanosheet-containing thin film as a semiconductor material for electronic applications. The device exhibits excellent stability and reproducibility, highlighting the possibility to perform multicycle writing and reset operation.

The results presented here will be object of a scientific paper, now in preparation:

1- **A. Ghiami**, M. V. Nardi, M. Timpel, P. Nozar, A. Chiappini, A. Quaranta, R. Verucchi, "Synthesis of $MoS_2$ Thin Film by Ionized Jet Deposition: Role of Substrate and Working Parameters", in preparation.

2- M. Timpel, G. Ligorio, **A. Ghiami**, L. Gavioli, E. Cavaliere, A. Chiappini, F. Rossi, L. Pasquali, F. Gärisch, E. J. W. List-Kratochvil, P. Nozar, A. Quaranta, R. Verucchi, and M. V. Nardi, "2D-MoS2 goes 3D: Transferring Optical and Electronic Properties of 2D $MoS_2$ to a Mechanically Stable 3D Bulk", in preparation.

# Chapter 5

# Conclusion

Since the discovery of the extraordinary properties of graphene, other two-dimensional nanomaterials, and in particular layered transition metal dichalcogenides (TMDC), have been under intensive investigations. This is due to their exciting physical and chemical properties. TMDCs have been deemed suitable and in some cases a potential breakthrough for several potential applications in a variety of fields such as, electronic, opto-electronic, sensing etc. It is well described in the literature that surface defects are responsible for many undesirable phenomena in electronic and optoelectronic devices based on 2D-TMDCs. Due to that reason, it is crucial to obtain a comprehensive understanding on the role of defects on surface electronic properties and finding ways to further tailor them, which could pave the way toward realization of 2D-TMDCs based electronic devices. Furthermore, despite the many progress has been achieved in wafer-scale synthesis of 2D materials, to reach a reliable and up-scalable synthesis methodology is still highly demanded. Both aforementioned issues were addressed in this thesis.

In the first part, the role of sulfur vacancies on surface electronic properties of $MoS_2$ has been studied. The 2H-$MoS_2$ single crystal with two different defect densities have been obtained by UHV annealing at 300 and 500 $^oC$. It was assumed that, the UHV annealing would yield $MoS_2$ with different amount of sulfur defects. XPS core level analysis confirmed the amount of sulfur vacancies increased about ~30 and ~140% after annealing at 300 and 500 $^oC$, respectively, in comparison to the vacancies natively present on pristine 2H-$MoS_2$. Investigating the core levels obtained by XPS analysis, as well as the valence band and SECO spectra obtained by UPS analysis, a clear correlation between annealing temperature, the relative amount of defects and the consequent WF changes has been reached. It was found that, increasing annealing temperature and introducing more sulfur vacancies, leads to an increase of the work function of ~0.20 and ~0.48 eV on 2H-$MoS_2$ thermally treated at 300 and 500 °C, respectively. At the same time, we observed a rigid shift toward lower binding energies of 0.10 (300°C) and 0.25 (500°C) of core levels, as well as of valence band maximum. The underlying mechanism was attributed to the sulfur loss due to annealing and the consequent appearance of excess negative charge on the Mo centers at the surface, which

leads to the formation of an interface dipole that strongly modifies the electric field at the surface. The observed core level rigid shifts is related to band bending effect, and an additional surface dipole contributes to further increase the work function.

The possibility to fill the vacancies and restore the original electronic structure of the 2H-$MoS_2$ surface was tested by means of molecular functionalization of the thermally treated surface with a thiol molecule containing a phosphonic acid group at one end. The interaction of the thiol molecule and the $MoS_2$ substrate was further assessed by μ-Raman and FT-IR analysis. It was found that, the molecule strongly interacts with the $MoS_2$. It was also shown that, thiol functionalization of thermally treated $MoS_2$ resulted information of a homogeneous and densely packed layer of MUPA (i.e., surface density of ~2.1 mol/$nm^2$) that filled almost completely the sulfur vacancy sites generated by thermal treatment. As a result, the surface band bending was completely recovered, as evidenced by XPS core level analysis of functionalized sample, together with the work function that almost recovers the initial value, with an offset of only 0.08 eV with respect to the pristine surface. This is attributable to a small surface dipole, related to the presence of only a few remaining sulfur vacancy sites.

The study highlights the underlying mechanism through which, the surface treatment of 2H-$MoS_2$ and specifically the generation of sulfur vacancies at the surface can strongly affect the electronic structure of the first interface and, consequently its reactivity. Moreover, via an efficient molecular functionalization, it has been demonstrated how the sulfur vacancies can be filled via a thiol-derived molecule, restoring the initial properties of the 2H-$MoS_2$ surface. The rationalization of the change in the electronic structure of 2H-$MoS_2$ after thermal treatment and molecular functionalization paves the way for a more efficient and effective engineering of both the 2H-$MoS_2$ surface and chemically engineered molecules with specific functionalities that will affect 2H-$MoS_2$ based device performances.

In the second part of the thesis, an up-scalable novel physical vapor deposition (PVD) approach, so called, Ionized Jet Deposition (IJD) has been utilized for the first time to synthesis $MoS_2$ thin film. This technique is based on ablation process of a material induced by a pulsed electron beam at very high power. In this way, thin films of oxides and other materials have been deposited. Initially, the IJD-$MoS_2$ growth has been investigated on Si substrate. The optimum operating conditions were obtained. It was found that 15 kV acceleration voltage and 150 Hz of pulse frequency lead to the best ablation process, as the best compromise in terms of efficient ablation process and absence of target overheating was obtained adopting these working parameters. Deposited film shows chemical properties

typical of $MoS_2$, with an excess of free, unbounded sulfur and an amorphous matrix, with different type of defects. Sulfur excess could be removed by annealing in the 190-400°C temperature range. Thermal treatment also leads to a certain degree of structural order with misoriented lattices as evidenced by XRD. While considering the electronic properties, by post-annealing, there has been occurred an increase in the work function and a more p-type semiconducting property, which is quite unusual for $MoS_2$ that is usually showing n-type character. However, some other unusual electronic properties revealed something uncontrolled was occurring during deposition. Indeed, we had evidence of the formation of an interface between $MoS_2$ and silicon substrate, probably composed of several type of silicon oxides that can significantly change the TMDC film chemical and physical properties. Being probably related to oxidizing processes of water molecules in the vacuum chamber during the growth, such a process cannot be controlled or removed.

Although the results of IJD-$MoS_2$ growth on Si substrate found to be quite promising, in order to avoid the formation of complex interface species, the IJD-$MoS_2$ growth has been optimized and investigated on Pt substrate, which is chemically more stable, un-reactive and resistant than Si in the harsh environment.

Exploiting results achieved for Si substrate, 15 kV acceleration voltage and 150 Hz pulse frequency were used as deposition parameters. Synthesized films (with a thickness of about 200nm) show typical properties of $MoS_2$, with a sulfur excess and amorphous structure. It was found that annealing at 250 $^oC$ for 3 h, makes it possible to completely eliminate the unbonded free sulfur and lead to an ordered 2H-$MoS_2$ nanocrystalline structure. Such a low post-annealing temperature is also compatible with polymeric substrate. TEM analysis of annealed films evidenced the formation of highly crystalline $MoS_2$ nanosheets embedded in amorphous $MoS_2$. The thickness of $MoS_2$ nanosheets was found to be 1-4 monolayer. Interestingly, further investigation on electrical and optical properties carried out by STS, EELS and PL measurements, showed that the IJD-$MoS_2$ thin film, in spite of its bulk nature (thickness of about 200 nm) are characterized by a direct bandgap of about 1.9 eV with strong and well-resolved photoluminescence emission at room-temperature. The observed direct band gap of 1.9 eV is typical for 2D-$MoS_2$ and is thought to be attributed to the fact that the 2D $MoS_2$ nanosheets in the IJD-$MoS_2$ thin film, are highly crystalline and encapsulated in an amorphous matrix. The encapsulation might effectively suppress inhomogeneous contribution to the exciton linewidth and protect against physisorption and impurities from the environment.

In the end, to demonstrate the applicability of the IJD-$MoS_2$ thin films for electronic devices, a resistive random memory (ReRAM) device based on IJD-$MoS_2$ has been realized. The demonstrated ReRAM device showed an abrupt on/off ratio of more than 2 orders of magnitude proves the high qualities of IJD-$MoS_2$ thin film as a semiconductor material for electronic application. The device exhibits excellent stability and reproducibility.

IJD was found to be a promising scalable synthesis approach for TMDCs materials, which can serve excellent electronic and optical properties of 2D-TMDCs in a more stable bulk form. The bulk nature of the IJD films overtake the difficulties in handling of 2D materials. Moreover, the room temperature deposition and a relatively low post-annealing temperature facilities the direct deposition of TMDCs on insulating flexible substrate like Kapton. On the other hand, direct deposition on the pre-patterned wafer can be also possible, which makes IJD a more compatible route with device integration flow in semiconductor device manufacturing industries.

# Chapter 6

# References


1. Novoselov, K. S. *et al.* Electric Field Effect in Atomically Thin Carbon Films Supplementary. *Science (80-. ).* **5**, 1–12 (2004).

2. Soldano, C., Mahmood, A. & Dujardin, E. Production, properties and potential of graphene. *Carbon N. Y.* **48**, 2127–2150 (2010).

3. Pumera, M. Graphene-based nanomaterials for energy storage. *Energy Environ. Sci.* **4**, 668–674 (2011).

4. Yin, Z. *et al.* Graphene-Based materials for solar cell applications. *Adv. Energy Mater.* **4**, 1–19 (2014).

5. Hill, E. W., Vijayaragahvan, A. & Novoselov, K. Graphene sensors. *IEEE Sens. J.* **11**, 3161–3170 (2011).

6. Bhimanapati, G. R. *et al.* Recent Advances in Two-Dimensional Materials beyond Graphene. *ACS Nano* **9**, 11509–11539 (2015).

7. Radisavljevic, B., Radenovic, A., Brivio, J., Giacometti, V. & Kis, A. Single-layer MoS 2 transistors. *Nat. Nanotechnol.* **6**, (2011).

8. Mak, K. F. & Shan, J. Photonics and optoelectronics of 2D semiconductor transition metal dichalcogenides. *Nat. Photonics* **10**, 216–226 (2016).

9. Voiry, D. *et al.* Conducting $MoS_2$ nanosheets as catalysts for hydrogen evolution reaction. *Nano Lett.* **13**, 6222–7 (2013).

10. Li, Y., Xu, C., Hu, P. & Zhen, L. Carrier Control of MoS2 Nanoflakes by Functional Self-Assembled Monolayers. *ACS Nano* **7**, 7795–7804 (2013).

11. Mouri, S., Miyauchi, Y. & Matsuda, K. Tunable photoluminescence of monolayer MoS2 via chemical doping. *Nano Lett.* **13**, 5944–5948 (2013).

12. Kim, J., Yoo, H., Choi, H. O. & Jung, H. Tunable VOCs Sensor by using Thiolated Ligand Conjugation on MoS 2. (2014).

13. Bertolazzi, S., Krasnozhon, D. & Kis, A. Nonvolatile memory cells based on

MoS2/graphene heterostructures. *ACS Nano* **7**, 3246–3252 (2013).

14. Yin, Z. *et al.* Single-layer MoS 2 phototransistors. *ACS Nano* **6**, 74–80 (2012).

15. Wu, W. *et al.* Piezoelectricity of single-atomic-layer MoS2 for energy conversion and piezotronics. *Nature* **514**, 470–474 (2014).

16. Liu, K., Feng, J., Kis, A. & Radenovic, A. Atomically thin molybdenum disulfide nanopores with high sensitivity for dna translocation. *ACS Nano* **8**, 2504–2511 (2014).

17. Groven, B. *et al.* Plasma-Enhanced Atomic Layer Deposition of Two-Dimensional WS2 from WF6, H2 Plasma, and H2S. *Chem. Mater.* **29**, 2927–2938 (2017).

18. Jurca, T. *et al.* Low-Temperature Atomic Layer Deposition of MoS 2 Films. *Angew. Chemie - Int. Ed.* **56**, 4991–4995 (2017).

19. Dumcenco, D. *et al.* Large-area epitaxial monolayer moS<inf>2</inf>. *ACS Nano* **9**, 4611–4620 (2015).

20. Wang, S., Pacios, M., Bhaskaran, H. & Warner, J. H. Substrate control for large area continuous films of monolayer MoS $_2$ by atmospheric pressure chemical vapor deposition. *Nanotechnology* **27**, 085604 (2016).

21. Andrzejewski, D. *et al.* Improved luminescence properties of MoS2 monolayers grown via MOCVD: Role of pre-treatment and growth parameters. *Nanotechnology* **29**, (2018).

22. Kim, T. *et al.* Wafer-scale production of highly uniform two-dimensional MoS2 by metal-organic chemical vapor deposition. *Nanotechnology* **28**, (2017).

23. Serna, M. I. *et al.* Large-Area Deposition of MoS2by Pulsed Laser Deposition with in Situ Thickness Control. *ACS Nano* **10**, 6054–6061 (2016).

24. Ho, Y. *et al.* Post sulfurization effect on the MoS 2 Grown by Pulsed Laser Deposition. **2**, 2–3 (2010).

25. Ho, Y.-T. *et al.* Layered MoS $_2$ grown on *c* -sapphire by pulsed laser deposition. *Phys. status solidi - Rapid Res. Lett.* **9**, 187–191 (2015).

26. Wang, Q. H., Kalantar-Zadeh, K., Kis, A., Coleman, J. N. & Strano, M. S. Electronics and optoelectronics of two-dimensional transition metal dichalcogenides. *Nat.*

*Nanotechnol.* **7**, 699–712 (2012).

27. Zhao, W. & Ding, F. Energetics and kinetics of phase transition between a 2H and a 1T MoS $_2$ monolayer—a theoretical study. *Nanoscale* **9**, 2301–2309 (2017).

28. Li, X. & Zhu, H. Two-dimensional MoS2: Properties, preparation, and applications. *J. Mater.* **1**, 33–44 (2015).

29. Kuc, A., Zibouche, N. & Heine, T. Influence of quantum confinement on the electronic structure of the transition metal sulfide TS2. *Phys. Rev. B - Condens. Matter Mater. Phys.* **83**, 1–4 (2011).

30. Johari, P. & Shenoy, V. B. Tuning the electronic properties of semiconducting transition metal dichalcogenides by applying mechanical strains. *ACS Nano* **6**, 5449–5456 (2012).

31. Yue, Q. *et al.* Mechanical and electronic properties of monolayer MoS 2 under elastic strain. *Phys. Lett. Sect. A Gen. At. Solid State Phys.* **376**, 1166–1170 (2012).

32. Splendiani, A. *et al.* Emerging photoluminescence in monolayer MoS2. *Nano Lett.* **10**, 1271–1275 (2010).

33. Lee, H. S. *et al.* MoS2 Nanosheet Phototransistors with Thickness-Modulated Optical Energy Gap. *Nano Lett.* **12**, 3695–3700 (2012).

34. Fabbri, F. *et al.* Novel near-infrared emission from crystal defects in MoS2 multilayer flakes. *Nat. Commun.* **7**, 13044 (2016).

35. Lei, B. *et al.* Significantly enhanced optoelectronic performance of tungsten diselenide phototransistor via surface functionalization. *Nano Res.* 1–10 (2017) doi:10.1007/s12274-016-1386-1.

36. Wang, W. *et al.* MoS 2 memristor with photoresistive switching. *Sci. Rep.* **6**, 1–10 (2016).

37. Tongay, S. *et al.* Defects activated photoluminescence in two-dimensional semiconductors: interplay between bound, charged, and free excitons. *Sci. Rep.* **3**, 2657 (2013).

38. Carozo, V. *et al.* Optical identification of sulfur vacancies: Bound excitons at the edges of monolayer tungsten disulfide. *Sci. Adv.* **3**, e1602813 (2017).

39. Spataru, C. D., Ismail-Beigi, S., Benedict, L. X. & Louie, S. G. Excitonic Effects and Optical Spectra of Single-Walled Carbon Nanotubes. *Phys. Rev. Lett.* **92**, 1–4 (2004).

40. Singh, N., Jabbour, G. & Schwingenschlögl, U. Optical and photocatalytic properties of two-dimensional MoS2. *Eur. Phys. J. B* **85**, 2–5 (2012).

41. Mak, K. F., Lee, C., Hone, J., Shan, J. & Heinz, T. F. Atomically thin MoS2: A new direct-gap semiconductor. *Phys. Rev. Lett.* **105**, 2–5 (2010).

42. Ataca, C., Topsakal, M., Aktürk, E. & Ciraci, S. A comparative study of lattice dynamics of three- and two-dimensional MoS2. *J. Phys. Chem. C* **115**, 16354–16361 (2011).

43. Antoine, K. Fermi level, work function and vacuum level. *Mater. Horizons* **1**, 96 (2015).

44. Schlesinger, R. *et al.* Controlling the work function of ZnO and the energy-level alignment at the interface to organic semiconductors with a molecular electron acceptor. *Phys. Rev. B - Condens. Matter Mater. Phys.* **87**, 1–5 (2013).

45. Wang, Q. *et al.* Dynamic Photoswitching of Electron Energy Levels at Hybrid ZnO/Organic Photochromic Molecule Junctions. *Adv. Funct. Mater.* **28**, 1–9 (2018).

46. Chhowalla, M. *et al.* The chemistry of two-dimensional layered transition metal dichalcogenide nanosheets. *Nat. Chem.* **5**, 263–275 (2013).

47. Lee, S. Y. *et al.* Chemically Modulated Band Gap in Bilayer Graphene Memory Transistors with High On/Off Ratio. *ACS Nano* **9**, 9034–9042 (2015).

48. Lee, S. Y. *et al.* Large Work Function Modulation of Monolayer MoS2 by Ambient Gases. *ACS Nano* **10**, 6100–6107 (2016).

49. Choi, S., Shaolin, Z. & Yang, W. Layer-number-dependent Work Function of MoS 2 Nanoflakes. *Nat. Commun.* **64**, 1550–1555 (2014).

50. You, A., Be, M. A. Y. & In, I. Work function variation of MoS2 atomic layers grown with chemical vapor deposition : The effects of thickness and the adsorption of water / oxygen molecules. *Appl. Phys. Lett.* **106**, (2015).

51. Leonhardt, A. *et al.* Material-Selective Doping of 2D TMDC through Al xO y Encapsulation. *ACS Appl. Mater. Interfaces* **11**, 42697–42707 (2019).

52. Xu, K., Wang, Y., Zhao, Y. & Chai, Y. Modulation doping of transition metal dichalcogenide/oxide heterostructures. *J. Mater. Chem. C* **5**, 376–381 (2017).

53. English, C. D., Shine, G., Dorgan, V. E., Saraswat, K. C. & Pop, E. Improved contacts to MoS2 transistors by ultra-high vacuum metal deposition. *Nano Lett.* **16**, 3824–3830 (2016).

54. Allain, A., Kang, J., Banerjee, K. & Kis, A. Electrical contacts to two-dimensional semiconductors. *Nat. Mater.* **14**, 1195–1205 (2015).

55. Tao, J., Chai, J. W., Zhang, Z., Pan, J. S. & Wang, S. J. The energy-band alignment at molybdenum disulphide and high- k dielectrics interfaces. *Appl. Phys. Lett.* **104**, (2014).

56. Çakır, D. *et al.* Engineering electronic properties of metal–MoSe $_2$ interfaces using self-assembled monolayers. *J. Mater. Chem. C* **2**, 9842–9849 (2014).

57. Bampoulis, P. *et al.* Defect Dominated Charge Transport and Fermi Level Pinning in MoS2/Metal Contacts. *ACS Appl. Mater. Interfaces* **9**, 19278–19286 (2017).

58. Akaike, K., Koch, N. & Oehzelt, M. Fermi level pinning induced electrostatic fields and band bending at organic heterojunctions. *Appl. Phys. Lett.* **105**, (2014).

59. Kappera, R. *et al.* Phase-engineered low-resistance contacts for ultrathin MoS2 transistors. *Nat. Mater.* **13**, 1–15 (2014).

60. Cho, K. *et al.* Contact-Engineered Electrical Properties of MoS 2 Field-Effect Transistors via Selectively Deposited Thiol-Molecules. *Adv. Mater.* **30**, 1–8 (2018).

61. Kim, C. *et al.* Fermi Level Pinning at Electrical Metal Contacts of Monolayer Molybdenum Dichalcogenides. *ACS Nano* **11**, 1588–1596 (2017).

62. Xu, Y. *et al.* Contacts between Two- and Three-Dimensional Materials: Ohmic, Schottky, and p-n Heterojunctions. *ACS Nano* **10**, 4895–4919 (2016).

63. McDonnell, S., Addou, R., Buie, C., Wallace, R. M. & Hinkle, C. L. Defect-DOMINATED DOPING and CONTACT RESISTANCE in MoS2. *ACS Nano* **8**, 2880–2888 (2014).

64. Liu, Y. *et al.* Approaching the Schottky-Mott limit in Waals metal – semiconductor junctions. *Nature* (2018) doi:10.1038/s41586-018-0129-8.

65. Chee, S. *et al.* Lowering the Schottky Barrier Height by Graphene / Ag Electrodes for High-Mobility MoS 2 Field-Effect Transistors. **1804422**, 1–7 (2019).

66. Kim, G., Kim, S., Park, J., Han, K. H. & Kim, J. Schottky Barrier Height Engineering for. *ACS Nano* **12**, 6292–6300 (2018).

67. Yu, Z. *et al.* Towards intrinsic charge transport in monolayer molybdenum disulfide by defect and interface engineering. *Nat. Commun.* **5**, 5290 (2014).

68. Amani, M. *et al.* Near-unity photoluminescence quantum yield in MoS 2. *Science (80-. ).* **350**, (2015).

69. Najmaei, S. *et al.* Tailoring the Physical Properties of Molybdenum Disul fi de Monolayers by Control of Interfacial Chemistry. *Nano Lett.* **14**, 1354–1361 (2014).

70. Park, J. H. *et al.* Defect passivation of transition metal dichalcogenides via a charge transfer van der Waals interface. *Sci. Adv.* **3**, e1701661 (2017).

71. Bertolazzi, S. *et al.* Engineering Chemically Active Defects in Monolayer MoS $_2$ Transistors via Ion-Beam Irradiation and Their Healing via Vapor Deposition of Alkanethiols. *Adv. Mater.* 1606760 (2017) doi:10.1002/adma.201606760.

72. Bhattacharjee, S., Member, S. & Ganapathi, K. L. Surface State Engineering of Metal / MoS 2 Contacts Using Sulfur Treatment for Reduced Contact Resistance and Variability. *IEEE Trans. Electron Devices* **63**, 2556–2562 (2016).

73. Yu, Z. *et al.* Analyzing the Carrier Mobility in Transition-Metal Dichalcogenide MoS2 Field-Effect Transistors. *Adv. Funct. Mater.* **27**, (2017).

74. Precner, M. *et al.* Evolution of Metastable Defects and Its Effect on the Electronic Properties of MoS 2 Films. *Sci. Rep.* **8**, 1–10 (2018).

75. Siao, M. D., Chang, Z. W., Shih, M. C. & Chiu, Y. P. Two-dimensional electronic transport and surface electron accumulation in MoS2. *Nat. Commun.* **9**, 1–12 (2018).

76. Kim, I. S. *et al.* Influence of stoichiometry on the optical and electrical properties of chemical vapor deposition derived MoS2. *ACS Nano* **8**, 10551–10558 (2014).

77. Baugher, B. W. H., Churchill, H. O. H., Yang, Y. & Jarillo-Herrero, P. Intrinsic electronic transport properties of high-quality monolayer and bilayer MoS2. *Nano Lett.* **13**, 4212–4216 (2013).

78. Wang, H. *et al.* Integrated circuits based on bilayer MoS 2 transistors. *Nano Lett.* **12**, 4674–4680 (2012).

79. Liu, H., Neal, A. T. & Ye, P. D. Channel length scaling of MoS 2 MOSFETs. *ACS Nano* **6**, 8563–8569 (2012).

80. Das, S., Chen, H. Y., Penumatcha, A. V. & Appenzeller, J. High performance multilayer MoS2 transistors with scandium contacts. *Nano Lett.* **13**, 100–105 (2013).

81. Addou, R., Colombo, L. & Wallace, R. M. Surface Defects on Natural MoS2. *ACS Appl. Mater. Interfaces* **7**, 11921–11929 (2015).

82. Ma, Q. *et al.* Controlled argon beam-induced desulfurization of monolayer molybdenum disulfid. *ACS Appl. Mater. Interfaces* **7**, 11921–11929 (2017).

83. Chen, Y. *et al.* Tuning Electronic Structure of Single Layer MoS 2 through Defect and Interface Engineering. *ACS Nano* **12**, 2569–2579 (2018).

84. Choi, B. Y. *et al.* Effects of Electron Beam Irradiation and Thiol Molecule Treatment on the Properties of MoS2 Field Effect Transistors. *J. Korean Phys. Soc.* **72**, 1203–1208 (2018).

85. Nan, H. *et al.* Strong photoluminescence enhancement of MoS2 through defect engineering and oxygen bonding. *ACS Nano* **8**, 5738–5745 (2014).

86. Donarelli, M., Bisti, F., Perrozzi, F. & Ottaviano, L. Tunable sulfur desorption in exfoliated MoSby means of thermal annealing in ultra-high vacuum. *Chem. Phys. Lett.* **588**, 198–202 (2013).

87. Kim, J. *et al.* Direct exfoliation and dispersion of two-dimensional materials in pure water via temperature control. *Nat. Commun.* **6**, 8294 (2015).

88. Chou, S. S. *et al.* Ligand conjugation of chemically exfoliated MoS2. *J. Am. Chem. Soc.* **135**, 4584–4587 (2013).

89. Selhorst, R. C. *et al.* Tetrathiafulvalene-containing polymers for simultaneous non-covalent modification and electronic modulation of MoS2 nanomaterials. *Chem. Sci.* **7**, 4698–4705 (2016).

90. Hofmann, O. T. & Rinke, P. Band Bending Engineering at Organic/Inorganic Interfaces Using Organic Self-Assembled Monolayers. *Adv. Electron. Mater.* **3**,

(2017).

91. Chen, X., Berner, N. C., Backes, C., Duesberg, G. S. & McDonald, A. R. Functionalization of Two-Dimensional MoS2: On the Reaction between MoS2 and Organic Thiols. *Angew. Chemie - Int. Ed.* **55**, 5803–5808 (2016).

92. Du, P. *et al.* A versatile strategy towards non-covalent functionalization of graphene by surface-confined supramolecular self-assembly of janus tectons. *Beilstein J. Nanotechnol.* **6**, 632–639 (2015).

93. Förster, A., Gemming, S. & Seifert, G. Functional thiols as repair and doping agents of defective MoS2 monolayers. *J. Phys. Condens. Matter* **30**, (2018).

94. Ryder, C. R., Wood, J. D., Wells, S. A. & Hersam, M. C. Chemically Tailoring Semiconducting Two-Dimensional Transition Metal Dichalcogenides and Black Phosphorus. *ACS Nano* **10**, 3900–3917 (2016).

95. Canton-Vitoria, R. *et al.* Functionalization of MoS2 with 1,2-dithiolanes: toward donor-acceptor nanohybrids for energy conversion. *npj 2D Mater. Appl.* **1**, 13 (2017).

96. Bertolazzi, S., Gobbi, M., Zhao, Y., Backes, C. & Samorì, P. Molecular chemistry approaches for tuning the properties of two-dimensional transition metal dichalcogenides. *Chem. Soc. Rev.* **47**, 6845–6888 (2018).

97. Voiry, D. *et al.* Covalent functionalization of monolayered transition metal dichalcogenides by phase engineering (SI). *Nat. Chem.* **7**, 45–49 (2014).

98. Nan, H., Zhou, R., Gu, X., Xiao, S. & Ostrikov, K. Recent advances in plasma modification of 2D transition metal dichalcogenides. *Nanoscale* (2019) doi:10.1039/c9nr05522c.

99. Kim, K. H. *et al.* Effect of large work function modulation of MoS2 by controllable chlorine doping using a remote plasma. *J. Mater. Chem. C* **8**, 1846–1851 (2020).

100. Jiang, J. *et al.* A Facile and Effective Method for Patching Sulfur Vacancies of WS2 via Nitrogen Plasma Treatment. *Small* **15**, 1–8 (2019).

101. Cho, K. *et al.* Electrical and Optical Characterization of MoS<inf>2</inf> with Sulfur Vacancy Passivation by Treatment with Alkanethiol Molecules. *ACS Nano* **9**, 8044–8053 (2015).

102. Ding, Q. *et al.* Basal-Plane Ligand Functionalization on Semiconducting 2H-MoS2Monolayers. *ACS Appl. Mater. Interfaces* **9**, 12734–12742 (2017).

103. Zhou, L., He, B., Yang, Y. & He, Y. Facile approach to surface functionalized MoS 2 nanosheets. *RSC Adv.* **4**, 32570 (2014).

104. Sanne, A. *et al.* Radio Frequency Transistors and Circuits Based on CVD MoS2. *Nano Lett.* **15**, 5039–5045 (2015).

105. Makarova, M., Okawa, Y. & Aono, M. Selective adsorption of thiol molecules at sulfur vacancies on MoS 2(0001), followed by vacancy repair via S-C dissociation. *J. Phys. Chem. C* **116**, 22411–22416 (2012).

106. Li, H., Wu, J., Yin, Z. & Zhang, H. Preparation and applications of mechanically exfoliated single-layer and multilayer MoS2and WSe2nanosheets. *Acc. Chem. Res.* **47**, 1067–1075 (2014).

107. Ottaviano, L. & , S Palleschi , F Perrozzi, G D'Olimpio , F Priante , M Donarelli, P Benassi, M Nardone, M Gonchigsuren, M Gombosuren, A Lucia, G. M. and O. A. C. Mechanical exfoliation and layer number identification of MoS 2 revisited Mechanical exfoliation and layer number identification of MoS 2 revisited. *2D Mater.* **4**, (2017).

108. Nicolosi, V., Chhowalla, M., Kanatzidis, M. G., Strano, M. S. & Coleman, J. N. Liquid Exfoliation of Layered Materials. *Science (80-. ).* **340**, 1226419–1226419 (2013).

109. Nguyen, E. P. *et al.* Investigation of two-solvent grinding-assisted liquid phase exfoliation of layered MoS2. *Chem. Mater.* **27**, 53–59 (2015).

110. Backes, C. *et al.* Guidelines for Exfoliation, Characterization and Processing of Layered Materials Produced by Liquid Exfoliation. *Chem. Mater.* acs.chemmater.6b03335 (2016) doi:10.1021/acs.chemmater.6b03335.

111. Jawaid, A. *et al.* Mechanism for Liquid Phase Exfoliation of MoS2. *Chem. Mater.* **28**, 337–348 (2016).

112. Heo, S. N., Ishiguro, Y., Hayakawa, R., Chikyow, T. & Wakayama, Y. Perspective: Highly ordered MoS $_2$ thin films grown by multi-step chemical vapor deposition process. *APL Mater.* **4**, 030901 (2016).

113. Hao, S., Yang, B. & Gao, Y. Orientation-specific transgranular fracture behavior of CVD-grown monolayer MoS2 single crystal. *Appl. Phys. Lett.* **110**, (2017).

114. Eichfeld, S. M. *et al.* Highly scalable, atomically thin WSe2grown via metal-organic chemical vapor deposition. *ACS Nano* **9**, 2080–2087 (2015).

115. Jeong, H. *et al.* Wafer-scale and selective-area growth of high-quality hexagonal boron nitride on Ni(111) by metal-organic chemical vapor deposition. *Sci. Rep.* **9**, 5736 (2019).

116. Delabie, A. *et al.* Low temperature deposition of 2D WS2 layers from WF6 and H2S precursors: impact of reducing agents. *Chem. Commun.* **51**, 15692–15695 (2015).

117. Wirtz, C. *et al.* Atomic layer deposition on 2D transition metal chalcogenides: Layer dependent reactivity and seeding with organic ad-layers. *Chem. Commun.* **51**, 16553–16556 (2015).

118. Lau, C. S. *et al.* Carrier control in 2D transition metal dichalcogenides with Al2O3 dielectric. *Sci. Rep.* **9**, 1–6 (2019).

119. Mattinen, M. *et al.* Atomic Layer Deposition of Emerging 2D Semiconductors, HfS2 and ZrS2, for Optoelectronics. *Chem. Mater.* **31**, 5713–5724 (2019).

120. Mattinen, M. *et al.* Atomic Layer Deposition of Crystalline MoS2 Thin Films: New Molybdenum Precursor for Low-Temperature Film Growth. *Adv. Mater. Interfaces* **4**, 1–11 (2017).

121. Kumar, S. *et al.* High performance UV photodetector based on $MoS_2$ layers grown by pulsed laser deposition technique. *J. Alloys Compd.* **835**, 155222 (2020).

122. Tumino, F., Casari, C. S., Passoni, M., Russo, V. & Li Bassi, A. Pulsed laser deposition of single-layer MoS2 on Au(111): From nanosized crystals to large-area films. *Nanoscale Adv.* **1**, 643–655 (2019).

123. Xie, M. Z. *et al.* Annealing effects on sulfur vacancies and electronic transport of MoS2 films grown by pulsed-laser deposition. *Appl. Phys. Lett.* **115**, (2019).

124. Serna, M. I. *et al.* Growth parameter enhancement for MoS2 thin films synthesized by pulsed laser deposition. *Phys. Status Solidi Curr. Top. Solid State Phys.* **7**, 1–7 (2016).

125. Siegel, G., Venkata Subbaiah, Y. P., Prestgard, M. C. & Tiwari, A. Growth of centimeter-scale atomically thin MoSfilms by pulsed laser deposition. *APL Mater.* **3**, (2015).

126. Fleischauer, D. FUNDAMENTAL ASPECTS OF THE ELECTRONIC STRUCTURE , MATERIALS PROPERTIES AND LUBRICATION PERFORMANCE SPUTTERED MoS , FILMS * An understanding of the fundamental properties of solid lubricants at the atomic level ( e . g . crystallite structure and chemical. *Thin Solid Films* **154**, 309–322 (1987).

127. Tao, J. *et al.* Growth of wafer-scale MoS $_2$ monolayer by magnetron sputtering. *Nanoscale* **7**, 2497–2503 (2015).

128. Samassekou, H. *et al.* Viable route towards large-area 2D MoS2 using magnetron sputtering. *2D Mater.* **4**, (2017).

129. Ling, Z. P. *et al.* Large-scale two-dimensional MoS_2 photodetectors by magnetron sputtering. *Opt. Express* **23**, 13580 (2015).

130. Hussain, S. *et al.* Large-area, continuous and high electrical performances of bilayer to few layers MoS2 fabricated by RF sputtering via post-deposition annealing method. *Sci. Rep.* **6**, 1–13 (2016).

131. Kim, H. S., Kumar, M. D., Kim, J. & Lim, D. Vertical growth of MoS2 layers by sputtering method for efficient photoelectric application. *Sensors Actuators, A Phys.* **269**, 355–362 (2018).

132. Tao, J. *et al.* Growth of wafer-scale MoS2 monolayer by magnetron sputtering. *Nanoscale* **7**, 2497–2503 (2015).

133. Huang, J. H. *et al.* Large-area few-layer MoS2 deposited by sputtering. *Mater. Res. Express* **3**, (2016).

134. Zhong, W. *et al.* Feasible route for a large area few-layer MoS2 with magnetron sputtering. *Nanomaterials* **8**, 1–12 (2018).

135. Kaindl, R. *et al.* Growth, structure and stability of sputter-deposited MoS2 thin films. *Beilstein J. Nanotechnol.* **8**, 1115–1126 (2017).

136. Li, J. & Östling, M. Scalable fabrication of 2D semiconducting crystals for future

electronics. *Electron.* **4**, 1033–1061 (2015).

137. Tao, L. *et al.* Centimeter-Scale CVD Growth of Highly Crystalline Single-Layer MoS2 Film with Spatial Homogeneity and the Visualization of Grain Boundaries. *ACS Appl. Mater. Interfaces* **9**, 12073–12081 (2017).

138. Jung, Y., Ji, E., Capasso, A. & Lee, G. H. Recent progresses in the growth of two-dimensional transition metal dichalcogenides. *J. Korean Ceram. Soc.* **56**, 24–36 (2019).

139. Zhang, J. *et al.* Scalable growth of high-quality polycrystalline MoS2 monolayers on SiO2 with tunable grain sizes. *ACS Nano* **8**, 6024–6030 (2014).

140. Van Der Zande, A. M. *et al.* Grains and grain boundaries in highly crystalline monolayer molybdenum disulphide. *Nat. Mater.* **12**, 554–561 (2013).

141. Lin, Y. C. *et al.* Wafer-scale MoS2 thin layers prepared by MoO3 sulfurization. *Nanoscale* **4**, 6637–6641 (2012).

142. Lee, Y. *et al.* Synthesis of wafer-scale uniform molybdenum disulfide films with control over the layer number using a gas phase sulfur precursor. *Nanoscale* **6**, 2821–2826 (2014).

143. Zhan, Y., Liu, Z., Najmaei, S., Ajayan, P. M. & Lou, J. Large-area vapor-phase growth and characterization of MoS 2 atomic layers on a SiO 2 substrate. *Small* **8**, 966–971 (2012).

144. Najmaei, S. *et al.* Vapour phase growth and grain boundary structure of molybdenum disulphide atomic layers. *Nat. Mater.* **12**, 754–759 (2013).

145. Yu, Y. *et al.* Controlled scalable synthesis of uniform, high-quality monolayer and few-layer MoS2 films. *Sci. Rep.* **3**, 1–6 (2013).

146. Orofeo, C. M., Suzuki, S., Sekine, Y. & Hibino, H. Scalable synthesis of layer-controlled WS2 and MoS2 sheets by sulfurization of thin metal films. *Appl. Phys. Lett.* **105**, (2014).

147. Song, J. G. *et al.* Layer-controlled, wafer-scale, and conformal synthesis of tungsten disulfide nanosheets using atomic layer deposition. *ACS Nano* **7**, 11333–11340 (2013).

148. Zhang, Y. *et al.* Recent Progress in CVD Growth of 2D Transition Metal Dichalcogenides and Related Heterostructures. *Adv. Mater.* **31**, 1–30 (2019).

149. Bosi, M. Growth and synthesis of mono and few-layers transition metal dichalcogenides by vapour techniques: a review. *RSC Adv.* **5**, 75500–75518 (2015).

150. Kim, S. Y., Kwak, J., Ciobanu, C. V. & Kwon, S. Y. Recent Developments in Controlled Vapor-Phase Growth of 2D Group 6 Transition Metal Dichalcogenides. *Adv. Mater.* **31**, 1–39 (2019).

151. Oviroh, P. O., Akbarzadeh, R., Pan, D., Coetzee, R. A. M. & Jen, T. C. New development of atomic layer deposition: processes, methods and applications. *Sci. Technol. Adv. Mater.* **20**, 465–496 (2019).

152. Puurunen, R. L. Surface chemistry of atomic layer deposition: A case study for the trimethylaluminum/water process. *J. Appl. Phys.* **97**, (2005).

153. Leskelä, M. & Ritala, M. Atomic Layer Deposition Chemistry: Recent Developments and Future Challenges. *Angew. Chemie - Int. Ed.* **42**, 5548–5554 (2003).

154. Tan, L. K. *et al.* Atomic layer deposition of a MoS2 film. *Nanoscale* **6**, 10584–10588 (2014).

155. Huang, Y. & Liu, L. Recent progress in atomic layer deposition of molybdenum disulfide: a mini review. *Sci. China Mater.* **62**, 913–924 (2019).

156. Li, H. *et al.* From bulk to monolayer MoS 2: Evolution of Raman scattering. *Adv. Funct. Mater.* **22**, 1385–1390 (2012).

157. Groven, B. *et al.* Two-Dimensional Crystal Grain Size Tuning in WS2 Atomic Layer Deposition: An Insight in the Nucleation Mechanism. *Chem. Mater.* **30**, 7648–7663 (2018).

158. Akimov, I. A., Sirenko, A. A., Clark, A. M., Hao, J. H. & Xi, X. X. Electric-Field-Induced Soft-Mode Hardening in SrTiO3 Films. *Phys. Rev. Lett.* **84**, 4625–4628 (2000).

159. Yang, Z. & Hao, J. Progress in pulsed laser deposited two-dimensional layered materials for device applications. *J. Mater. Chem. C* **4**, 8859–8878 (2016).

160. Abd Elhamid M., Mohamed A. Hafez, Abdelnaser M. Aboulfotouh, and I. M. A.

Study of graphene growth on copper foil by pulsed laser deposition at reduced temperature. *J. Appl. Phys.* **121**, (2017).

161. UMBER KALSOOM, M. SHAHID RAFIQUE, SHAMAILA SHAHZADI, KHIZRA FATIMA, R. S. Bi- tri- and few-layer graphene growth by PLD technique using Ni as catalyst. *Mater. Sci.* **35**, 687–693 (2017).

162. Elhamid, A. M. A., Aboulfotouh, A. M., Hafez, M. A. & Azzouz, I. M. Room temperature graphene growth on complex metal matrix by PLD. *Diam. Relat. Mater.* **80**, 162–167 (2017).

163. Barvat, A. *et al.* Mixed Phase Compositions of MoS 2 Ultra Thin Film Grown by Pulsed Laser Deposition. *Mater. Today Proc.* **5**, 2241–2245 (2018).

164. Loh, T. A. J. & Chua, D. H. C. Growth mechanism of pulsed laser fabricated few-layer MoS2 on metal substrates. *ACS Appl. Mater. Interfaces* **6**, 15966–15971 (2014).

165. McDevitt, N. T., Zabinski, J. S. & Donley, M. S. the Use of Raman-Scattering To Study Disorder in Pulsed-Laser Deposited Mos2 Films. *Thin Solid Films* **240**, 76–81 (1994).

166. Feng, Q. *et al.* Growth of Large-Area 2D MoS 2 ( 1 − x ) Se 2 x Semiconductor Alloys. *Adv. Mater.* **26**, 2648–2653 (2014).

167. Loh, T. A. J. & Chua, D. H. C. Pulsed laser fabricated few-layer MoS2on silver. *Chem. Phys. Lett.* **610**–**611**, 284–287 (2014).

168. Greene, J. E. Review Article: Tracing the recorded history of thin-film sputter deposition: From the 1800s to 2017. *J. Vac. Sci. Technol. A Vacuum, Surfaces, Film.* **35**, 05C204 (2017).

169. Kelly, P. J. & Arnell, R. D. Magnetron sputtering: A review of recent developments and applications. *Vacuum* **56**, 159–172 (2000).

170. Somorjai, G. A. *Introduction to Surface Chemistry and Catalysis*. *a wiley-insterscience publication* vol. 191 (1995).

171. Hufner. *Photoelectron Spectroscopy:Priciples and Applications*. (Springer-Verlag Berlin Heidelberg GmbH, 2003). doi:10.1007/978-3-662-09280-4.

172. Gao, Y. Surface analytical studies of interfaces in organic semiconductor devices.

*Mater. Sci. Eng. R Reports* **68**, 39–87 (2010).

173. Chen, W., Qi, D., Gao, X. & Wee, A. T. S. Surface transfer doping of semiconductors. *Prog. Surf. Sci.* **84**, 279–321 (2009).

174. Chen, W., Qi, D. C., Huang, H., Gao, X. & Wee, A. T. S. Organic-organic heterojunction interfaces: Effect of molecular orientation. *Adv. Funct. Mater.* **21**, 410–424 (2011).

175. Varela, M. *et al.* Materials Characterization in the Aberration-Corrected Scanning Transmission Electron Microscope. *Annu. Rev. Mater. Res.* **35**, 539–569 (2005).

176. Hofer, F., Schmidt, F. P., Grogger, W. & Kothleitner, G. Fundamentals of electron energy-loss spectroscopy. *IOP Conf. Ser. Mater. Sci. Eng.* **109**, (2016).

177. Stroscio, J. A. & Fein, A. P. TUNNELING SPECTROSCOPY OF THE Si(111)2. *Surf. Sci.* **181**, 295–306 (1987).

178. Hong, J. *et al.* Exploring atomic defects in molybdenum disulphide monolayers. *Nat. Commun.* **6**, 1–8 (2015).

179. Wu, Z. & Ni, Z. Spectroscopic investigation of defects in two-dimensional materials. *Nanophotonics* **6**, 1219–1237 (2017).

180. Wang, S., Lee, G. Do, Lee, S., Yoon, E. & Warner, J. H. Detailed Atomic Reconstruction of Extended Line Defects in Monolayer MoS2. *ACS Nano* **10**, 5419–5430 (2016).

181. Kc, S., Longo, R. C., Addou, R., Wallace, R. M. & Cho, K. Impact of intrinsic atomic defects on the electronic structure of MoS 2 monolayers. *Nanotechnology* **25**, (2014).

182. Functionalization, S. *et al.* Communications Towards a Comprehensive Understanding of the Reaction Mechanisms Between Defective MoS 2 and Thiol Molecules. **201706038**, 10501–10505 (2017).

183. Nguyen, E. P. *et al.* Electronic Tuning of 2D MoS2 through Surface Functionalization. *Adv. Mater.* **27**, 6225–6229 (2015).

184. Zhou, W. *et al.* Intrinsic structural defects in monolayer molybdenum disulfide. *Nano Lett.* **13**, 2615–2622 (2013).

185. Backes, C. *et al.* Functionalization of liquid-exfoliated two-dimensional 2H-MoS2.

*Angew. Chemie - Int. Ed.* **54**, 2638–2642 (2015).

186. Tuxen, A. *et al.* Size threshold in the dibenzothiophene adsorption on MoS2 nanoclusters. *ACS Nano* **4**, 4677–4682 (2010).

187. Cho, K. *et al.* Electrical and Optical Characterization of MoS2 with Sulfur Vacancy Passivation by Treatment with Alkanethiol Molecules. *ACS Nano* **9**, 8044–8053 (2015).

188. Nardi, M. V. *et al.* Versatile and Scalable Strategy to Grow Sol-Gel Derived 2H-MoS2 Thin Films with Superior Electronic Properties: A Memristive Case. *ACS Appl. Mater. Interfaces* **10**, 34392–34400 (2018).

189. Song, S. H., Joo, M. K., Neumann, M., Kim, H. & Lee, Y. H. Probing defect dynamics in monolayer MoS2 via noise nanospectroscopy. *Nat. Commun.* **8**, 1–5 (2017).

190. Le, D., Rawal, T. B. & Rahman, T. S. Single-layer MoS2 with sulfur vacancies: Structure and catalytic application. *J. Phys. Chem. C* **118**, 5346–5351 (2014).

191. Kunstmann, J., Wendumu, T. B. & Seifert, G. Localized defect states in MoS 2 monolayers: Electronic and optical properties. *Phys. Status Solidi* **8**, 1–20 (2016).

192. Pandey, M. *et al.* Defect-Tolerant Monolayer Transition Metal Dichalcogenides. *Nano Lett.* **16**, 2234–2239 (2016).

193. Christodoulou, C. *et al.* Tuning the work function of graphene-on-quartz with a high weight molecular acceptor. *J. Phys. Chem. C* **118**, 4784–4790 (2014).

194. Christodoulou, C. *et al.* Tuning the Electronic Structure of Graphene by Molecular Dopants: Impact of the Substrate. *ACS Appl. Mater. Interfaces* **7**, 19134–19144 (2015).

195. Lee, S. Y. *et al.* Large Work Function Modulation of Monolayer MoS 2 by Ambient Gases. 1–8.

196. Li, H., Paramonov, P. & Brédas, J.-L. Theoretical study of the surface modification of indium tin oxide with trifluorophenyl phosphonic acid molecules: impact of coverage density and binding geometry. *J. Mater. Chem.* **20**, 2630–2637 (2010).

197. Leung, C., Kao, L., Su, S., Feng, J. & Chan, T. Relationship between surface dipole, work function and charge transfer: Some exceptions to an established rule. *Phys.*

*Rev. B - Condens. Matter Mater. Phys.* **68**, 1–6 (2003).

198. Van Reenen, S., Kouijzer, S., Janssen, R. A. J., Wienk, M. M. & Kemerink, M. Origin of Work Function Modification by Ionic and Amine-Based Interface Layers. *Adv. Mater. Interfaces* **1**, 1–11 (2014).

199. Sim, D. M. *et al.* Controlled Doping of Vacancy-Containing Few-Layer MoS2 via Highly Stable Thiol-Based Molecular Chemisorption. *ACS Nano* **9**, 12115–12123 (2015).

200. Santoni, A., Rondino, F., Malerba, C., Valentini, M. & Mittiga, A. Electronic structure of Ar+ ion-sputtered thin-film MoS2: A XPS and IPES study. *Appl. Surf. Sci.* **392**, 795–800 (2017).

201. Ponomarev, E. *et al.* Hole Transport in Exfoliated Monolayer MoS2. *ACS Nano* **12**, 2669–2676 (2018).

202. Roy, S. *et al.* Atomic Observation of Filling Vacancies in Monolayer Transition Metal Sulfides by Chemically Sourced Sulfur Atoms. *Nano Lett.* **18**, 4523–4530 (2018).

203. Gunter, P. L. J. & Niemantsverdriet, J. W. Thickness determination of uniform overlayers on rough substrates by angle-dependent XPS. **89**, 69–76 (1995).

204. Willmott, P. R. & Huber, J. R. Pulsed laser vaporization and deposition. *Rev. Mod. Phys.* **72**, 315–328 (2000).

205. Shah, S. I., Jaffari, G. H., Yassitepe, E. & Ali, B. *Evaporation: Processes, Bulk Microstructures, and Mechanical Properties*. *Handbook of Deposition Technologies for Films and Coatings* (Elsevier Ltd., 2010). doi:10.1016/B978-0-8155-2031-3.00004-1.

206. Adachi, H., Hirochi, K., Setsune, K., Kitabatake, M. & Wasa, K. Low-temperature process for the preparation of high Tc superconducting thin films. *Appl. Phys. Lett.* **51**, 2263–2265 (1987).

207. Mazzer, M. *et al.* Progress on low-temperature pulsed electron deposition of CuInGaSe2 solar cells. *Energies* **9**, 1–11 (2016).

208. Nistor, M., Mandache, N. B. & Perrière, J. Pulsed electron beam deposition of oxides thin films. *J. Phys. D. Appl. Phys.* **41**, 165205 (2008).

209. Liguori, A., Gualandi, C., Focarete, M. L., Biscarini, F. & Bianchi, M. The pulsed electron deposition technique for biomedical applications: A review. *Coatings* **10**, 1–19 (2020).

210. Gambardella, A., Berni, M., Russo, A. & Bianchi, M. A comparative study of the growth dynamics of zirconia thin films deposited by ionized jet deposition onto different substrates. *Surf. Coatings Technol.* **337**, 306–312 (2018).

211. Skocdopole, J. *et al.* Preparing of the Chameleon Coating By the Ion Jet Deposition Method. *Acta Polytech. CTU Proc.* **9**, 19 (2017).

212. Menossi, D. *et al.* SnS by Ionized Jet Deposition for photovoltaic applications. *2017 IEEE 44th Photovolt. Spec. Conf. PVSC 2017* **2017-Janua**, 2372–2375 (2017).

213. Skočdopole, J., Kalvoda, L., Nozar, P. & Netopilík, M. Preparation of polymeric coatings by ionized jet deposition method. *Chem. Pap.* **72**, 1735–1739 (2018).

214. Skocdopolova, L. DEVICE FOR GENERATING PLASMA AND DIRECTING AN ELECTRON BEAM TOWARDS A TARGET. WO Patent 2013/186697 (2013).

215. Leathem, S. O., Stoltz, P., Messmer, P., Bruhwiler, D. L. & Cambier, J.-L. Influence of the Injection Speeds on the Discharge Characteristics and Minimization of Delay Time in a Pseudospark Discharge. *Open Plasma Phys. J.* **3**, 20–27 (2010).

216. Prusakova, V. *et al.* Morphologic, structural, and optical characterization of sol-gel derived $TiO_2$ thin films for memristive devices. *Phys. Status Solidi* **12**, 192–196 (2015).

217. Shin, G. H. *et al.* Si-MoS 2 vertical heterojunction for a photodetector with high responsivity and low noise equivalent power. *ACS Appl. Mater. Interfaces* **11**, 7626–7634 (2019).

218. Dhyani, V. & Das, S. High-Speed Scalable Silicon-MoS2 P-N Heterojunction Photodetectors. *Sci. Rep.* **7**, 2–10 (2017).

219. Hao, L. *et al.* Electrical and photovoltaic characteristics of MoS2/Si p-n junctions. *J. Appl. Phys.* **117**, (2015).

220. Morita, M., Ohmi, T., Hasegawa, E., Kawakami, M. & Ohwada, M. Growth of native oxide on a silicon surface. *J. Appl. Phys.* **68**, 1272–1281 (1990).

221. Kim, S. *et al.* Size dependence of Si 2p core-level shift at Si nanocrystal/ Si O2 interfaces. *Appl. Phys. Lett.* **91**, 1–4 (2007).

222. Renault, O. *et al.* Synchrotron radiation x-ray photoelectron spectroscopy of Si nanocrystals grown onto Al2O3Si surfaces. *Appl. Phys. Lett.* **87**, 1–3 (2005).

223. Mignuzzi, S. *et al.* Effect of disorder on Raman scattering of single-layer Mo S2. *Phys. Rev. B - Condens. Matter Mater. Phys.* **91**, 1–7 (2015).

224. Camacho-López, M. A. *et al.* Micro-Raman study of the m-MoO2to α-MoO3transformation induced by cw-laser irradiation. *Opt. Mater. (Amst).* **33**, 480–484 (2011).

225. Windom, B. C., Sawyer, W. G. & Hahn, D. W. A Raman Spectroscopic Study of MoS2 and MoO3: Applications to Tribological Systems. *Tribol. Lett.* **42**, 301–310 (2011).

226. Gołasa, K. *et al.* Resonant Raman scattering in MoS2- From bulk to monolayer. *Solid State Commun.* **197**, 53–56 (2014).

227. Gao, D. *et al.* Ferromagnetism in freestanding MoS 2 nanosheets. *Nanoscale Res. Lett.* **8:129**, 1–8 (2013).

228. Fan, X. *et al.* Fast and E ffi cient Preparation of Exfoliated 2H MoS 2 Nanosheets by Sonication-Assisted Lithium Intercalation and Infrared Laser-Induced 1T to 2H Phase Reversion. *Nano Lett.* **15**, (2015).

229. Deokar, G. *et al.* Toward the use of CVD-grown MoS 2 nanosheets as field-emission source. *Beilstein J. Nanotechnol.* **9**, 1686–1694 (2018).

230. Coehoorn, R. *et al.* Electronic structure of MoSe2, MoS2, and WSe2. I. Band-structure calculations and photoelectron spectroscopy. *Phys. Rev. B* **35**, 6195–6202 (1987).

231. Eda, G. *et al.* Photoluminescence from chemically exfoliated MoS 2. *Nano Lett.* **11**, 5111–5116 (2011).

232. Woo Hyun Chae, Jeffrey D. Cain, Eve D. Hanson, A. A. M. Substrate-induced strain and charge doping in CVD-grown monolayer MoS 2 Substrate-induced strain and charge doping in CVD-grown monolayer MoS 2. *Appl. Phys. Lett.* **111,** 143106

(2017).

233. Wierzbowski, J. *et al.* Direct exciton emission from atomically thin transition metal dichalcogenide heterostructures near the lifetime limit. *Sci. Rep.* 7–12 (2017) doi:10.1038/s41598-017-09739-4.

234. Hong, J. *et al.* Layer-dependent anisotropic electronic structure of freestanding quasi-two-dimensional MoS 2. *Phys. Rev. B* **075440**, 1–11 (2016).

235. Dileep, K., Sahu, R., Sarkar, S., Peter, S. C. & Datta, R. Layer specific optical band gap measurement at nanoscale in MoS 2 and ReS 2 van der Waals compounds by high resolution electron energy loss spectroscopy. *J. Appl. Phys.* **114309**, (2017).

236. Rigosi, A. F., Hill, H. M., Rim, K. T., Flynn, G. W. & Heinz, T. F. Electronic band gaps and exciton binding energies in monolayer Mo x W 1- x S 2 transition metal dichalcogenide alloys probed by scanning tunneling and optical spectroscopy. *Phys. Rev. B* **94**, 1–6 (2016).

237. Liu, X. *et al.* Rotationally Commensurate Growth of MoS 2 on Epitaxial Graphene. *acs na* **10**, 1067–1075 (2016).

238. Sangwan, V. K. *et al.* Multi-terminal memtransistors from polycrystalline monolayer molybdenum disulfide. *Nature* **554**, 500–504 (2018).

239. Ge, R. *et al.* Atomristor: Nonvolatile Resistance Switching in Atomic Sheets of Transition Metal Dichalcogenides. *Nano Lett.* **18**, 434–441 (2018).

240. Wang, M. *et al.* Robust memristors based on layered two-dimensional materials. *Nat. Electron.* **1**, 130–136 (2018).

241. Yin, Z. *et al.* Memory Devices Using a Mixture of MoS 2 and Graphene Oxide as the Active Layer. *Small* **9**, 727–731 (2013).

242. Cadiz, F. *et al.* Excitonic Linewidth Approaching the Homogeneous Limit in MoS 2 -Based van der Waals Heterostructures. *Phys. Rev. X* **7**, 1–12 (2017).